# MEASUREMENT OF NEUTRON RADIATIVE CAPTURE CROSS SECTIONS FOR $^{70}Zn(n, \gamma)^{71}Zn^{m}$ REACTION USING ISOTOPICALLY ENRICHED $^{70}Zn$ ISOTOPE IN THE FEW MeV INCIDENT NEUTRON ENERGY REGION

A

**Thesis submitted in fulfillment of the**

**requirement for the degree of**

**Doctor of Philosophy**

**in Physics**


**By**

**LALRINMAWIA PUNTE**


**To**



**SCHOOL OF PHYSICAL SCIENCES**

**DEPARTMENT OF PHYSICS**

**MIZORAM UNIVERSITY**

**TANHRIL-796004**


**July, 2018**

# MEASUREMENT OF NEUTRON RADIATIVE CAPTURE CROSS SECTIONS FOR $^{70}Zn(n, \gamma)^{71}Zn^{m}$ REACTION USING ISOTOPICALLY ENRICHED $^{70}Zn$ ISOTOPE IN THE FEW MeV INCIDENT NEUTRON ENERGY REGION

A

**Thesis submitted in fulfillment of the**

**requirement for the degree of**

**Doctor of Philosophy**

**in Physics**


**By**

**LALRINMAWIA PUNTE**

**(Reg. No.: MZU/Ph.D./692 of 20.10.2014)**


**To**



**SCHOOL OF PHYSICAL SCIENCES**

**DEPARTMENT OF PHYSICS**

**MIZORAM UNIVERSITY**

**TANHRIL-796004**


**July, 2018**

Dr. B. Lalremruata
Assistant Professor
Department of Physics
Mizoram University
Tanhril-796004
Aizawl, Mizoram


**MIZORAM UNIVERSITY**
**DEPARTMENT OF PHYSICS**
**AIZAWL 796 004 MIZORAM**
Phones: 0389 - 2330435, - 2330522
FAX : 0389 - 2330522
Mobile : +919436779952
E-mail : marema08@gmail.com

(A Central University Established by an Act of Parliament)

Date: 20th July, 2018

# Certificate

This is to certify that the thesis entitled *"**Measurement of neutron radiative capture cross sections for $^{70}Zn(n, \gamma)^{71}Zn^{m}$ reaction using isotopically enriched $^{70}Zn$ isotope in the few MeV incident neutron energy region**"* submitted by Mr. Lalrinmawia Punte, for the degree of Doctor of Philosophy in Physics, of the Mizoram University: Aizawl, India, embodies the record of original investigations carried out by him under our supervision. He has been duly registered and the thesis presented is worthy of being considered for the award of Ph.D. degree. This research work has not been submitted for any degree of any other university.

**(Dr. HRANGHMINGTHANGA)**
**Joint-Supervisor**

**(Dr. B. LALREMRUATA)**
**Supervisor**

# Declaration of the Candidate

**Mizoram University**
**July, 2018**

I Lalrinmawia Punte, hereby declare that the subject matter of this thesis is the record of work done by me, that the contents of this thesis did not form bias of the award of any previous degree to me or to do the best of my knowledge to anybody else, and that the thesis has not been submitted by me for any research degree in any other University/Institute.

This is being submitted to the Mizoram University for the degree of Doctor of Philosophy in Physics.

**(LALRINMAWIA PUNTE)**
**Candidate**

**(Prof. SUMAN RAI)**
**Head**
**Department of Physics**
**Mizoram University**

**(Dr. B. LALREMRUATA)**
**Supervisor**

# Acknowledgment

First and foremost, I would like to thank God Almighty for giving me the strength, knowledge, ability and opportunity to undertake this research study and to persevere and complete it satisfactorily. Without his blessings, this achievement would not have been possible.

I would like to thank several people who, in different ways, contributed directly and indirectly to my Ph.D. work and this thesis is incomplete without acknowledging them.

After thanking Almighty God, the first person I wish to convey my sincerest thanks, is my Honourable Supervisor Dr. B. Lalremruata, Department of Physics, Mizoram University, for all the guidance and for being always there when necessary not only as a teacher but also as a researcher and his endless encouragement. With his endless energy, expertise, and patience, he contributed to every aspect of this thesis, even in very complicated moments of his life. The co-operation extended by him towards me during all phases of my research work as well as personal life is gratefully acknowledged. Without him, it would not have been possible to complete this Ph.D. work.

I would like to express my deep sense of gratitude to my Joint-Supervisor Dr. Hranghmingthanga, Department of Physics, Mizoram University for his able guidance and incessant encouragement.

I am deeply thankful to Dr. N. Otsuka for many fruitful discussions and advice during our daily collaboration. I am very fortunate and proud to have worked under his guidance.

I am also thankful to Dr. S.V. Suryanarayana, Dr. B. K. Nayak, L. S. Danu, V.V. Desai, S. Kailas, S. Ganesan, A. Saxena, for their help and advice in setting up

the data acquisition system.

I have a great pleasure in extending my sincere thanks to all the members of the NHERG group (my lab-mates and friends), Dr. Satheesh, H. Lalremruata, Rebecca Lalnuntluangi and J. Lalnunthari for their help and kind cooperation during all these years.

I am also thankful to our former head of the Department and present Head, Prof. Suman Rai, and all of our teaching staffs for their guidance and support during my Ph.D. work.

I would like to express gratitude towards all the non-teaching staff of the Department of Physics, Mizoram University, Aizawl, and staff of University workshop.

I am thankful to a joint collaborative research project between the Department of Physics, Mizoram University, and BARC, Mumbai under the financial support provided by the B.R.N.S., DAE, Mumbai, for providing research Fellowship during the research work, and also thanks to IAEA Nuclear Data Section for supporting this work.

I also wish to express my deep sense of gratitude towards my father, my brothers and sister, In-laws, my wife Tetei and son Hlutea for their moral support, understanding and constant encouragement at all stages, during the research work.

**Dated : Aizawl**
**The 20th July, 2018**

**(LALRINMAWIA PUNTE)**
**Department of Physics**
**Mizoram University**
**Aizawl, Mizoram**

# Contents

## List of Figures

**List of Tables**

| | | |
|---|---|---|
| 22 | The $^{70}Zn(n, \gamma)^{71}Zn^{g+m}$ capture cross sections derived from the experimental $^{70}Zn(n, \gamma)^{71}Zn^{m}$ cross sections $<\sigma_{Zn}^{g+m}>_{present}$. The ratio of the evaluated cross sections folded by the ($p$ ,$n_0$) neutron flux energy spectra for TENDL-2015 $<\sigma_{Zn}^{g+m}>_{TENDL}$, JENDL-4.0 $<\sigma_{Zn}^{g+m}>_{JENDL}$, TALYS-1.6 with generalized superfluid level density model $<\sigma_{Zn}^{g+m}>_{TALYS}$ to the present cross sections are also given. | 93 |

*Dedication*

*To my parents, wife, son, brothers*

*and sisters*

# CHAPTER 1

# INTRODUCTION

# 1. INTRODUCTION

## 1.1. Motivation

The neutron capture cross sections of zinc isotopes are important for nuclear astrophysics. In the solar system, about half of the nuclei beyond iron are produced by the slow neutron capture process (*s*-process), the other half by the rapid neutron capture process (*r*-process), and a marginal contribution is provided by the so-called *p*-process (Burbidge *et al*. 1957). Most of the *s* elements between iron and strontium ($60 \lesssim A \lesssim 90$) are generated at about 90 keV in massive stars with mass $M > 8M_{\odot}$ ($M_{\odot}$ stands for the mass of the sun) during stellar He Core burning, and later during C Shell burning via activation of the neutron source reaction $^{22}Ne(\alpha,n)^{25}Mg$ (where $^{22}Ne$ is being produced from double $\alpha$ capture on $^{14}N$ left behind from the CNO cycle), forming the weak *s* component (Käppeler F. *et al*. 1989; Beer *et al*. 1992; Lederer *et al*. 2013; Reifarth *et al*. 2012). In shell C-burning, due to higher MACS uncertainties at higher temperatures, the *s*-process nucleosynthesis is more uncertain than in the He core (Pignatari *et al*., 2010). For $A \gtrsim 90$, the *s* elements are produced at about 5 to 25 keV in low mass asymptotic giant branch (AGB) stars with mass $1.3M_{\odot} \lesssim M \lesssim 8M_{\odot}$ forming the main *s* component (e.g., Arlandini *et al*., 1999) which is responsible for the mass region from Y to Bi (Reifarth, 2012). Finally, about 50% of the solar $^{208}Pb$ is provided by AGB stars at low metallicity, forming the strong *s* component (Gallino *et al*., 1998). After the formation of a degenerate carbon-oxygen core, the alternating hydrogen shell burning and helium shell burning characterize the AGB stars. During the AGB evolution phase, the *s* process is mainly activated in the radiative $^{13}C$-pocket by the $^{13}C(\alpha, n)^{16}O$ reaction where the $^{13}C$ is being produced via $^{12}C(p, \gamma)^{13}N(\beta^{+})^{13}C$. After a thermal pulse (TP), the shell H burning is not effective and in the He inter-shell

region, the H-rich material from the envelope is mixed down by the Third Dredge Up (TDU). The $^{70}$Zn(*n, γ*) reaction is the strongest local sensitivities in the $^{13}$C-pocket as well as TP for $^{70}$Zn isotope (Koloczek *et al*., 2016). Taking from spectroscopic observation evidences and from Galacticals chemical evolution calculations, Travaglio *et al.* (2004) showed that the weak *s* component and the main *s* component do not fully reproduce the *s* abundances between strontium and barium, proposing the existence of a new unknown component called lighter element primary process (LEPP). There is still under debate about the nature of such a component, and different scenarios have been proposed as an astrophysical site of the LEPP (Pignatari *et al*., 2010).

The s-process path in the region around zinc starting from $^{64}$Zn is completely bypassing the r-only nucleus $^{70}$Zn which is produced when the $^{69}$Zn branching is open during the initial high neutron-density phase and during the final neutron burst (Reifarth *et al.* 2012; Pignatari *et al.*, 2010 ). The branch bypassing occurs at $^{69}$Zn, since the *β*-half-lives of ground and isomeric states are too short (1h and 14 h). Therefore, $^{69}$Zn will always undergo a *β*-decay before capturing a neutron and hence, $^{70}$Zn is bypassed during the weak s-process (Reifarth *et al.*, 2012) between iron and arsenic. The s-process starting from $^{70}$Zn has a contribution for the formation of $^{71}$Ga *via* $^{71}$Zn and hence, $^{70}$Zn(*n*, *γ*) reaction has linked the s-process path through $^{71}$Ga. The **Figure 1** shows how the $^{70}$Zn has linked the s-process path between iron and arsenic. The branching at $^{69}$Zn is indicated by the increase of the overabundance of $^{70}$Zn and the decrease of the abundance ratio of the Germanium isotopes $^{70}$Ge/$^{72}$Ge. Notice that $^{70}$Zn was destroyed during core He burning, but produced by shell C burning. This overabundance of $^{70}$Zn can be used as indicator of the strength of the nuclear reaction flow through the branchings along the s-process path, especially at $^{69}$Zn (The *et al*., 2007). The cross sections in the energy region relevant to the *s*-process have not been

known accurately. In order to improve the situation, Reifarth *et al.*, (2012) performed an experiment to study the Maxwellian averaged cross sections (MACS) of $^{64}$Zn, $^{68}$Zn and $^{70}$Zn neutron captures at kT = 25 keV, which concludes that the $^{70}$Zn neutron capture MACS is about half of the values recommended by Bao *et al.* (2000) though it does not have a strong impact on s-process scenario.

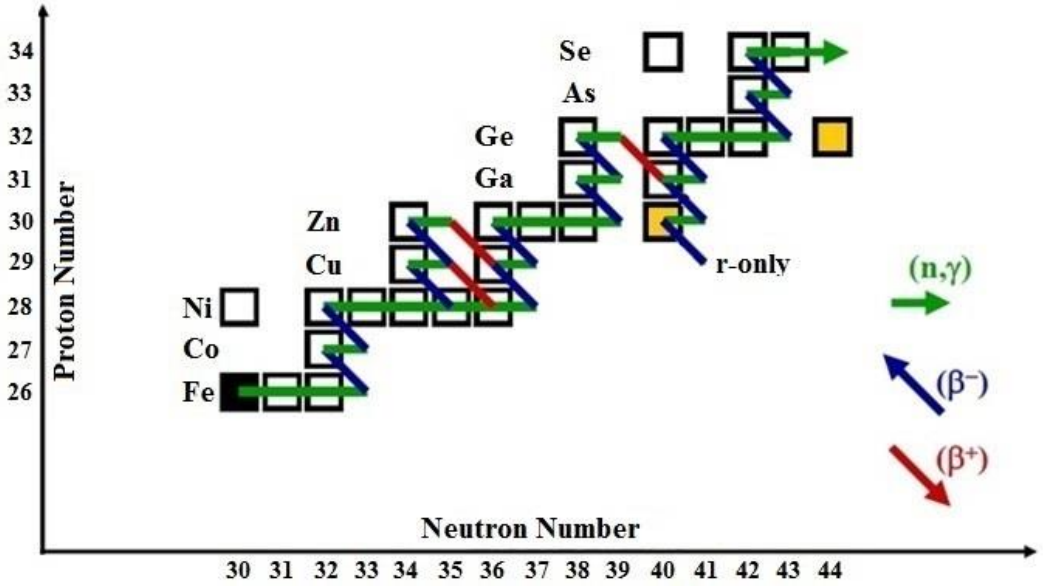


**Figure 1:** Neutron-induced: s-process.

It is also important for nuclear reactor application. The radiative capture cross section of $^{70}$Zn is a candidate of Reactor Dosimetry (Trkov *et al*., 2013). Reactor Dosimetry (RD) is an element of Nuclear Safety Culture. It is applied for determination of neutron field parameters and the neutron flux responses in different regions of the reactor system plays an important role in determining of consecutive effects from the irradiation. That is, for determination of radiation exposure on reactor system elements such as Reactor Pressure Vessel (RPV), internals, shielding; dose determination for material damage study; determination of radiation field parameters for conditioning of irradiation. Therefore, the Reactor Dosimetry is a field that embraces measurements and assessment of the exposure of reactor materials and reactor experiments (Ilieva, 2011). It is also a candidate of dosimetry reactions to study deviation of the epithermal

reactor neutron spectrum from 1/E distribution because there is no $^{70}$Zn+n resolved resonance below 10 keV (Trkov, 2015). The importance of deviation from 1/E distribution is particularly in determining the neutron leakage and absorption in the slowing down energy region.

Except for the thermal neutron energy, the above mentioned kT~25 keV spectrum averaged cross section is the unique experimental $^{70}$Zn neutron capture cross section available in the EXFOR library (Otuka *et al*., 2014), while comparison of evaluated cross sections in the basic evaluated nuclear data libraries TENDL-2015 (Koning *et al.*, 2015), JENDL-4.0 (Shibata *et al.*, 2011 ; Iwamoto *et al.*, 2007) and EAF-2010 (Sublet *et al.*, 2010) shows large discrepancies between the upper boundary of the resolved resonance region and 10 MeV as shown in **Figure 2** and there is no experimental results from upper boundary of the resolved resonance region. So, it is not possible to know which evaluation is correct in absence of the experimental data. The purpose of this paper is to report new $^{70}$Zn($n, \gamma$)$^{71}$Zn$^{m}$ (3.96 ± 0.05 hrs) cross sections experimentally determined at incident neutron spectrum averaged energies of 0.96 and 1.69 MeV to achieve improvement in our knowledge of this capture reaction in the MeV region. Therefore, the present result in this energy region will resolve this issue. The cross section for the $^{70}$Zn($n, \gamma$)$^{71}$Zn$^{m}$ has not been measured in the past in the MeV region. There are few data measured for a thermal and epithermal region using reactor neutrons. This may be due to the fact that the natural abundance of $^{70}$Zn is only 0.61 % and the enriched isotope is very costly.

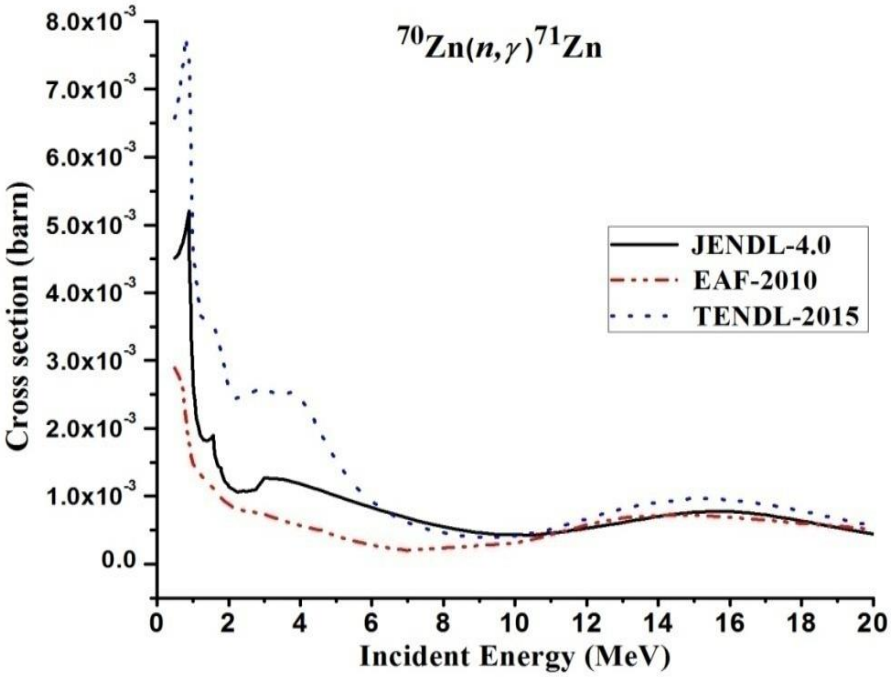


**Figure 2:** Comparison of different evaluated files from IAEA-ENDF for the $^{70}$Zn(*n*, $\gamma$)$^{71}$Zn reaction in the energy range 0.4 - 20 MeV.

### 1.2. Radiative Capture

In *radiative capture,* the incident neutron is captured by the target nucleus forming a compound nucleus which then decays to its ground state often through several intermediate states, thereby emitting one or more high energy gamma rays. The Illustration of radiative capture is shown in the **Figure 3**. An example of a radiative capture reaction is shown below.

$$_{0}^{1}\boldsymbol{n} + {}_{30}^{70}\boldsymbol{Zn} \rightarrow \left({}_{30}^{71}\boldsymbol{Zn}\right)^{*} \rightarrow {}_{30}^{71}\boldsymbol{Zn} + \boldsymbol{\gamma}$$

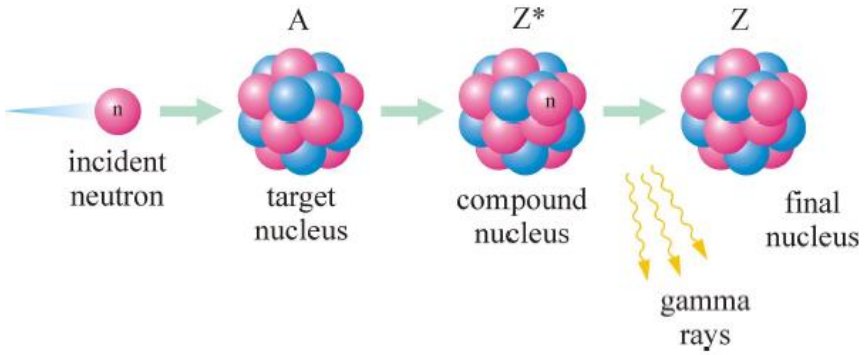


**Figure 3:** Illustration of (*n, γ*) reaction.

It is believed that the radiative capture reaction proceeds through the formation of an excited compound nucleus and subsequently decays by emitting one or several gamma-rays, *i.e.*,

$$(Z, A) + n \rightarrow (Z, A + 1)^* \rightarrow (Z, A + 1) + \gamma \, .$$

Where (Z, A + 1)* is the compound nucleus generated during the process. The formation of the compound nucleus and the emission of the gamma rays is represented in **Figure 4**.

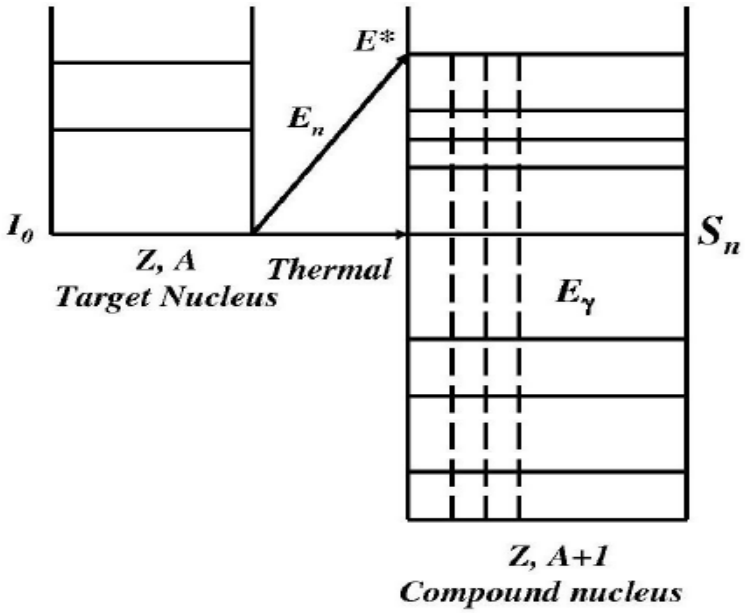


**Figure 4:** Scheme of the radiative capture process resulting in the formation of a compound nucleus. The neutron is captured into an unbound state above the neutron separation energy, Sn.

After the neutron capture, the compound nucleus is excited to a level with an energy given by,

$$E^* = S_n + E_n - - - - (1);$$

where $S_n$ is the neutron separation energy of the nucleus (Z, A+1) and $E_n$ is the energy of the incident neutron. The generated compound nucleus decays after a very short time ~ $10^{-14}$ s by the emission of one or more gamma-rays to reach either in a metastable state, which is an excited energy level close to the ground state, or a ground state (Domingo-Pardo, 2004). As the incoming neutron was first absorbed by the nucleus to form a compound nucleus, the chance of neutron capture is different for each target nucleus, depending on factors such as mass and spin. Therefore, the neutron capture cross section of an isotope can be defined as the probability of a reaction per incident neutron per target nucleus (Gicking, 2012).

### 1.3. Neutron Activation Analysis (NAA)

In 1936, the neutron activation analysis (NAA) was first developed by G. Hevesy and H. Levi. They found that the samples containing certain rare earth elements after exposure to a source of neutrons become highly radioactive. From this observation, they recognized that NAA is a powerful sensitive analytical technique to analyze the sample, *i.e.*, to identify the elements present in the unknown samples both qualitatively and quantitatively by measuring the induced radioactivity. Due to its accuracy and reliability, NAA is usually used as an important reference for other analysis methods (Verma, 2007).

The NAA technique is based on the principle of detecting and measuring the gamma rays emitted by the radioactive isotopes transformed from the stable isotopic sample by irradiating it with neutrons in a nuclear reactor or using any other neutron source. During irradiation, most of the naturally occurring stable isotopic elements are

transformed into radioactive isotopes by neutron capture. According to the characteristic half-lives of the newly radioactive isotopes varying from seconds to years, it is so decay emitting the γ-radiations with specific energies. In order to identify the source of γ-radiations, the characteristic γ-rays emitted by radioactive isotopes are subsequently measured with semi-conductor γ-ray spectrometers. Since, γ-radiation of a specific wavelength(s) or energy(ies) is emitted by each radionuclide, the emitted γ-radiations are characteristic of the isotope formed and hence characteristic of the parent element (Verma, 2007; Bode and De Coeij, 1998). This emitted radiation is an imprint of the element, and the amount of radiation given off at certain energy is investigative of the amount of the element present in the sample.

The neutron activation analysis is extremely useful for the determination of concentration of trace and minor elements in many disciplines. These include environmental sciences, nutritional and health related studies, geological as well as archaeological sciences, nuclear data measurements, material and forensic sciences. The most suitable source of neutrons for NAA is a research reactor (IAEA-TECDOC, 2001).

### 1.3.1. Basic Principles of NAA

The principle of neutron activation analysis is the nuclear reaction, specifically the neutron capture and subsequent gamma radiation emission through β-decay, called ($n, \gamma$) reaction. The radiative neutron capture has the high probability for thermal (energy ~ 0.025 eV) neutrons and for elements having large cross sections. The sequence of events occurring during the nuclear reaction of neutron capture or ($n, \gamma$) reaction used for neutron activation analysis is shown in **Figure 5**.

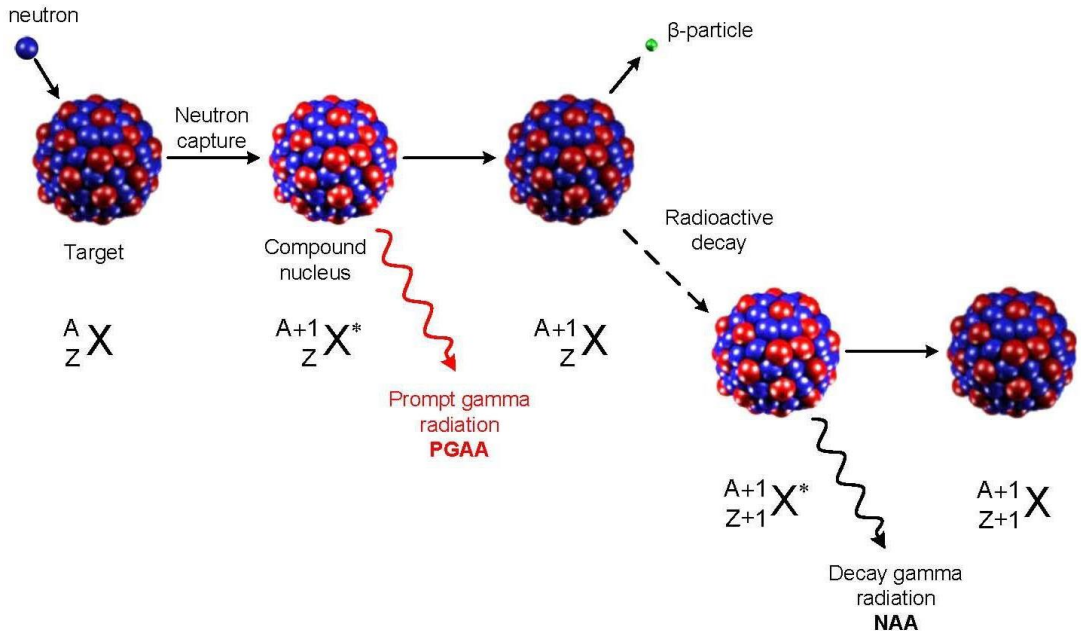


**Figure 5:** Diagram illustrating the process of neutron capture by a nucleus followed by the emission of gamma rays (Lylia Hamidatou *et al*., 2013).

In a neutron capture reaction, when the target nucleus absorbed an incident neutron through an inelastic collision, a compound nucleus is formed which is in the excited state. The compound nucleus excitation energy is due to the binding energy of the neutron with the nucleus. Then, the compound nucleus de-excites into either stable or radioactive. In the former case, during irradiation, de-excitation of compound nucleus occurs by emitting one or more characteristic prompt gamma rays. This type of NAA is called Prompt gamma ray NAA (PGNAA). The PGAA technique is usually performed by using neutrons beam extracted through a reactor beam port. In the latter case, a radioactive nucleus decays mostly by β-emission, the product nucleus which is being in the excited state may then de-excites (or decays) to its ground state by emission of one or more characteristic high energy delayed γ-rays. This type of NAA is known as Delayed gamma ray NAA (DGNAA). According to the type of neutrons used, NAA can be classified as thermal neutron activation analysis, epithermal neutron activation analysis, and fast neutron activation analysis.

The most advantage of PGNAA is the ability to obtain prompt gamma-ray spectra from excited compound nuclides of the neutron capture that do not produce radioactive isotopes through the (*n, γ*) reaction. This technique is most applicable to elements with very high neutron capture cross sections (B, Ni, P, S, Cd, Sm, and Gd); radioactive elements with a very short half-life which decay very quickly to be measured by DGNAA; elements that produce only stable isotopes; or radioactive elements with very low count rate (weak decay gamma-ray intensities). 2D, 3D analysis of (main) elements distribution in the samples can be performed by PGAA (Lylia Hamidatou *et al*., 2013).

DGNAA technique is useful for mostly of elements that produce radioactive nuclides. This technique is adjustable regarding with time so that the sensitivity for a long-lived radionuclide that undergoes interference by a shorter-lived radionuclide can be enhanced by waiting for the short-lived radionuclide to decay or quite the opposite, the sensitivity for short-lived isotopes can be increased by decreasing irradiation time to minimize the interference of long-lived isotopes. This selectivity is a key advantage of DGNAA over other analytical methods (Verma, 2007; Lylia Hamidatou *et al*., 2013). In the present work, the residual nucleus $^{71}Zn^{m}$ has the half-life of 3.96 ± 0.05hrs and we adopted DGNAA technique.

### 1.3.2. Activation Equation

Consider the neutron capture reaction, in which the target sample is bombarded by neutrons. The product nuclide can be either stable or radioactive. In the former case, only prompt gamma de-excitation occurs. In the latter case, the radioactive nuclei undergo *β*-decay emitting delayed γ-rays which can be detected by using the HpGe detector and is eventually transformed into a stable nuclide. The rate of change of

radioactive nuclides during irradiation is governed by the expression (Yit-Fong Chan, 2012):

$$\frac{dN(t)}{dt} = (rate\ of\ production) - (rate\ of\ decay)$$

$$= (\phi\sigma N) - \lambda N(t) - - - (2),$$

where, N is the number of target nuclei in the sample; $N(t)$ is the number of isotopes produced during irradiation; $\sigma$ is the neutron capture cross section of the reaction or is a probability of a neutron being captured by a nucleus; $\phi$ is the neutron flux; $\lambda$ is the decay constant of radioactive nuclei produced.

Multiplying **Eq. (2)** by λ and rearranging we get,

$$\frac{d[\lambda N(t)]}{[\lambda N(t) - N\sigma\phi]} = -\lambda dt - - - (\mathbf{3})$$

Integrating **Eq. (3)**, we get,

$$\ln(\lambda N(t) - N\sigma\phi)|_0^N = -\lambda t|_0^t$$

$$\frac{[\lambda N(t) - N\sigma\phi]}{-N\sigma\phi} = e^{-\lambda t}$$

Therefore, the **Eq. (2)** becomes:

$$N(t) = \frac{N\sigma\phi}{\lambda}\left(1 - e^{-\lambda t}\right) - - - (\mathbf{4}).$$

The activity of the product nuclei, $A_\gamma$ at the end of irradiation is given by:

$$A_\gamma = N\sigma\phi\left(1 - e^{-\lambda t}\right) - - - (5).$$

The activity $A_\gamma$ of a reaction product at any time is related to counting rate $A_C$ in one of its characteristic photo-peaks which is given by:

$$A_\gamma = \frac{A_C\lambda}{\varepsilon_p f_s f_d} - - - (6),$$

where, $\varepsilon_p$ is the photopeak detection efficiency of the detector; $f_s$ is the source self-absorption correction, and $f_d$ is the photon disintegration probability.

Let $t_1$ be the time elapsed during irradiation of the sample (irradiation time), $t_2$ is the time elapsed between the end of irradiation and the start of counting (cooling or delay time), and $t_3$ be the length of counting time. During irradiation, there is a build-up in activity. **Figure 6** shows the behavior of activated neutron sample. Considering correction for decay during counting interval $t_3$ , the number of counts (count rate) detected is:

$$A_C = \left[N\sigma\phi\varepsilon_p f_s f_d\left(1 - e^{-\lambda t_1}\right)e^{-\lambda t_2}\left(1 - e^{-\lambda t_3}\right)\right]/\lambda \quad ---(7).$$

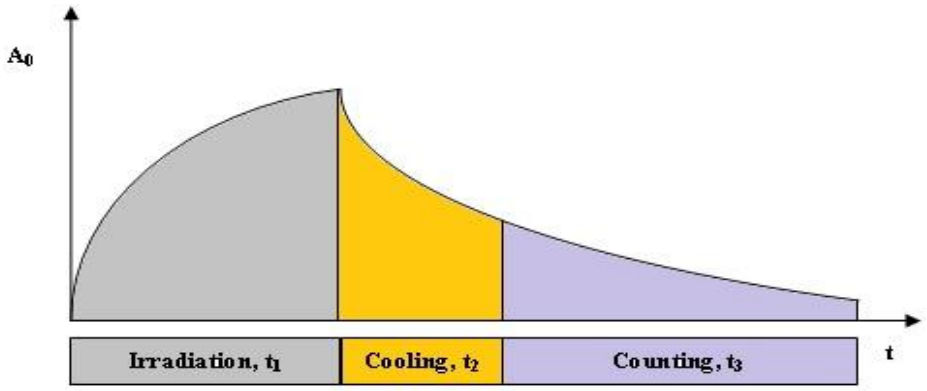


**Figure 6:** Activity build-up as a sample is irradiated to $t_1$ . Counting measurements taken between $t_2$ and $t_3$.

Cross sections were estimated using the above equation of activation formula. The count rates were corrected for coincidence effects, for γ-ray abundance, γ-ray self-absorption, an efficiency of the detector, and measurement geometry, neutron flux fluctuations during the irradiations, and the background neutrons.

The cross section $\sigma$ of a neutron-induced nuclear reaction can be estimated relative to the well-known cross section $\sigma_m$ of the monitor reaction using the following relation;

$$\sigma = \sigma_m \frac{A_C N_m \phi \varepsilon_m f_{s,m} f_{d,m}(1 - e^{-\lambda_m t_1})e^{-\lambda_m t_2}(1 - e^{-\lambda_m t_3})}{A_{C,m} N \phi \varepsilon f_s f_d (1 - e^{-\lambda t_1})e^{-\lambda t_2}(1 - e^{-\lambda t_3})} \quad ---(8),$$

where, *A* is the number of counts under the photo peak. The quantities with the subscript 'm' are for the monitor reaction.

The commonly used monitor reactions are $^{197}$Au(*n, γ*)$^{198}$Au , $^{115}$In(*n, n'*)$^{115}$In$^{m}$ $^{27}$Al(*n, p*)$^{27}$Mg, $^{27}$Al(*n, α*)$^{24}$Na, $^{56}$Fe(*n, p*)$^{56}$Mn, $^{93}$Nb(*n, 2n*)$^{92}$Nb$^{m}$, etc.

Although the activation technique is simple and efficient as compared to other techniques, one of the limitations is that it cannot be used for reactions whose product nuclei are stable.

### 1.4. Review of Literature

Reifarth *et al*. (2012) measured the neutron radiative capture cross sections of $^{64}$Zn, $^{68}$Zn, and $^{70}$Zn with the activation technique in a quasi-stellar neutron spectrum via the $^{7}$Li(*p, n*)$^{7}$Be reaction corresponding to a thermal energy of $kT$ = 25 keV. By repeating the irradiations several times with different experimental conditions, it could be achieved on the uncertainty of 3% for the $^{64}$Zn(*n, γ*)$^{65}$Zn cross section and for the partial cross section $^{68}$Zn(*n, γ*)$^{69}$Zn$^{m}$ feeding the isomeric state in $^{69}$Zn. For the partial cross sections of $^{70}$Zn(*n, γ*)$^{71}$Zn$^{m}$ and $^{70}$Zn(*n, γ*)$^{71}$Zn$^{g}$, which had not been measured so far, uncertainties of only 16% and 6% could be reached because of limited counting statistics and decay intensities. He compared the present results to the previous measurements on $^{64}$Zn and $^{68}$Zn, and then, he found that the uncertainties could be significantly improved, while the $^{70}$Zn cross section was found to be two times smaller than existing model calculations. From these results, Maxwellian average cross sections were determined between 5 and 100 keV. Additionally, the *β*-decay half-life of $^{71}$Zn$^{m}$ could be determined with significantly improved accuracy. By network calculations, he studied the results of these data for convective core He burning and convective shell C burning in massive stars.

Mannhart *et al.*, (1967) determined thermal capture cross sections and isomeric cross section ratios in thermal neutron capture for even-even nuclei in the region of the $2P_{1/2} - 1g_{9/2}$ neutron shell. They measured capture cross sections for formation of $^{71}Zn^{m}$ and $Zn^{71}$ by the activation method using $^{197}Au(n, \gamma)Au^{198}$ as a monitor with the cross section as 98.5 ± 0.4 b. From these data and additional measurements of cross section ratios, the isomeric ratios were also determined for thermal capture in $^{70}Zn$. Then, the isomer ratios were compared with calculations based on the statistical model of HUIZENGA and VANDENBOSCH. The measured thermal neutron capture cross sections for the $^{70}Zn(n, \gamma)^{71}Zn^{m}$ and $^{70}Zn(n, \gamma)^{71}Zn$ are 0.0081 ± 0.0005 % b and 0.083 ± 0.005 % b.

Mangal *et al*. (1962), measured thermal neutron capture cross sections for the $^{70}Zn(n, \gamma)^{71}Zn^{m}$ and $^{70}Zn(n, \gamma)^{71}Zn$ using activation technique by making irradiation with the "Swimming pool" reactor at Trombay, Bombay. Near the core, the zinc oxide film was irradiated, because 14 h irradiation in the thermal column failed to give 3 h activity. The sample activity was studied for 10 h, after it had decayed for 8 h to allow $^{69}Zn$ activity to decay. The decay curve consisted of two activities. The 14 h activity observed due to conversion electrons of $^{69}Zn^{m}$ when subtracted from the total activity gave an activity which decayed with a half-life of 3 h. This was attributed to $^{m}Zn^{71}$. In such cases, the neutrons flux at the point of irradiation was of the order of $10^{11}$ neutrons per $cm^2 \cdot sec^{-1}$. The sample was irradiated every time, either in the thermal column or near the core, the flux was calibrated simultaneously with the help of the standard reaction as reactor calibration was not so sensitive. An end window $\beta$-counter was used for nuclei which decay through $\beta$-particle emission. The $^{55}Mn(n, \gamma)Mn^{56}$ reaction was taken as the standard, with cross section as 13.4 ± 0.3 b. The measured thermal neutron capture cross sections for the $^{70}Zn(n, \gamma)^{71}Zn^{m}$ and $^{70}Zn(n, \gamma)^{71}Zn$ are 9 ± 20 % mb and

111 ± 20 % mb, and isomeric cross section ratios for target nuclei of spin 0 *i.e.*, $^{71}Zn^{m}$ / $^{70}Zn^{71}$ is 0.041 ± 0.017 with competing levels of $\frac{9}{2}/\frac{1}{2}$.

Cohen *et al*. (2005), measured the reactor thermal neutron capture cross section for the resonance integrals of the reactions $^{70}Zn(n, \gamma)^{71}Zn$ and $^{70}Zn(n, \gamma)^{71}Zn^{m}$, referred to the tabulated value for the resonance integral of the $^{68}Zn(n, \gamma)^{69}Zn^{m}$ reaction with cross section as 0.24 ± 0.03 b. No previous data were found on the discriminated resonance integrals for the capture reactions on $^{70}Zn$. The experimental results were 0.1350 ± 0.0093 b, for the $^{70}Zn(n, \gamma)^{71}Zn$ reaction (average of four measurements) and 0.157 ± 0.029 b for the $^{70}Zn(n, \gamma)^{71}Zn^{m}$ reaction, the latter corresponding to a single measurement of the resonance integral. As they did not perform any corrections for the departures from the ideal behaviour of the epithermal flux, and literature data on the mean effective resonance energy were lacking for these reactions, these results should be considered as informative or working values, only. The mean values of the epithermal flux per unit ln *E*, as measured the reaction $^{68}Zn(n, \gamma)^{69}Zn^{m}$, which was used as internal standard, was $8.4\times10^{10}$ n $cm^{-2}$ $s^{-1}$ respectively.

Krane (2017) measured the radiative thermal neutron capture cross sections $^{70}Zn(n, \gamma)^{71}Zn^{m,g}$ reaction. Irradiations were done in the TRIGA reactor of the Oregon State University Radiation Center. Several different irradiation sites were used: one in the central core, which also featured a Cd-lined facility to absorb thermal neutrons (nominal thermal and epithermal fluxes of $9.0\times10^{12}$ and $1.2\times10^{12}$ neutrons $cm^{-2}s^{-1}$); a fast pneumatic transfer facility (rabbit) located in the outer ring of the core ($4.4\times10^{12}$ and $3.4\times10^{11}$ neutrons $cm^{-2}$ $s^{-1}$); and a thermal column located behind graphite shielding about 2 m from the core ($7.8\times10^{10}$ and $2.0\times10^{8}$ neutrons $cm^{-2}s^{-1}$). All of the irradiations for the cross section measurements were accompanied by Au and Co as dilute impurities in aluminum foils which served as flux monitors.

In order to facilitate corrections for the epithermal neutron component, the resonance integrals were also measured. He also determined the cross sections for $^{64}Zn(n, \gamma)^{65}Zn$ and $^{68}Zn(n, \gamma)^{69}Zn^{m}$ reactions. The γ rays from the irradiated samples were observed with high-resolution Ge detectors (efficiency 35–40% compared with NaI at 1332 keV, resolution 1.7–1.8 keV at 1332 keV). Through high-resolution γ-ray spectrometry in the $^{71}Zn^{m}$ decay, a new set of γ-ray energies and intensities was obtained of roughly an order of magnitude greater precision than the previous set, and several transitions new to the decay scheme are proposed. The implications for the properties of the levels of $^{71}Ga$ were discussed. More precise values of the decay half-lives for $^{69}Zn^{m}$, $^{71}Zn^{g}$, and $^{71}Zn^{m}$ were determined.

# CHAPTER 2

# EXPERIMENTAL DETAILS

# 2. EXPERIMENTAL DETAILS

## 2.1. Neutron Source

The experiment was performed at the Folded Tandem Ion Accelerator (FOTIA) Facility, Nuclear Physics Division, Bhabha Atomic Research Centre (BARC), Mumbai. Schematic layout and photographs of the Folded Tandem Ion Accelerator (FOTIA) are shown in **Figures 7, 8(a) & (b)**. The protons at 2.80 and 3.50 MeV after passing through a beam collimator (0.5 cm in diameter) bombarded a 2.0-mg/cm$^2$ (37.4 μm) thick natural lithium target to produce neutrons through the $^7$Li(*p, n*)$^7$Be reaction ($E_{th}$ = 1.881 MeV). The proton beam energy spread is ± 0.02 MeV. A fresh lithium target was used for irradiation at each proton energy. The lithium targets were supplied by the Tata Institute of Fundamental Research

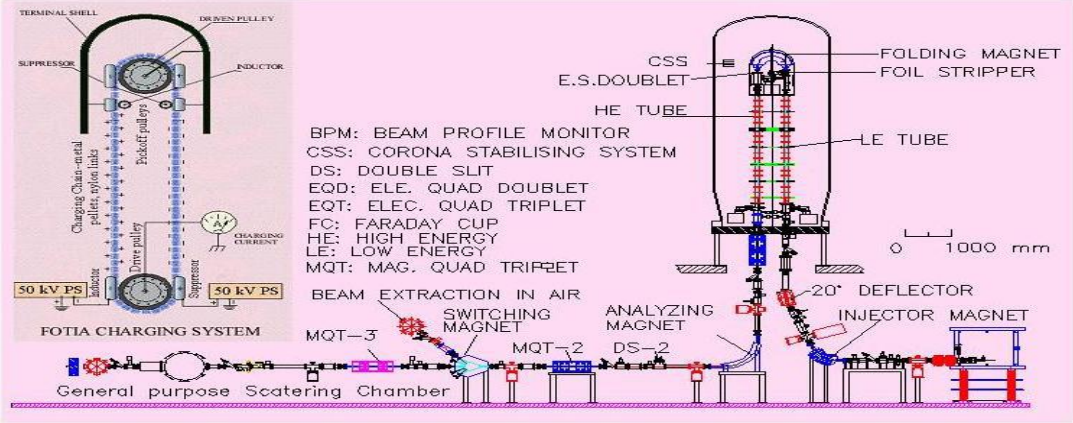


**Figure 7:** Schematic Layout of the Folded Tandem Ion Accelerator (FOTIA)

**Figure 8(a):** A wide view photograph of FOTIA

**Figure 8(b):** A close view photograph of FOTIA

(TIFR), Mumbai, and prepared using the rolling method at TIFR. A 0.25-mm thick tantalum foil (manufactured by Goodfellow Cambridge Limited, England, and supplied by H. Fillunger & Co. Pvt. Ltd., Banglore) on which the lithium target was pasted was used as a proton beam stopper. The proton beam current during irradiation varied from 50 to 100 nA, and the beam diameter on the lithium target was about 5 mm. The neutron flux was monitored online by an NE213 (shown in **Figure 10**) neutron detector at zero degree and at 1 m distance from the lithium target. The neutron flux was recorded and saved every 30 minutes to get the neutron flux fluctuation during the whole irradiation period. The experimental setup is schematically shown in **Figure 9(a)** and photographs in **Figures 9(b)** & **(c).**

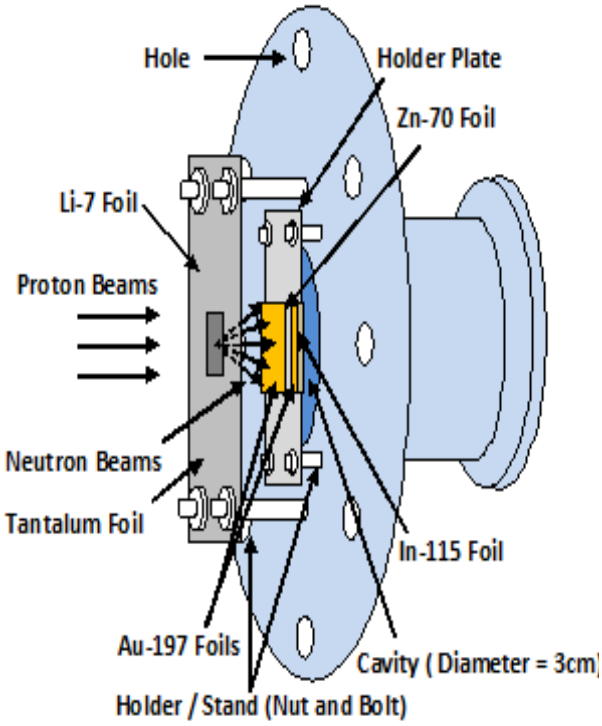


**Figure 9(a):** The schematic diagram of the Experimental Setup-1.

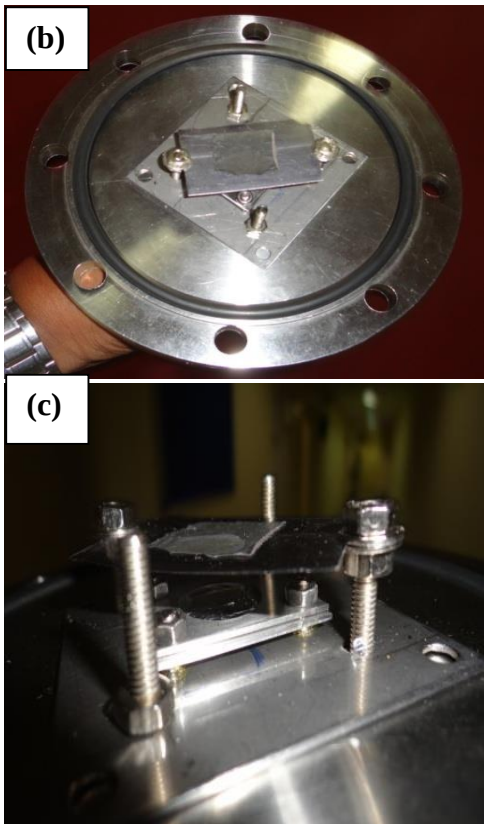


**Figure 9(b)** & **(c):** The photographs of Experimental Setup-1.


**Figure 10:** Experimental Setup-1: NE213 neutron detector at zero degree kept at 1 m distance from the lithium target.

The proton beam was continuous, and therefore TOF technique cannot be employed to measure the neutron flux energy spectrum. We, therefore rely on the $^{7}$Li(*p, n*)$^{7}$Be neutron flux energy spectrum code EPEN (R. Pachuau *et al*., 2017a, 2017b) developed at our laboratory to obtain the neutron flux energy spectra φ(E) for various lithium target configurations based on the $^{7}$Li(*p, n*)$^{7}$Be cross section evaluated by H. Liskien and A. Paulsen (Liskien *et al*., 1975) for proton energy of 1.95 - 4 MeV and Macklin and Gibbons (Macklin *et al*., 1958) for below 1.95 MeV up to threshold (1880.429 keV). The neutron flux energy spectra φ(E) calculated by EPEN at the two proton energies in the present experimental configuration are shown in **Figures 11** and **12**. It can be seen that the neutron energy is quasi-monoenergetic due to the proton energy loss in the lithium target and also due to the finite angular coverage of the neutron capture reaction target in the experimental setup. Since the proton energies in the present experiment are above the threshold energy of the $^{7}$Li(*p, n*$_1$)$^{7}$Be reaction (2.37 MeV), there are (*p, n*$_1$) low energy background neutrons in addition to the (*p, n*$_0$) neutrons, and their contribution should be known for subtraction. The mean energy of the (*p, n*$_0$) neutron group was obtained by

$$\langle E_n \rangle = \int \varphi_0(E)\, E dE \Big/ \int \varphi_0(E)\, dE \quad --- (9)$$

with the EPEN ($p$, $n_0$) neutron flux energy spectrum $\varphi_0(E)$, and it is 0.96 and 1.69 MeV for $E_p$ = 2.80 and 3.50 MeV, respectively. The width of the ($p$, $n_0$) spectrum is ± 0.15 MeV at both proton energies. The neutron flux energy spectra are plotted in **Figures 11** and **12.**

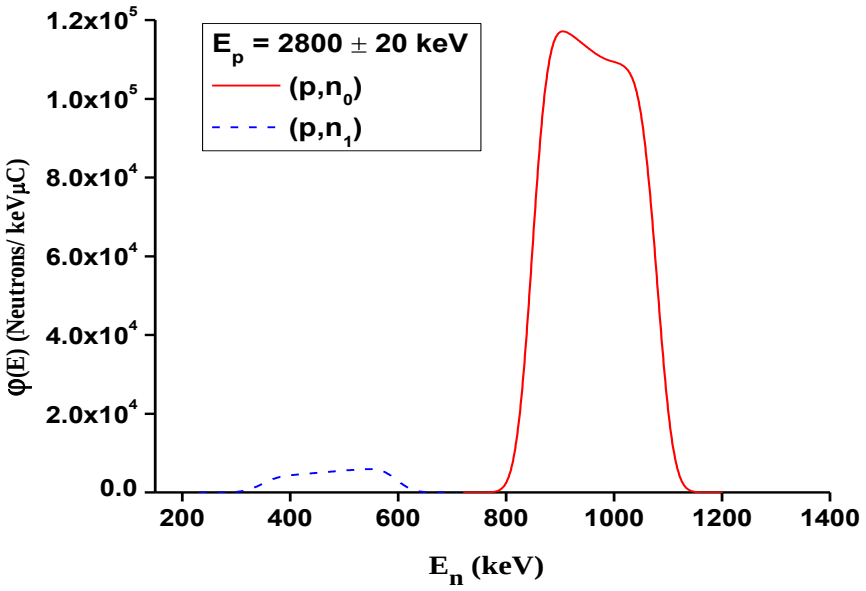


**Figure 11:** Neutron flux energy spectrum φ(E) from the $^7$Li($p$, $n_0$)$^7$Be and$^7$Li($p$, $n_1$)$^7$Be reaction at $E_p$ = 2.80 ± 0.02 MeV obtained from the code EPEN.

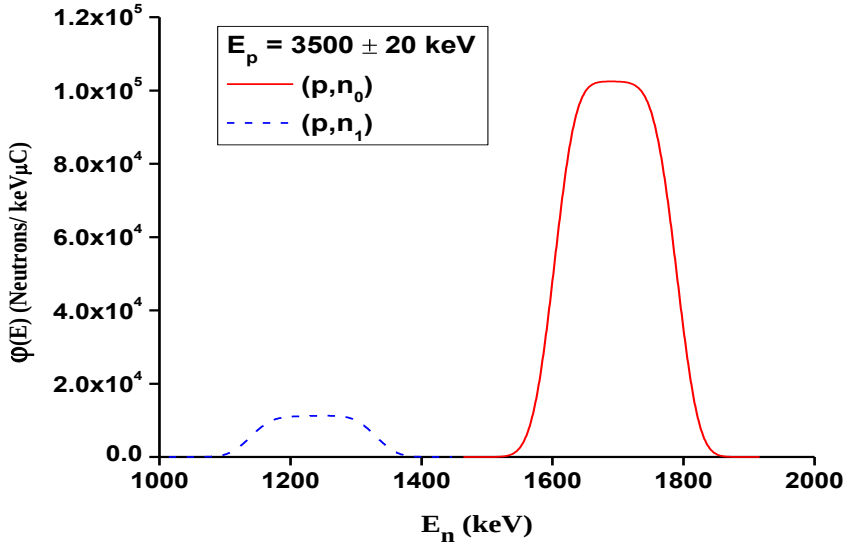


**Figure 12:** Neutron flux energy spectrum φ(E) from the $^7$Li($p$, $n_0$)$^7$Be and $^7$Li($p$, $n_1$)$^7$Be reaction at $E_p$ = 3.50 ± 0.02 MeV obtained from the code EPEN.

## 2.2. Sample Preparation

A zinc foil enriched (72.4 ± 1.0%) to $^{70}$Zn (manufactured by FUSE "Integrated Plant Electrohimpribor", Russia, and supplied by AMT Ventures Pvt. Ltd.) was sandwiched between gold foils (manufactured by Goodfellow Cambridge Limited, England, and supplied by H. Fillunger & Co. Pvt. Ltd., Banglore). The gold foils were used for normalization of the measured cross section with the $^{197}$Au($n$, $\gamma$)$^{198}$Au standard cross section. Furthermore, another natural indium foil (provided by BARC) was stacked at the end of the foil stack to serve as an independent flux monitor foil using the $^{115}$In($n$, $n'$)$^{115}$In$^{m}$ reaction for cross-checking. The whole stacked foils (10 mm × 10 mm) were wrapped with a 0.025 mm-thick superpure aluminium foil. The Au-Zn-Au-In stack was mounted at zero degree with respect to the beam direction at a distance of 14 mm from the lithium target. All foils were weighted at TIFR with an accuracy of 0.1 mg. Details of foils used in the present work are shown in **Table 1**.

**Table 1:** Details of foils used in the present experiment.

| **Isotope** | **Enrichment (%)** | **Purity (%)** | **$E_n$ (MeV)** | **Thickness (mg/cm$^2$)** | **Number of atoms of the isotope ($10^{-4}$ atoms/b)** |
|---|---|---|---|---|---|
| $^{70}$Zn | 72.4 ± 1.0<br>8.49 ($^{64}$Zn)<br>8.40 ($^{66}$Zn)<br>2.01 ($^{67}$Zn)<br>8.70 ($^{68}$Zn) | >99.97 | 0.96 | 87.3 ± 0.1 | 5.529 |
| | | | 1.69 | 113.6 ± 0.1 | 7.194 |
| $^{197}$Au | 100% | 99.95 | 0.96 | 72.3 ± 0.1 (front)<br>68.5 ± 0.1 (back) | 2.211 (front)<br>2.094 (back) |
| | | | 1.69 | 74.0 ± 0.1 (front)<br>70.3 ± 0.1 (back) | 2.263 (front)<br>2.149 (back) |
| $^{115}$In | 95.71% | 99.99 | 0.96 | 102.0 ± 0.1 | 5.120 |
| | | | 1.69 | 129.8 ± 0.1 | 6.516 |

### 2.3. Measurement of $\gamma$-ray Activity

After completion of the neutron irradiation and sufficient cooling, the foil stack was transferred to the counting room. The γ-ray activity was measured using a pre-calibrated lead-shielded 185 cc high purity germanium (HPGe) detector having 30% relative efficiency, and 1.8 keV energy resolution at 1.33 MeV γ-energy. The data acquisition was carried out using CAMAC based LAMPS (Linux Advanced Multi Parameter System) software (TCAMCON-95/CC 2000 crates controller and CM-48 ADCs). The HPGe detector set up is shown in **Figure 13**. Therefore, the detector dead time was negligible. To correctly identify the γ-ray of interest, the decay curve analysis was carried out by saving the γ count periodically as shown in **Table 2** and followed for 2 – 3 times the half-life of $^{71}Zn^{m}$. Details of decay data adopted in the analysis are given in **Table 3**. A typical γ-ray spectrum of the present experiment at $\langle E_n \rangle$ = 1.69 MeV is shown in **Figure 14**.

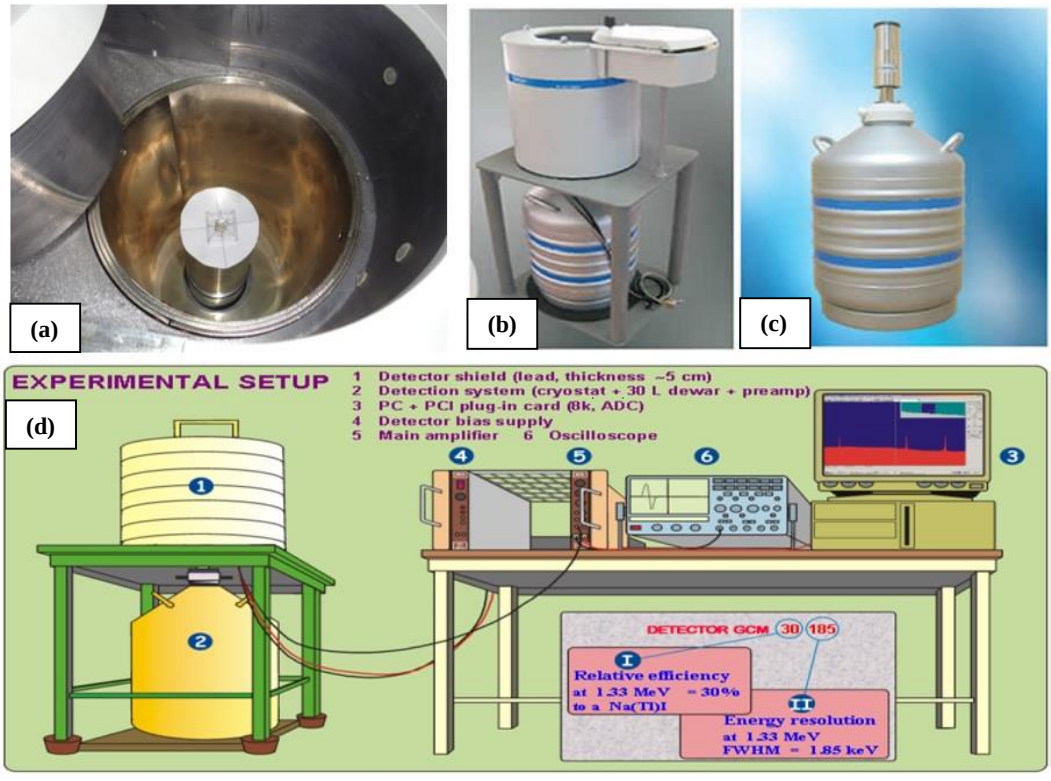


**Figure 13(a)-(d):** Experimental Setup-2 (HPGe Detector Setup).

**Table 2:** Irradiation, cooling and counting times.

| $E_n$ (MeV) | Irradiation time (sec.) | Run No. | Cooling time (sec.) (beam stop time-counting start time) | Counting time (sec.) |
|---|---|---|---|---|
| 0.96 | 26580.0 | 1 | 1808.0 | 3875.6 |
| | | 2 | 5705.6 | 3636.9 |
| | | 3 | 9373.5 | 7313.7 |
| | | 4 | 16746.2 | 7212.3 |
| | | 5 | 24012.5 | 1836.0 |
| 1.69 | 30300.0 | 1 | 1534.0 | 3591.2 |
| | | 2 | 5180.2 | 3634.3 |
| | | 3 | 8851.5 | 3616.9 |
| | | 4 | 12541.4 | 7253.3 |
| | | 5 | 20113.7 | 10368.6 |
| | | 6 | 30573.3 | 7950.3 |
| | | 7 | 38531.6 | 6353.3 |

**Table 3:** Decay data adopted in the present work taken from the ENSDF library (Abusaleem *et. al*., 2011, Xiaolong, 2009; Blachot, 2012).

| Nuclide | Half-life | $E_\gamma$ (keV) | $I_\gamma$ (%) |
|---|---|---|---|
| $^{71}Zn^m$ | 3.96 ± 0.05h | 386.280 | 91.40 ± 2.10 |
| $^{198}Au$ | 2.6947 ± 0.0003d | 411.802 | 95.62 ± 0.06 |
| $^{115}In^m$ | 4.486 ± 0.004h | 336.240 | 45.80 ± 2.20 |

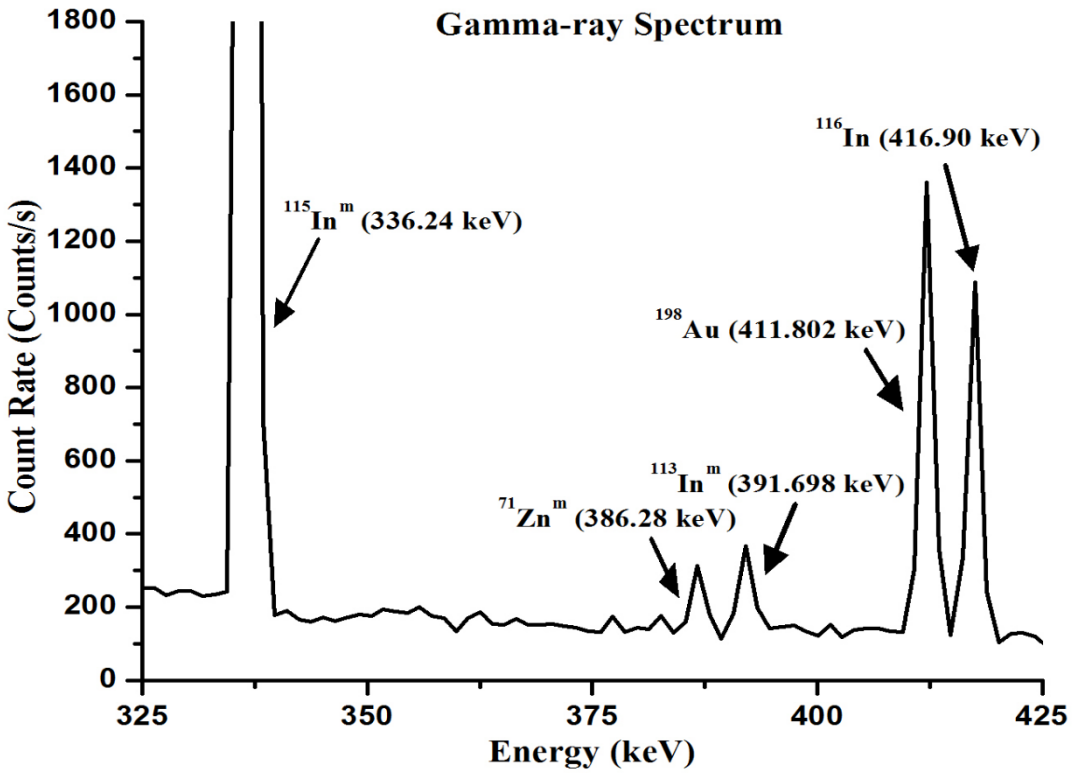


**Figure 14:** Typical γ-ray spectrum of radioactive nuclides $^{115}In^{m}$, $^{71}Zn^{m}$ and $^{198}Au$ at $<E_n>$ = 1.69 MeV.

### 2.4. HPGe Detector Energy Calibration

The energy calibration specifies the relationship between peak position in the spectrum (channel number) and the corresponding gamma-ray energy (*i.e.*, gamma-ray as a function of channel number). The energy calibration is accomplished by measuring the spectrum of a source emitting gamma-rays of precisely known energy and comparing the measured peak position with energy irrespective of the number of nuclides present in the source. This is normally performed before measuring the sample. Whatever source is used, it should be ensured that the calibration energies cover the entire range over which the spectrum is to be used. In practice, the spectrum should be measured long enough to achieve good statistical precision for the peaks to be used for calibration (Gilmore, 2008). The measured energies are only used to identify the nuclides and, thus, the uncertainty in the energy is no longer used in the

following calculations. The $^{152}$Eu point source ($T_{1/2}$ = 13.517 Years, Martin, 2013) of known activity, $A_0$ was used for energy calibration of the HPGe detector at its various characteristic gamma energies. The characteristics of the $^{152}$Eu point source used in the experiment are given in **Table 4.**

**Table 4:** Characteristics of the $^{152}$Eu point source.

| **Isotope** | **Activity on Reference Date [DPS]** | **Activity on Measurement Date (24.2.2013) [DPS]** | **Reference Date** | **Half-life [$t_{1/2}$ yrs.]** |
|---|---|---|---|---|
| $^{152}$Eu | 7582.5 | 3733.17 | 1.10.1999 | 13.517 ± 0.014 y |

### 2.5. HPGe detector efficiency calibration

Detection efficiency of a detector system depends on different parameters: the incident gamma ray energy, the detector crystal, the materials surrounding the detector crystal, the physical thickness of the detector in the direction of the incident radiation, the source to detector distance and geometry (Knoll, 2000). Three efficiencies can be considered depending upon how we wish to use it:

(i) Absolute total efficiency: it is the ratio of the number of gamma rays emitted by the source (in all directions) to the number of counts detected anywhere in the spectrum. This takes into account the full energy peak and all incomplete absorptions represented by Compton continuum (Gilmore, 2008).

(ii) Intrinsic efficiency: it is the ratio of the number of pulses recorded by the detector (counts in the peaks of the spectrum) to the number of gamma rays hitting the detector *i.e.*, the fraction of gamma rays recorded in the net full energy peak to the number of gamma rays incident on the detector. This efficiency of a detector is a detector property and is independent of source/detector geometry (Knoll, 2000).

(iii) Absolute full-energy peak (or photo-peak) efficiency: it is the ratio of the peak area in the spectrum, at a particular energy (counts in the full-energy peak), to the number of gamma-rays emitted by the source. It depends on the geometrical arrangement of source and detector. This parameter is the most significant in practical gamma-spectroscopy (Gilmore, 2008: Knoll, 2000).

A $^{152}$Eu point source of known activity ($A_0$ = 7582.5 Bq on 1$^{st}$ Oct.1999) was used for determination of the absolute photo-peak efficiency of the HPGe detector at various characteristic γ energies of the point source, because, its photon radiations cover the energy range of interest and also provide the highest possible accuracy. The spectrum obtained demonstrates that the $^{152}$Eu source was a long-lived multi-gamma-ray emitter with the gamma-rays being emitted over a wide range of energies. This spectrum emphasizes the ability of the HPGe detector to measure complex spectra and to distinguish gamma-rays with very close energies, in the limits of the values for the energy resolutions.

For the point source, the detector efficiency calibration consisted of determining a function describing the full-energy peak (FEP) detection efficiency versus the gamma-ray energies. For convenience, the peak efficiency was calibrated in terms of absolute efficiency. Based on the energy spectrum, the peak efficiency indicates the number of events detected in the full-energy peak over the total number of events emitted by the source. It relies upon several variables like the gamma energy, the detector qualities (dimensions, shape, material, etc.) and the source's relative arrangement (Peralta, 2004; Chandani, 2014). The detection efficiency for the point source placed at a distance of 1 cm from the detector $\varepsilon_p$ was determined by

$$\varepsilon_p = \varepsilon_I \varepsilon_G \quad - - - (10),$$

In the above equations, $\varepsilon_I$ is the intrinsic detection efficiency, $\varepsilon_G$ is the

geometric efficiency depending on the distance and shape of the source). A brief discussions for these parameters are given in the following **Sections 2.5.1** and **2.5.2.**

Since the count rate from the $^{70}Zn(n, \gamma)^{71}Zn^{m}$ reaction is rather low, we needed to place the foil stack very close to the detector to obtain high count rate. Therefore, the efficiency calibration source has also to be placed at the same distance, which is 1 cm from the detector. However, this introduces the coincidence-summing effect. Evaluations of the coincidence summing effect and detection efficiency are discussed in the following sections. Note that all parameters independent of γ energies are finally cancelled because we need only the ratio of detection efficiencies in the determination of the cross sections.

### 2.5.1. The Intrinsic Efficiency

Basically, the detection efficiency depends mainly on the characteristic of intrinsic factors of the detector and on the solid angle Ω subtended by the source at the detector face. The intrinsic detector efficiency is represented by **Eq.(11)** respectively as:

$$\varepsilon_i = 1 - e^{-\mu \overline{d}} - - - (11)$$

where $\mu$ is the attenuation coefficient of the detector active medium for a γ-ray photon with energy $E_\gamma$, $\overline{d}$ is the average path length traveled by a photon through the detector active volume for an isotropic emission and is represented by **Eq.(12)** respectively (Abbas, 2006):

$$\overline{d} = \frac{\int_\Omega \left(\sum_{j=1}^{n} d_j\right) d\Omega}{\int_\Omega d\Omega} = \frac{\int_\varphi \int_\theta \left(\sum_{j=1}^{n} d_j\right) \sin\theta d\theta \, d\varphi}{\Omega} - - - (12),$$

where, $d_1$, $d_2$, …, $d_n$ are the possible path lengths traveled by the photon within the detector active volume and $\theta$ and $\varphi$ are the polar and the azimuthal angles respectively.

Experimentally, the intrinsic efficiency can be determined by:

,

$$\varepsilon_I = \frac{CK_c}{A_0 e^{-\lambda t}\Delta t I_\gamma} - - - -(13),$$

where $C$ is the number of counts during the counting time ($\Delta t$ = 3607 sec), $A_0$ is the $^{152}$Eu source activity at the time of manufacture, $t$ is the time elapsed from the date of manufacturer to the start time of counting, $\lambda$ is the decay constant, $I_\gamma$ is the decay $\gamma$ intensity, $K_c$ is the correction factor for the coincidence summing effect, $d$ is the source to detector distance.

### 2.5.2. Geometric Efficiency

The detector efficiency is a function of the solid angle subtended by the source at the detector *i.e*., of the source-to-detector distance, and the areas of the detector and source front face. Generally, gamma rays are emitted equally in all directions thereby covering a solid angle Ω for a point source to the detector located along the axis of a right circular cylindrical detector. For an arbitrary detector and isotropic point source, the geometric efficiency can be defined as the fraction of solid angle subtended by the detector at the source position (Peralta, 2004):

$$\varepsilon_G = (1/4\pi)\int d\Omega = (1/4\pi)\int_A \frac{\vec{a}\bullet\vec{n}}{|r^3|} dA - - - (14)$$

where, $\vec{n}$ is a unitary vector perpendicular to the detector surface at each point and $\vec{a}$ the vector linking the point source to a detector elementary area d$A$. For an extended source, an extra integration must be brought out to cover all source points. For a cylindrical detector with a window of radius $r$ and a point source located in the symmetry axis at a distance $d$ from the detector as shown in **Figure 15**, the solid angle can be calculated as (Peralta, 2004):

$$\Omega = \int_\emptyset \int_\theta \sin\theta d\theta \, d\emptyset = \int_0^{2\pi} d\emptyset \int_{\cos\theta}^{1} d(\cos\theta') = 2\pi(1-\cos\theta) - - - (15)$$

where,

$$\tan\theta = \frac{r}{d},$$

and,

$$\cos\theta = 1/\sqrt{tan^2\theta + 1}$$

$$= d/\sqrt{r^2 + d^2}$$

and then, the solid angle for the point source is given by (Peralta, 2004; Damon, 2005):

$$\Omega = 2\pi\left[1 - d/(d^2 + r^2)^{1/2}\right] - - - (16),$$

where, *d* is the source to detector distance and *r* is the radius of the detector. A depiction of the solid angle is shown below for a point source located at distance *d* from a cylindrical detector with radius *r*.

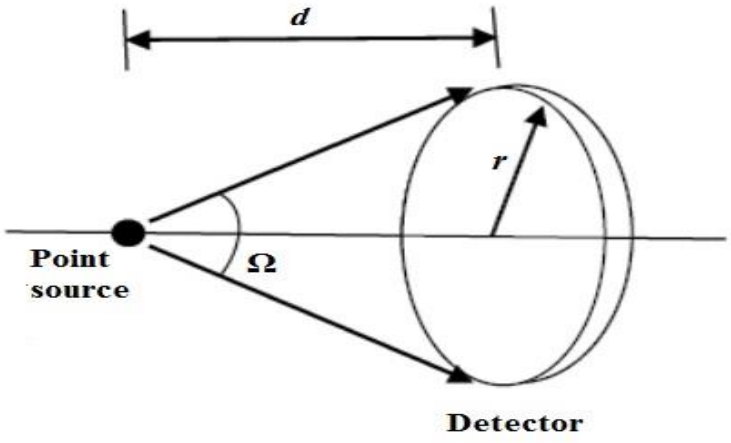


**Figure 15**: Geometric arrangement of $^{152}$Eu point source placed at the distance *d*.

Therefore, the geometric efficiency $\varepsilon_G$ can be defined as the ratio of the number of photons emitted towards the detector to the number of photons emitted by the source, and then, it is for a point source and cylindrical detector given by:

$$\varepsilon_G = \Omega/4\pi$$

$$= \left(\frac{1}{2}\right)\left(1 - \frac{d}{\sqrt{d^2 + r^2}}\right) - - - (14a)$$

For example:

Consider the point source placed above the detector crystal as follows:

(i) Distance of the source from the detector (d) =1 cm.

(ii) Radius of the circular detector (r) =2.865 cm.

Now, the solid angle for the point source is calculated by using **Eq. (16)** as

$$\Omega = 2\pi\left(1 - \frac{d}{\sqrt{d^2 + r^2}}\right)$$

$$= 2 \times 3.14\left(1 - 1/\sqrt{1 + (2.865)^2}\right)$$

$$= 4.2143$$

Finally, using **Eq. (14a)**, we get the geometric efficiency as:

$$\varepsilon_G = 4.2143/12.5714$$

$$= 0.3352$$

### 2.5.3. Coincidence Summing Effect

When two γ-rays emitted in a cascade are detected within the resolving time of the detector, the detector cannot distinguish between the two γ-rays, and thus giving rise to a single signal in the spectrum as if a single γ-ray would have been detected. This is known as "cascade" or "true coincidence" summing. This leads to (1) a loss in count ("summed out") from the peaks corresponding to two γ-rays, and (2) an addition of count ("summed in") at the sum of two energies. For any source-to-detector distance there will be some degree of summing depending on the detector size, beyond a certain distance, coincidence-summing losses will be negligible (Damon, 2005).

The **Figure 16** shows a simplified decay scheme for $^{152}$Eu. There can be two possible choices for the atoms of this nuclide when they decay; they can either emit $\beta^-$ particle and become $^{152}$Gd or, more likely (on 72.08% of events), undergo electron capture and become $^{152}$Sm. For both modes of decay, the daughter nucleus then de-

excited by emitting a number of gamma-rays in any of the decays schemes until a stable nucleus is formed. Moreover, the electron capture decay to $^{152}$Sm is likely to be accompanied by the emission of Sm X-rays. The lifetimes of the discrete nuclear levels are short, which are much shorter than the resolving time of the gamma spectrometer system. Every disintegration of a $^{152}$Eu atom in the source will release a number of gamma-rays and possibly X-rays, simultaneously. For the detector, there is a high probability that more than one of these within the resolving time of the detector will be detected together. In that case, a pulse will be recorded which represents the sum of the energies of the two individual photons detected together. This phenomenon is called True coincidence summing (TCS), *i.e.*, it is the summing of two gamma-rays emitted in coincidence, the event results in the loss of counts from the photo-peak and therefore a loss of photo-peak efficiency (Damon, 2005; Wissam, 2007; Gilmore, 2008).

The degree of TCS depends upon the probability that two or more coincident gamma rays emitted very nearly simultaneously will be detected simultaneously as a single count by the detector. This is a function of the geometry, of the solid angle subtended at the detector by the source and errors, are particularly severe when the sources are placed very close to the detector. It is noted that two gamma rays will be detected together decreases with increasing the distance between source and detector. So, it is understood that for any source-to-detector distance, there will be some degree of summing. Thus, the coincidence summing corrections can be avoided by counting the sample keeping far from the detector, so that the probability of two gamma rays reaching the detector at the same time will be negligible. So, in practice, depending on the detector size, TCS loses beyond a certain distance are negligible. This is quite impractical for the samples with the low activity where the samples are required to be

counted as close as possible to the detector. Another way to avoid coincidence summing corrections is to use a gamma ray standard as a monitor; the $^{152}$Eu, which is used in our works (Damon, 2005; Wissam, 2007; Gilmore, 2008). The evidence for coincidence summing is found in the gamma rays spectrum of the $^{152}$Eu point source shown in **Figure 17**. The photo-peaks corresponding to the combination of gamma-ray lines that are indicated in **Figure 17** is given in **Table 5**. In our experiment, since the count rate from the $^{70}Zn(n, \gamma)^{71}Zn^{m}$ reaction is rather low, we needed to place the foil stack very close to the detector to obtain high count rate.

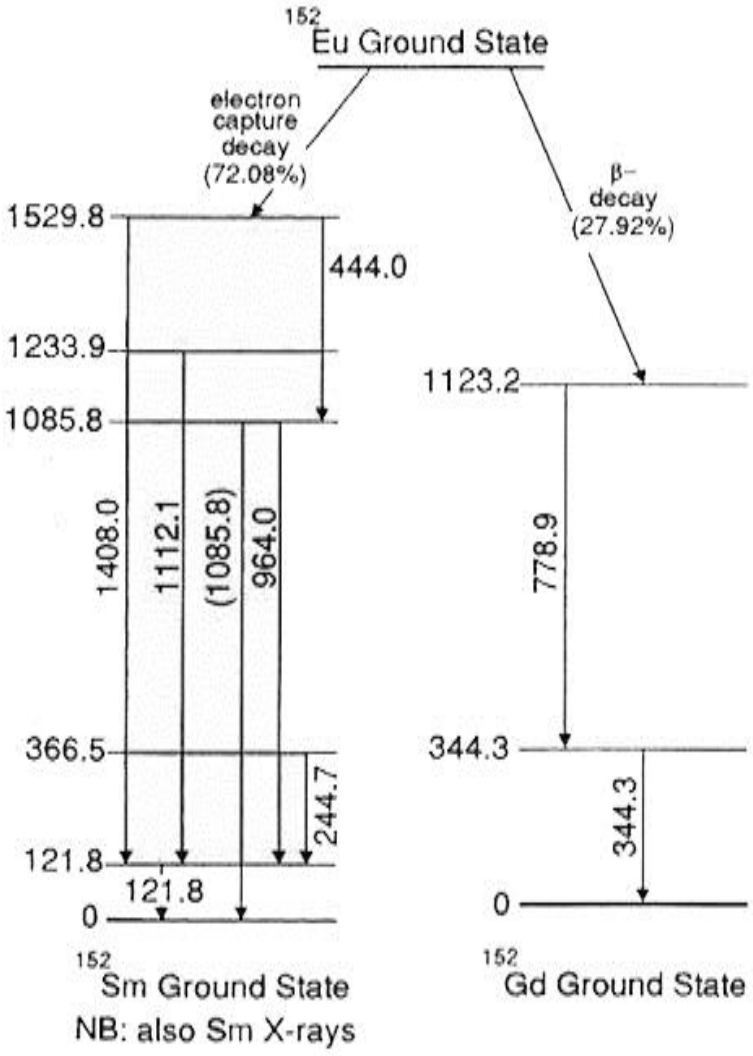


**Figure 16:** Simplified decay scheme for $^{152}$Eu (Gilmore, 2008).

**Table 5:** Combinations of gamma-rays (keV) of the $^{152}$Eu standard source that undergo coincidence summing. The yellow boxes indicate those peaks that undergo summing out and those green pale boxes, summing in.

| Coincidence Summing Out/In on Eu-152 | | | | |
|---|---|---|---|---|
| **keV** | **121.8** | **244.7** | **344.3** | **444.1** |
| **244.7** | **366.5** | | | |
| **444.1** | **565.9** | | | |
| **778.9** | | | **1123.2** | |
| **867.4** | | **1112.1** | | |
| **964.0** | **1085.8** | | | **1408.1** |
| **1085.8** | | | | |
| **1112.1** | **1233.9** | | | |
| **1408.0** | **1529.8** | | | |

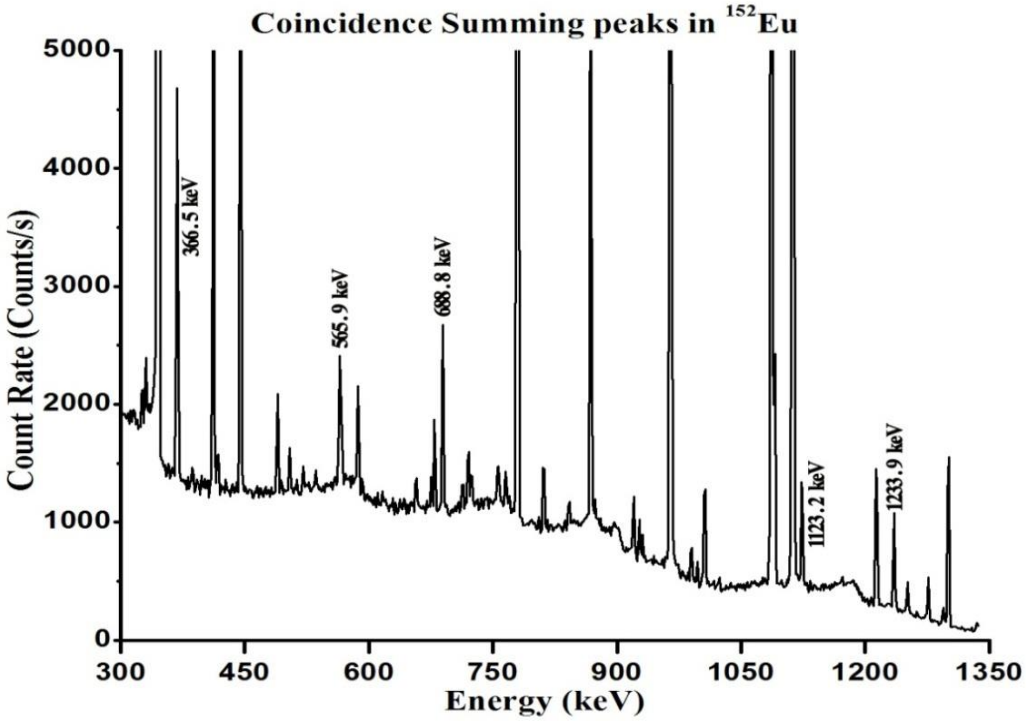


**Figure 17:** Sum peaks in the $^{152}$Eu standard source spectrum due to coincidence summing.

### 2.5.3.1. Mathematical Summing corrections

The coincidence summing correction factors can be calculated by using the methods of empirical, semi-empirical and theoretical. The empirical methods should be applied on the basis of the count rate ratio between close and far geometries of photons having similar energy. The semi-empirical methods should be based on the measurement of the detector total efficiency or the calculation of the total efficiency by measuring the full energy peak and the peak to total efficiencies. This method also requires the knowledge of the exact geometry (sample dimensions and materials) and detector dimensions. The theoretical methods are based on Monte Carlo simulation of the interaction of the photons with the detector, the shielding, and the sample materials. In these methods, there is no need of measuring any radioactivity but are sensitive to the exact value of the detector dimensions (Haquin, 2017).

In principle, mathematically it is possible to correct for TCS errors, the simplest possible decay scheme in which we could expect TCS is shown in **Figure 18**. It shows that the beta decay to one of the two excited states followed by the emission of the three gamma-rays. To simplify matters for the purposes of illustration, the internal conversion coefficients for the gamma-rays are all assumed to be zero (Gilmore, 2008).

According to Gilmore (2008), let the source activity be *A* Becquerels, in the absence of TCS, the count rate in the full-energy peak for $\gamma_1$ can be calculated as :

$$n_1 = Ap_1\varepsilon_1 - - - (17)$$

where, $p_1$ is the gamma emission probability and $\varepsilon_1$ is the full-energy peak efficiency of detection of $\gamma_1$, respectively. Similar equations, with the appropriate $p$ and $\varepsilon$, would be used to calculate the number of counts in the full-energy peak for $\gamma_2$ and $\gamma_3$.

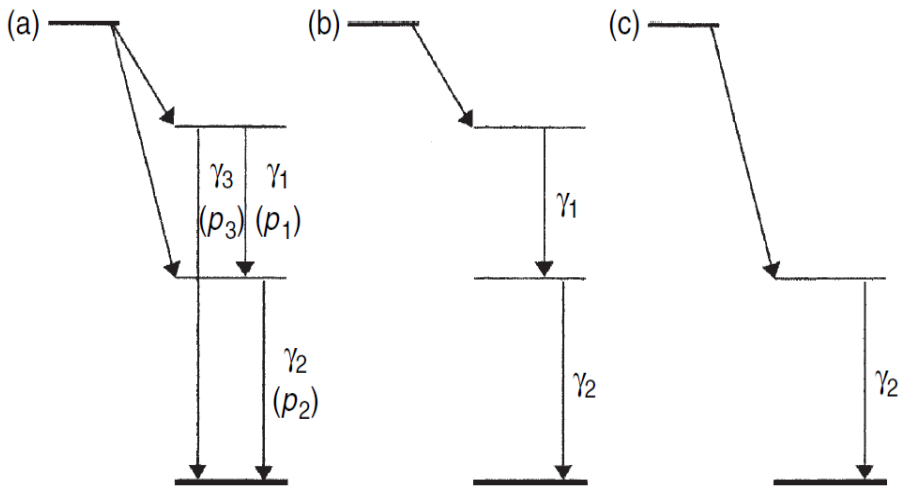


**Figure 18:** Simple illustrative decay schemes liable to true coincidence summing.

Now, we will lose the counts from the $\gamma_1$ peak due to summing of $\gamma_1$with $\gamma_2$. We do not need to consider $\gamma_3$ as de-excitation of the upper energy level can only give $\gamma_1$ or $\gamma_3$, not both and we only need the partial decay scheme in **Figure 18(b)**. The count rates (number of counts per second) lost by summing can be calculated as the product of:

- the number of atoms decaying (*A*)
- the probability of de-excitation producing $\gamma_1(p_1)$
- the probability of $\gamma_1$ being detected and appearing in the full-energy peak $(\varepsilon_1)$
- the probability of $\gamma_2$ being detected and appearing in the total-energy peak $(\varepsilon_{T2})$

Therefore, we must consider all the coincidences whether giving rise to a sum peak count or not and hence, the final term uses $\varepsilon_{T2}$, the total efficiency for the detection of $\gamma_2$. Hence, the net count rates for peak ***1*** would be:

$$n_1' = Ap_1\varepsilon_1 - Ap_1\varepsilon_1\varepsilon_{T2} - - - (18)$$

The ratio $n_1/n_1'$ would then be used to correct for the TCS losses of the $\gamma_1$ peak area.

$$C_1 = \frac{n_1}{n_1'} = \frac{1}{1-\varepsilon_{T2}} - - - (19)$$

For $\gamma_2$, the situation is slightly different in that, not all gamma-rays emerging from the intermediate energy level are a consequence of the de-excitation from the higher level. Some are emanated immediately by the $\beta^-$ decay and cannot contribute to summing (see **Figure 18(c)**). The number of summing events is then the product of:

- the number of events giving rise to $\gamma_2 (Ap_1)$
- the probability of detection of $\gamma_2$ in the full-energy peak $(\varepsilon_2)$
- the probability of the detection of $\gamma_1$ in the total-energy peak $(\varepsilon_{T1})$.

And so, the net count rate for the peak ***2*** would be:

$$n_2' = Ap_2\varepsilon_2 - Ap_1\varepsilon_2\varepsilon_{T1} - - - (20)$$

The ratio $n_2/n_2'$ would then be used to correct for the TCS losses of the $\gamma_2$ peak area, *i.e.*,

$$C_2 = \frac{n_1}{n_2'} = \frac{1}{1-(p_1/p_2)\varepsilon_{T1}} - - - (21)$$

Every true summing event of completely absorbed gamma-rays will produce a count in a peak equivalent to the sum of the energies and so the peak corresponding to the crossover transition. $\gamma_3$, will be increased in the area rather than decreased. Following the same reasoning as above, the net count rate would be:

$$n_3' = Ap_3\varepsilon_1 - Ap_1\varepsilon_1\varepsilon_{T2} - - - (22)$$

The summing correction that would be applied to correct for the TCS gains of the $\gamma_3$ peak area.

$$C_3 = \frac{n_3}{n_3'} = \frac{1}{1+(p_1\varepsilon_1\varepsilon_2/p_3\varepsilon_3)} - - - (23)$$

Often, the crossover transition probability is small and, because the emission probabilities for the normal cascade transitions are high, the summing-in can be much greater that the direct emission. Unless taken into consideration, the error from using peak areas due to this transition would be large (Gilmore, 2008).

In general, we cannot depend upon the internal conversion coefficients which was being negligible as were treated in the above simplified and we have considered a much simpler decay scheme than we can normally expect. If we examine instead the $^{152}$Eu decay scheme (which is more representative of the real situation), the correction for TCS becomes apparent. Then, we must not take into account only every possible $\gamma - \gamma$ coincidence, but also, the possibility of the coincidence of every cascade on the $^{152}$Sm side of the scheme with the Sm X-rays emitted (Gilmore, 2008).

The further complications occur if the source emits positrons. This is due to the presence of 511 keV annihilation quanta in coincidence with the gamma-rays coming from de-excitation of the daughter nucleus. For this problem, the analytical solution is to add a pseudo energy level to the decay scheme 511 keV above the level in which the positron emission leaves the daughter. Moreover, the triple coincidences between the most intense gamma-ray and bremsstrahlung coincidences lead to further complications. Obviously, in order to apply these calculations at all, we must have available a full-energy peak efficiency free of TCS errors and a total efficiency curve. According to the principle, the task is very ambitious, however, if the detailed decay scheme, adequate full energy peak efficiency data, total efficiency data, complete conversion coefficient data and detailed knowledge of the sample are available, then a mathematical correction is possible (Gilmore, 2008).

Semkow *et al.*, 1990 developed the mathematical formula for the correction of coincidence summing and further simplified by De Felice *et al.*, 2000 which is given by **Eq. (24)** (Xhixha, 2012).

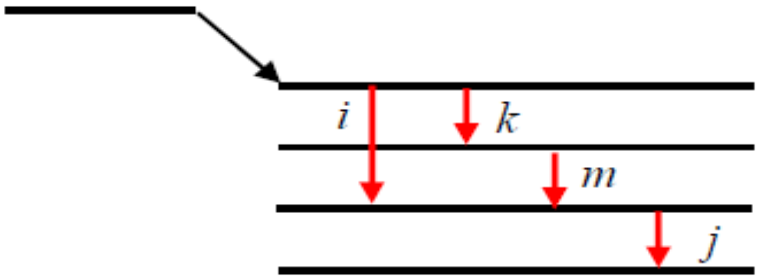


**Figure 19:** Simplified decay scheme showing the effect of summing in and out (Xhixha, 2012).

According to Xhixha (2012), considering a simple decay scheme shown in the above **Figure 19**, the coincidence summing of $\gamma - \gamma$ and $\gamma - KX$ (normally only KX-rays have sufficient energy to be observed by the HPGe detector) can be formulated as:

$$C_{CS(i)} = \left[1 - \frac{\sum_j P_{Tij} P_i P_j \varepsilon_{Tj}}{I_{\gamma i}}\right]\left[1 + \frac{\sum_{k,m} P_{Tkm} P_k P_m \varepsilon_k \varepsilon_m}{I_{\gamma i}\varepsilon_i}\right] - - - (24),$$

where $P_{Tij}$ is the probability of coincident transitions ($i$, $j$); $P_i$ is the probability of photon emission in transition $i$; $I_{\gamma i}$ is the photon emission probability; $\varepsilon_i$ is the full energy peak efficiency and $\varepsilon_{Tj}$ is the total efficiency.

The **Eq. (24)** can be simplified in a function of full energy photo-peak and total efficiencies as:

$$C_{CS(i)} = \left[1 - \sum_j C_j \varepsilon_{Tj}\right]\left[1 + \sum_{k,m} C_{k,m} \frac{\varepsilon_k \varepsilon_m}{\varepsilon_i}\right] - - - (25)$$

where, $C_j$ and $C_{k,m}$ can be calculated using the decay data. The gamma rays emission probability, $P_\gamma$, can be calculated as:

$$P_\gamma = \frac{1}{1+\alpha_T} - - - (26)$$

and transition probability of KX-rays, $P_{KX}$ emitted as a result of the internal conversion of the electron capture process can be calculated as:

$$P_{KX(i)} = \frac{\omega_K \alpha_{KX(i)}}{1+\alpha_{T(i)}} - - - (27),$$

where $\alpha_T$ is the total internal conversion coefficient; $\omega_K$ is the K-fluorescence yield for the daughter nuclide and $\alpha_{K(i)}$ is the K-conversion coefficient of transition *i*. For decay schemes with several transitions that decay by K-conversion, the total KX-ray emission probability is equal to the sum of the individual KX-ray emission probability of the transition (Xhixha, 2012).

The coincidence summing correction is normally ignorable when it depends upon the angular correlation between gamma rays averaged over the solid angle which for close source-to-detector distances. Subsequently, it has been neglected in this treatment. By considering the angular correlation between two gamma rays, the **Eq. (24)** & **(25)** must be re-written as (Xhixha, 2012):

$$C_{CS(i)} = \left[1 - W_{Tj}\frac{\sum_j P_{Tij}P_iP_j\varepsilon_{Tj}}{I_{\gamma i}}\right]\left[1 + W_{km}\frac{\sum_{k,m} P_{Tkm}P_kP_m\varepsilon_k\varepsilon_m}{I_{\gamma i}\varepsilon_i}\right] - - - (28),$$

where, $W$ is the angular correlation factor of two gamma rays. By using Legendre series, the angular correlation terms can be expanded as:

$$W(\theta)d\Omega = \sum_{i=1}^{L} A_{ij}P_{ij}(\cos\theta)d\Omega - - - (29)$$

where $A_{ij}$ are catalogued for some standard radionuclides by IAEA (*http://www-nds.iaea.org/*).

### 2.5.3.2. Software for Correction of TCS (EFFTRAN)

**Table 6** shows the $^{152}$Eu standard source characteristic γ energies and their corresponding γ intensities considered in the detector efficiency measurement. In order to correct the measured efficiency for the coincidence summing effect, the correction factor $K_c$ was calculated using the Monte Carlo simulation code EFFTRAN (Vidmar, 2005). We provided the detailed specifications of the HPGe detector (*e.g.*, dimensions and materials of the crystal, crystal hole cavity, end cap, window, mount cup, absorber) and $^{152}$Eu γ source (*e.g.*, dimension, material, characteristic γ- and X-rays) as inputs to the simulation. The simulation, therefore, takes care of γ-ray–γ-ray and γ-ray - X-ray coincidences. The detector efficiencies with and without the correction measured at the characteristic γ energies of the $^{152}$Eu point source are shown in **Figure 20**. All characteristic γ-lines are affected by the summed out effect while only those with higher energies are affected by the summed in effect as can be seen in **Table 6** where the γ-rays with lower energies, in general, have larger correction factors because the loss of their counts due to the summed out effect is not or less compensated by the summed in effect. Only the efficiency ratio is necessary for the determination of the cross sections, and therefore only the uncertainties in counting statistics and γ intensity were considered in the error propagation to the efficiencies of the $^{71}Zn^{m}$ and $^{198}$Au characteristic γ lines.

**Table 6:** Detection efficiencies for the point source geometry $\varepsilon_p$ and for the foil stack geometry ε at the characteristic γ energies of $^{152}$Eu with their γ intensities $I_\gamma$ (Martin, 2013) adopted for efficiency determination, counts C and coincidence summing effect correction factors $K_c$. The 444.0 keV γ-line consists of 443.96 keV ($I_\gamma$ = 2.827 ±

0.014%) and 444.01 keV ($I_\gamma$ = 0.298 ± 0.011%) unresolved by our detector. The uncertainty in ε is propagated from the uncertainties in C and $I_\gamma$.

| $E_\gamma$(keV) | $I_\gamma$(%) | C | $K_c$ | $\varepsilon_p$ | E |
|---|---|---|---|---|---|
| 121.8 | 28.53±0.16 | 328049.3 | 1.113 | 3.0514 | 3.0270 ± 0.0178 |
| 244.7 | 7.55±0.04 | 53997.8 | 1.158 | 2.0083 | 1.9940 ± 0.0136 |
| 344.3 | 26.59±0.20 | 157183.5 | 1.078 | 1.5550 | 1.5450 ± 0.0123 |
| 411.1 | 2.237±0.013 | 9647.2 | 1.193 | 1.2803 | 1.2720 ± 0.0149 |
| 444.0 | 3.125±0.018 | 13292.1 | 1.142 | 1.2087 | 1.2013 ± 0.0125 |
| 778.9 | 12.93±0.08 | 32542.8 | 1.112 | 0.6964 | 0.6922 ± 0.0058 |
| 1112.1 | 13.67±0.08 | 28712.2 | 1.033 | 0.5399 | 0.5368 ± 0.0045 |
| 1408.0 | 20.87±0.09 | 34940.8 | 1.050 | 0.4374 | 0.4349 ± 0.0030 |

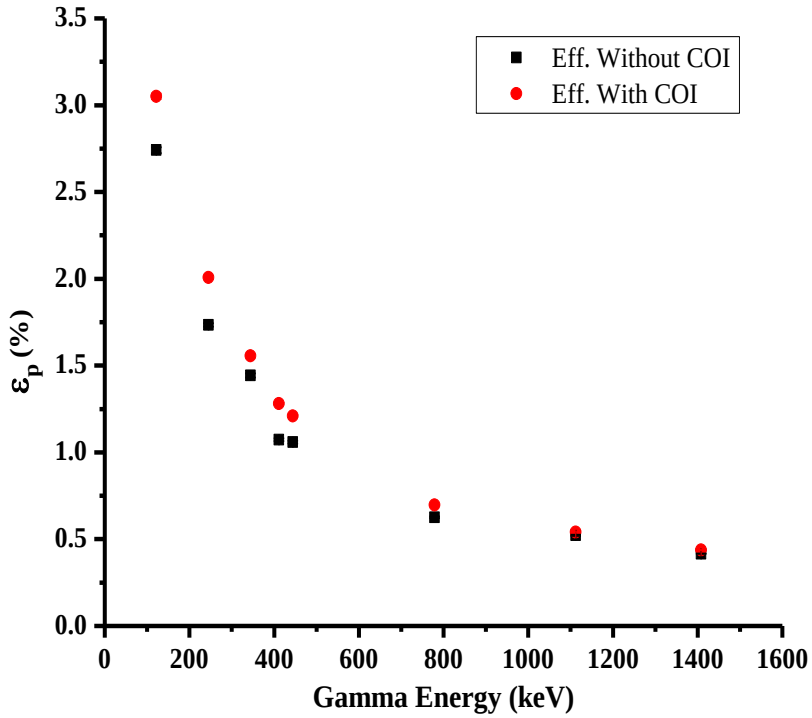


**Figure 20:** Experimental detection efficiency of the HPGe detector $\varepsilon_p$ for the $^{152}$Eu standard point sources placed at distance of 1 cm from the detector with and without true coincidence summing corrections (COI). The error bar for the uncertainty due to counting statistics is within the symbol.

Since the calibration of the HPGe detector was carried out with the point source while the activated foil stack has a finite area (1cm × 1cm), the efficiency for the point source geometry $\varepsilon_p$ was transferred by Monte Carlo Code EFFTRAN (Vidmar, 2005) to the efficiency for the foil stack geometry ε, which is shown in **Figures 21** and **Table 6**.

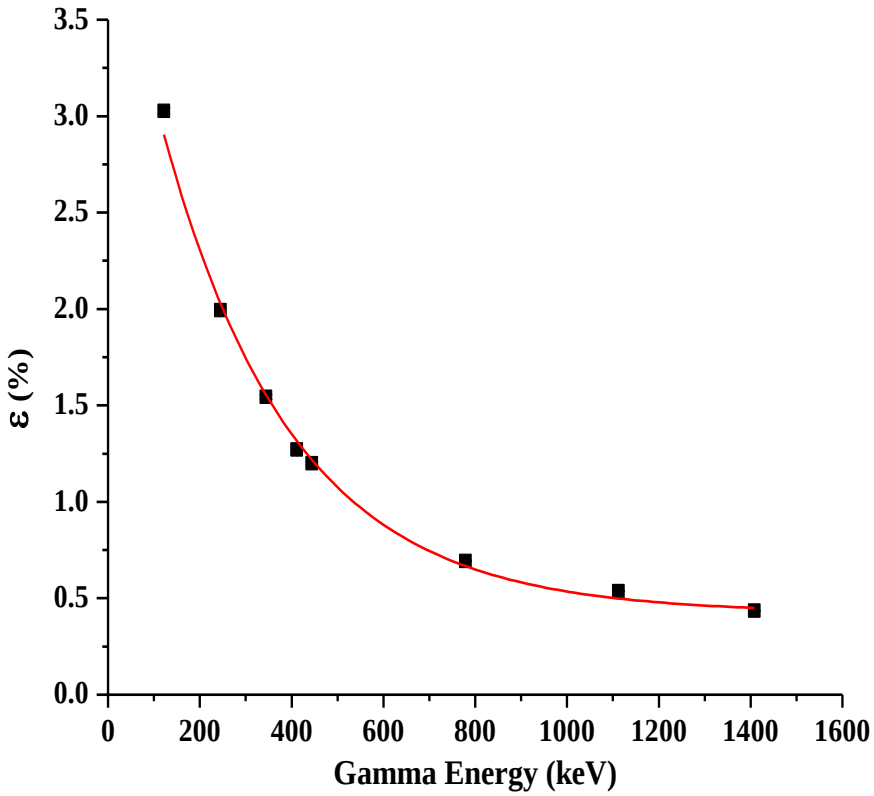


**Figure 21:** Detection efficiency calibration curve of the HPGe detector for the 1 cm ×1 cm source placed at a distance of 1 cm from the detector. The error bar for the uncertainty due to counting statistics is within the symbol.

### 2.6. Interpolation of Detection Efficiency

In order to obtain the detector efficiencies at the characteristic γ energies of the $^{71}Zn^{m}$ ($E_{Zn}$ = 386.28 keV) and $^{198}Au$ ($E_{Au}$ = 411.802 keV), the point-wise

efficiencies in **Table 6** were interpolated through the following fitting function (see **Figure 21**):

$$\varepsilon(E) = \varepsilon_0 \exp(-E/E_0) + \varepsilon_c \quad - - - (30)$$

The fitting parameter values are given in **Table 7**. This **Eq. (30)** gives the detection efficiencies of 386.28 keV γ-ray of $^{71}Zn^{m}$ and 411.802 keV γ-ray of $^{198}Au$ as $\varepsilon_{Zn}$ = 1.404644 ± 0.034969% and $\varepsilon_{Au}$ = 1.319418 ± 0.034688%, respectively.

**Table 7:** The efficiency curve fitting parameter values.

| **Parameter** | **Value** | **Uncertainty** | **Correlation coefficient** | | |
|---|---|---|---|---|---|
| **$\varepsilon_0$** | 3.889 | 0.2083 | 1.000 | | |
| **$E_0$(keV)** | 279.541 | 16.880 | -0.843 | 1.000 | |
| **$\varepsilon_c$** | 0.428 | 0.0194 | 0.408 | -0.687 | 1.000 |

# CHAPTER 3

# DATA ANALYSIS PROCEDURE

# 3. DATA ANALYSIS PROCEDURE

## 3.1. Estimation of the Cross section

The measured $^{70}$Zn($n$, $\gamma$)$^{71}$Zn$^{m}$ cross section $\langle\sigma_{Zn}^{m}\rangle_{exp}$ was derived with the $^{197}$Au($n$, $\gamma$)$^{198}$Au reference cross section $<\sigma_{Au}>$ by

$$\langle\sigma_{Zn}^{m}\rangle_{exp} = \langle\sigma_{Au}\rangle(A_{Zn}/A_{Au})[a_{Au}N_{Au}I_{Au}\varepsilon_{Au}f_{Au}/(a_{Zn}N_{Zn}I_{Zn}\varepsilon_{Zn}f_{Zn})](C_{Zn}/C_{Au}) \quad ---(31),$$

where, $A_x = \Sigma_i A_{x,i}$ is the number of counts ($A_{x,i}$ is the number of counts from i-th counting), $a_x$ is the isotopic abundance of the sample, $N_x$ is the number of atoms, $I_x$ is the $\gamma$ intensity, $\varepsilon_x$ is the detection efficiency,

$$f_x = [1 - \exp(-\lambda_x t_1)]\sum_i \exp(-\lambda_x t_{2,i})\left[1 - \exp(-\lambda_x t_{3,i})\right]/\lambda_x \quad ---(32)$$

is the timing factor for the irradiation time $t_1$, cooling time for the i-th counting $t_{2,i}$, measuring the time for the i-th counting $t_{3,i}$, $\lambda_x$ is the decay constant, and $C_x$ is the correction factor (x = Zn or Au). See **Tables 2** and **3** for timing parameters and decay data, respectively. The symbol <...> signifies that the cross section is averaged for the ($p$, $n_0$) neutron flux energy spectrum $\varphi_0$(E). The fractional uncertainty in the cross section was estimated by the quadrature sum of the fractional uncertainty in $<\sigma_{Au}>$, $A_x$, $a_x$, $N_x$, $I_x$, $f_x$, $C_x$ (x = Zn and Au) as well as $\varepsilon_{Au}/\varepsilon_{Zn}$. The fractional uncertainty in $\Delta f_x/f_x$ was determined assuming that the uncertainty is due to the uncertainty in the half-lives of $^{71m}$Zn and $^{198}$Au. See **Section 3.4.1** for the determination of $\Delta f_x/f_x$.

## 3.2. Reference Cross section

The reference cross section $<\sigma_{Au}>$ was obtained by folding the IAEA Neutron Cross Section Standards $\sigma_{Au}$(E) (Carlson *et al*., 2009) with the neutron flux energy spectrum $\varphi_0$(E) obtained by EPEN:

$$<\sigma_{Au}> = \int \varphi_0(E)\sigma_{Au}(E)dE / \int \varphi_0(E)dE \quad ---(33)$$

The energy integrated neutron flux determined from the $^{198}$Au activity after subtracting the contributions of ($p$, $n_1$) neutrons is ~ 1.2 × $10^6$ n/cm$^2$/s at 0.96MeV and ~ 1.4 × $10^6$ n/cm$^2$/s at 1.69 MeV. These fluxes agree well with those determined by the measured $^{115}$In$^m$ counts and the evaluated $^{115}$In($n$, $n'$)$^{115}$In$^m$ cross section in the IRDF-2002 library (Bersillon *et al*., 2006) within 5%.

### 3.3. Corrections

The correction factor $C_x$ in **Eq. (31)** is decomposed to

$$C_x = C_{x,fluc} \bullet C_{x,low} \bullet C_{x,scat} \bullet C_{x,attn} \quad --- \quad (34)$$

(x = Zn or Au). Each term is the correction factor for

1. neutron flux fluctuation (fluc)
2. low energy neutron backgrounds due to $^7$Li($p$, $n_1$)$^7$Be neutrons (low)
3. scattered neutron background originating from elastic, inelastic and multiple scattering in the foil stack and the surrounding materials (scat)
4. γ-rays self-attenuation (attn).

and summarized in **Table 8.** Some correction factors were determined for the two gold foils separately and their means were applied to **Eq. (31)** because we did not count γ-rays from two gold foils separately.

**Table 8:** Correction factors applied to the measured cross section derivation by **Eq. (31).**

| **$E_n$ (MeV)** | 0.96 | 1.69 |
|---|---|---|
| **$C_{Zn,fluc}$/ $C_{Au,fluc}$** | 0.869 | 0.748 |
| **$C_{Au,low}$** | 0.920 (front)<br>0.921 (back)<br>0.921 (mean) | 0.884 (front)<br>0.884 (back)<br>0.884 (mean) |
| **$C_{Zn,low}$** | 0.948 | 0.888 |
| **$C_{Zn,scat}$** | 0.985 | 0.975 |
| **$C_{Au,scat}$** | 0.985 (front)<br>0.983 (back)<br>0.984 (mean) | 0.981 (front)<br>0.979 (back)<br>0.980 (mean) |

| | | |
|---|---|---|
| $C_{Zn,attn.}$ | 1.015 | 1.016 |
| $C_{Au,attn.}$ | 1.019 (front)<br>1.010 (back)<br>1.01 (mean) | 1.020 (front)<br>1.010 (back)<br>1.015 (mean) |

### 3.3.1. Neutron Flux Fluctuation Correction Factor

From the activity formula **Eq. (7)**, we can see that the activity of the irradiated foil is proportional to the neutron flux. Hence, the activation formula assumes a constant neutron flux during the time of irradiation. The effect of the variation of neutron flux as a function of time due to proton current fluctuation during the long irradiation time was taken into consideration. Its correction factor for flux fluctuation was obtained by (Sage *et al*, 2010; Fessler *et al*., 2000):

$$C_{x,fluc} = <\Phi_m> [1 - \exp(-\lambda_x t_1)] / \left[\sum_{i=1,n} \Phi_{m,i} [1 - \exp(-\lambda_x \Delta t_1)] \exp[-\lambda_x (t_1 - i\Delta t_1)]\right] - - - (35)$$

where $\Phi_{m,i}$ is the neutron flux measured by the NE213 monitor detector during the i-th time interval ( $i$ = 1,$n$ *i.e.*, time bin and $n$ is number of total time bins), $\Delta t_1 = t_1/n$ is the dwell time (*i.e.*, 30 min) and $<\Phi_m> = \Sigma_{i=1,n} \Phi_{m,i} / n$ is the mean flux during irradiation. This correction factor applied to the ratio of measured Zinc to Gold samples for each irradiation is significant, because, the half-lives of the captured products $^{71}Zn^m$ (3.96 ± 0.05h) and $^{198}Au$ (2.6947 ± 0.0003d ) which are formed simultaneously, are very different.

### 3.3.2. Low Energy Background Neutron Correction Factor

The correction of neutron background contributions for low-energy neutrons ($p, n_1$) *i.e.,* second group of neutrons produced due to the population of the first excited state of $^7Be$, were also applied using neutron energy spectra obtained from the EPEN. If the proton energy is above a cut-off energy, $E_p^c = 2.37$ MeV, a second neutron

production channel $^{7}$Li($p$, $n_1$)$^{7}$Be opens in addition to $^{7}$Li($p$, $n_0$)$^{7}$Be, which leads to a second neutron group at lower energies. Hence, the cut-off energy $E_p^c$ was defined, above which the neutrons were found to be quasi-monoenergetic. The neutron group due to the $^{7}$Li($p$, $n_2$)$^{7}$Be reaction does not appear until $E_p$ = 7.07 MeV, but the $^{7}$Li($p$, $n+^{3}He+\alpha$) three-body breakup channel also opens at proton energies above $E_p$ = 3.70 MeV and shows a broad neutron spectrum. The position of this cut-off varied depending on the incident deuteron energy. The incident neutron spectrum obtained from EPEN clearly indicates the separation with a deep valley and then, the second group neutron spectra for 2.8MeV and 3.5 MeV proton energies can be clearly seen and their integrated neutron flux/intensity can be estimated from the **Figures 11** & **12**. The required correction factor was then calculated by forming the ratio of the sample activities produced by neutrons below the cut-off energy to those produced by the entire neutron spectrum. Then, the ($p$, $n_1$) low energy neutron background was subtracted by the correction factor

$$C_{x,low} = 1 - \int \varphi_1(E)\sigma_x(E)dE \Big/ \int \varphi(E)\sigma_x(E)dE \quad ---(36)$$

where $\varphi_1$(E) is the ($p$, $n_1$) neutron flux energy spectrum calculated by EPEN ($\varphi$(E) = $\varphi_0$(E) + $\varphi_1$(E)), and $\sigma_x$(E) is the $^{70}$Zn($n$, $\gamma$)$^{71}$Zn$^{m}$ cross section taken from the TENDL-2015 library (Koning *et al*., 2015) or $^{197}$Au($n$, $\gamma$)$^{198}$Au cross section taken from the IAEA Neutron Cross Sections Standards (Carlson *et al*., 2009).

### 3.3.3. Scattered Neutron Background Correction Factor

Correction factors for the scattered neutron background $C_{scat}$ originating from elastic, inelastic and multiple scattering in the foil stack and surrounding materials were evaluated by PHITS (Particle and Heavy Ion Transport code System) Ver 2.840 (Sato *et al*., 2013). The experimental setup with all materials in and around the foil

stack placed downstream of the tantalum proton beam stopper in **Figures 9(a-c)** was modelled in the simulation. Neutrons were generated according to the ($p$, $n_0$) neutron flux energy spectra $\varphi_0(E)$ calculated by EPEN and in the forward direction. Productions of $^{71}Zn^m$ and $^{198}Au$ were calculated with the ($p$, $n_0$) neutron spectra from EPEN and evaluated cross sections of all foil stack and surrounding materials from the AceLibJ40 library (a library in the ACE Format based on JENDL-4.0). Cross sections were calculated by counting $^{71}Zn^m$ and $^{198}Au$ produced by all neutrons including neutrons scattered by a foil stack or surrounding material before the production (All), and those produced by neutrons not scattered before the production (True). The calculated cross sections and correction factors are summarized in **Table 9**. The uncertainties in $C_{scat}$ are about 0.5% and 0.1% for Zn and Au foils, respectively. The weighted means of $C_{scat}$ are adopted in determination of experimental cross sections because we cannot distinguish γ-rays from front and back foils in our measurement.

**Table 9:** Cross sections (mb) and correction factors calculated by PHITS with neutron flux energy spectra from EPEN and evaluated cross sections of all foil stack and surrounding materials in JENDL-4.0. The uncertainties in cross sections are standard deviations due to statistics from 500 M (Zn) and 100 M neutrons (Au).

| $E_n$ (MeV) | Foil | All | True | $C_{scat}$ | (mean) |
|---|---|---|---|---|---|
| 0.96 | Au front | 82.600 ± 0.076 | 81.350 ± 0.068 | 0.985 ± 0.001 | 0.984 ± 0.001 |
| | Au back | 82.330 ± 0.073 | 80.940 ± 0.068 | 0.983 ± 0.001 | |
| | Zn | 1.378 ± 0.004 | 1.358 ± 0.004 | 0.985 ± 0.004 | |
| 1.69 | Au front | 70.440 ± 0.073 | 69.120 ± 0.067 | 0.981 ± 0.001 | 0.980 ± 0.001 |
| | Au back | 66.750 ± 0.070 | 65.320 ± 0.063 | 0.979 ± 0.001 | |
| | Zn | 0.627 ± 0.003 | 0.611 ± 0.002 | 0.975 ± 0.005 | |

### 3.3.4. γ-ray Self-attenuation Factors

When a gamma ray passes through any material, including the sample in which it is generated, with a given probability, it undergoes specific interactions. In these interactions, the photon is attenuated either by absorption or scattering with losing energy partially or totally; in any case, it cannot contribute to the peak count-rate. This effect of gamma photon attenuation within the sample itself before being measured with a detector apparatus is called self-attenuation. The degree of self-attenuation depends on a number of factors such as samples geometry (shape and sample – detector geometry) and linear attenuation coefficient $\mu$; the linear attenuation coefficient depends in turn on material density, sample composition, and photon energy $E$ (Robu *et al*., 2008). The gamma photon attenuation in the sample can also induce serious systematic errors if a stack of foils is used since the gamma photon while passing through the second foil is reduced by absorption in the first foil and so on. It is usually a function of the total linear attenuation coefficient $\mu_l$ multiplied by the thickness of the sample as measured in the direction of the gamma photon. For the purposes of accuracy and precision that are needed in the analysis involving the NAA technique, gamma spectrometric analysis requires correction for the self-attenuation effect due to the interactions of the γ-rays with the foil stack. According to Beer-Lambert's Law, the probability to find a photon penetrating a distance $x_1$ with a fluence, $I_0$, in a material-1(volume mass density $\rho_1$) as shown in **Figure 22** is given by

$$I_1/I_0 = \exp(-\mu_{l,1}x_1) = \exp(-\mu_{\mathrm{m},1}\rho_1 x_1) - - - (37)$$

where, $\mu_m$ is the mass attenuation coefficient of the $\gamma$ energy and material-1, and $I_1$ is gamma-ray flux at interface-1. If the 1st foil (thickness $x_1$) is a homogeneous source of the $\gamma$-line, and it penetrates other n-1 foils (thickness $x_i$) before reaching the detector,

the probability of the penetration is expressed by (Millsap *et al*., 2015; Robu *et al*., 2009; Jackman, 2007).

$$C_{S,attn} = \left[(1/x_1)\int_0^{x_1} \exp(-\mu_{m,1}\rho_1 x_1)\,dx\right] \bullet \prod_{i=2,n} \exp(-\mu_{m,i}\rho_i x_i)$$

$$= \left[\left[1-\exp(-\mu_{m,1}\rho_1 x_1)\right]/(\mu_{m,1}\rho_1 x_1)\right] \bullet \prod_{i=2,n} \exp(-\mu_{m,i}\rho_i x_i) - - - (38).$$

If the measured sample is subject to attenuation and the calibration source is not, the correction factor $C_{attn}$ must be applied to the peak area that is : $1/C_{S,attn}$, then,

$$C_{attn} = C_{S,attn}^{-1} = \left[(\mu_{m,1}\rho_1 x_1)/\left[1-\exp(-\mu_{m,1}\rho_1 x_1)\right]\right] \bullet \prod_{i=2,n} \exp(-\mu_{m,i}\rho_i x_i) - - - (39)$$

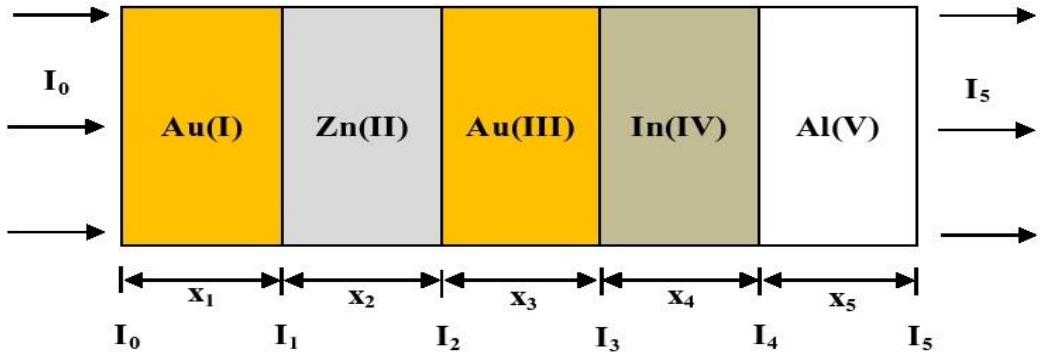


**Figure 22:** Gamma-rays Attenuation with a Fluence, $I_0$, Passing Through Five Different Samples.

**Table 10** shows the calculated self-attenuation factors of $^{71}Zn^{m}$ 386.28 keV and $^{198}Au$ 411.802 keV γ-rays penetrating the foil stack and detected by the detector behind the aluminium foil with the mass attenuation coefficients calculated by XMuDat Ver 1.01 (Nowotny, 1998).

**Table 10 :** Self-attenuations factor at each medium of the foil stack calculated by XMuDat Ver 1.01 (Nowotny, 1998).

| $E_n$ (MeV) | Sample | $^{198}Au$ $E_\gamma$ = 411.802 keV | $^{71}Zn^m$ $E_\gamma$ = 386.28 keV |
|---|---|---|---|
| 0.96 | Au (front) | 0.9851 | |
| | Zn | 0.9969 | 0.9916 |
| | Au (back) | 0.9859 | 0.9840 |
| | In | 0.9957 | 0.9957 |
| | Al | 0.9994 | 0.9994 |
| 1.69 | Au (front) | 0.9847 | |
| | Zn | 0.9961 | 0.9915 |
| | Au (back) | 0.9855 | 0.9836 |
| | In | 0.9945 | 0.9945 |
| | Al | 0.9994 | 0.9994 |

### 3.4. Error Propagation

The accurate value of neutron capture cross sections is important for reactor applications, critical safety, neutron dosimetry and nuclear astrophysics. However, the accuracy of the experimental cross section result is limited by the uncertainty. In order to get the accurate value, the covariance information is required. The uncertainty accompanied with the activation cross section is essential in determination of reasonable margin contributing to both safety and economy in nuclear applications. If several data points of the activation cross sections are involved in the determination of the quantity of interest (*e.g.*, reaction rate obtained by folding of energy dependent activation cross sections by the spectrum characterizing the incident particle field), the correlation (covariance) among the data points has to also be considered to avoid overestimation or underestimation of the uncertainty in the quantity of interest. Due to this situation, modern evaluation tries to provide not only the best estimate of the cross section but also their uncertainty and covariance describing correlation among data points of the same reaction or even different reactions ("cross-correlation"). In order

to provide the uncertainty and covariance in addition to the best estimate of the cross section based on the experimental knowledge, data evaluators need detailed documentation of the uncertainties in each experiment. However, evaluators often face difficulty due to lack of sufficient documentation of the experiment. At the worst case, the evaluators cannot find any uncertainty in the measured cross section, and it is also not rare to see a total uncertainty without its breakdown (*e.g.*, uncertainty due to counting statistics). The covariance measures the strength of the correlation between the variables. This information describes how the covariances of neutron capture cross section in reference standard cross section and efficiency of the HPGe detector, and the uncertainty in the timing factor were estimated.

### 3.4.1. Determination of the Uncertainty in the Timing Factor, Δfx/fx

Since, the γ-lines of the reaction product $^{71m}$Zn and monitor product $^{198}$Au were measured simultaneously, we can set $t_{2,x} = t_{2,m} = t_2$ and $t_{3,x} = t_{3,m} = t_3$ (x = Zn and m = Au) in **Eq. (32).** Then these time factors contain five sources of uncertainties $t_1$, $t_2$, $t_3$, $\lambda_x$ and $\lambda_m$. In this experimental work, the uncertainties in $t_1$, $t_2$ and $t_3$ are considered as negligible, therefore only the uncertainties in $\lambda_x$ and $\lambda_r$ have to be propagated. Some researchers include the uncertainty in the decay constants in the quadrature sum formula $(\Delta\sigma_x + \sigma_x)^2 = (\Delta\lambda_x + \lambda_x)^2 + (\Delta\lambda_r + \lambda_r)^2 + \ldots$, but it is not correct, because, the decay constant is related to the cross section through the exponential function. The correct way is to calculate the uncertainties in the time factors $f_x$ and $f_r$, and propagate them to the uncertainty in $\sigma_x$ by $(\Delta\sigma + \sigma)^2 = \ldots. + (\Delta f_x + f_x)^2 + (\Delta f_r + f_r)^2 + \ldots$ The uncertainties in the time factors should be propagated from the uncertainties in the decay constants.

For the timing factor in **Eq. (32)**

$$f_{\mathrm{x}} = [1 - \exp(-\lambda_{\mathrm{x}} t_1)] \sum_i \exp\left(-\lambda_{\mathrm{x}} t_{2,\mathrm{i}}\right) [1 - \exp\left(-\lambda_{\mathrm{x}}, t_{3,\mathrm{i}}\right)]/\lambda_{\mathrm{x}} = \sum_i f_{\mathrm{x,i}}$$

$$---(40),$$

the uncertainty in the timing factor is:

$$\Delta f_{\mathrm{x,i}} = (\partial f_{\mathrm{x,i}}/\,\partial\lambda_{\mathrm{x}})\Delta\lambda_{\mathrm{x}} = (\partial f_{\mathrm{x,i}}/\,\partial\lambda_{\mathrm{x}})(\mathrm{d}\lambda_{\mathrm{x}}/\mathrm{dT}_{1/2,\mathrm{x}})\Delta\mathrm{T}_{1/2,\mathrm{x}}$$

$$= (\lambda_{\mathrm{x}}/\mathrm{T}_{1/2,\mathrm{x}})(\partial f_{\mathrm{x,i}}/\,\partial\lambda_{\mathrm{x}})\Delta\mathrm{T}_{1/2,\mathrm{x}} --- (41)$$

assuming that only the uncertainty in the half-life is responsible to the uncertainty in the timing factor. The uncertainty in the decay constant $\Delta\lambda = (\ln 2\Delta T_{1/2}) = T^2_{1/2}$ can be obtained from $\Delta T_{1/2}$ in the ENSDF library. The partial derivative $\partial f_{\mathrm{x,i}}/\partial\lambda_{\mathrm{x}}$ can be calculated by:

$$\partial f_{\mathrm{x,i}}/\,\partial\lambda_{\mathrm{x}} = f_{\mathrm{x,i}} t_{1,\mathrm{i}} \exp(-\lambda_{\mathrm{x}} t_1)\,/[1 - \exp(-\lambda_{\mathrm{x}} t_1)]$$

$$-f_{\mathrm{x,i}} t_{2,\mathrm{i}}$$

$$+f_{\mathrm{x,i}} t_{3,\mathrm{i}} \exp\left(-\lambda_{\mathrm{x}} t_{3,\mathrm{i}}\right)/[1 - \exp\left(-\lambda_{\mathrm{x}}, t_{3,\mathrm{i}}\right)]$$

$$-f_{\mathrm{x,i}}/\lambda_{\mathrm{x}} --- (42)$$

This equation shows that the sensitivity depends not only on $\lambda$ but also on $t_1$, $t_2$, and $t_3$ even though the uncertainties in the latter three parameters are treated as negligible. Finally we obtain the fractional uncertainty in $f_{\mathrm{x}}$ by:

$$\Delta f_{\mathrm{x}}/f_{\mathrm{x}} = \left[\sum_i (\Delta f_{\mathrm{x,i}})^2\right]^{\frac{1}{2}} f_{\mathrm{x}} \; --- (43),$$

which is listed in **Table 19** as the uncertainty in the cross section due to the uncertainty in the half-life. Taking the first, second, third and fourth parts of the right-hand side of **Eq. (32)** as **Eq.(i)**, **(ii)**, **(iii)** and **(iv)**, and the parameters given in **Table 11**, the timing factors for $^{71}Zn^{m}$ and $^{198}Au$ at proton energies of 2.8 MeV and 3.5 MeV are calculated as shown in the **Tables 12(a)** & **(b)** and **13(a)** & **(b).**

**Table 11:** Decay data adopted for calculation of timing factor taken from the ENSDF library.

| **Nuclide** | **T1/2 (sec)** | **ΔT1/2 (sec)** | **λ (1/sec)** | **Δλ (1/sec)** |
|---|---|---|---|---|
| $^{71}Zn^{m}$ | 14256 | 180 | 4.86214E-05 | 6.13907E-07 |
| $^{198}Au$ | 232822.08 | 25.92 | 2.97715E-06 | 3.31446E-10 |

**Table 12(a):** Calculation of timing factor for $^{71}Zn^{m}$ at $E_p$ = 2.8 MeV.

| **For $E_p$ = 2.8 MeV** | | | | | | | | | | |
|---|---|---|---|---|---|---|---|---|---|---|
| **$^{71}Zn^{m}$** | | | | | | | | | | |
| **$t_1$ (sec)** | **$t_{2i}$ (sec)** | **$t_{3i}$ (sec)** | **$f_i$ (sec)** | **Eq.(i) (sec$^2$)** | **Eq.(ii) (sec$^2$)** | **Eq.(iii) (sec$^2$)** | **Eq.(iv) (sec$^2$)** | **$\partial f_i/\partial\lambda$ (sec$^2$)** | **Δf (sec)** | **Δf/f (%)** |
| 26580 | 1808 | 3875.6 | 2346.6536 | 23614353.1 | -4242749.6 | 43859150.9 | -48263765.7 | 14966988.6 | 16.5875 | 0.177 |
| 26580 | 5705.6 | 3636.9 | 1832.2432 | 18437846.3 | -10454046.7 | 34450158.4 | -37683856.4 | 4750101.5 | | |
| 26580 | 9373.5 | 7313.7 | 2830.3354 | 28481638.9 | -26530148.8 | 48473699.4 | -58211679.2 | -7786489.7 | | |
| 26580 | 16746.2 | 7212.3 | 1954.7902 | 19671035.9 | -32735307.9 | 33566177.2 | -40204288.7 | -19702383.5 | | |
| 26580 | 24012.5 | 1836 | 396.41308 | 3989101.1 | -9518869.0 | 7794558.06 | -8153051.7 | -5888261.5 | | |

**Table 12(b):** Calculation of timing factor for $^{178}Au$ at $E_p$ = 2.8 MeV.

| **For $E_p$ = 2.8 MeV** | | | | | | | | | | |
|---|---|---|---|---|---|---|---|---|---|---|
| **$^{198}Au$** | | | | | | | | | | |
| **$t_1$ (sec)** | **$t_{2i}$ (sec)** | **$t_{3i}$ (sec)** | **$f_i$ (sec)** | **Eq.(i) (sec$^2$)** | **Eq.(ii) (sec$^2$)** | **Eq.(iii) (sec$^2$)** | **Eq.(iv) (sec$^2$)** | **$\partial f_i/\partial\lambda$ (sec$^2$)** | **$\Delta f$ (sec)** | **$\Delta f/f$ (%)** |
| 26580 | 1808 | 3875.6 | 291.5978 | 757444671.4 | -4242749.6 | 783681820.4 | -788220420.9 | 748663321.2 | 0.4718 | 0.027 |
| 26580 | 5705.6 | 3636.9 | 270.5773 | 591405080.7 | -10454046.7 | 612108642.3 | -615434472.3 | 577625204.0 | | |
| 26580 | 9373.5 | 7313.7 | 535.284 | 913565809.8 | -26530148.8 | 940372368.7 | -950684920.4 | 876723109.4 | | |
| 26580 | 16746.2 | 7212.3 | 516.4799 | 630960385.4 | -32735307.9 | 649572909.5 | -656596949.3 | 591201037.6 | | |
| 26580 | 24012.5 | 1836 | 129.6956 | 127952833.5 | -9518869.0 | 132788112.0 | -133151687.6 | 118070388.8 | | |

**Table 13(a):** Calculation of timing factor for $^{71}Zn^m$ at $E_p$ = 3.5 MeV.

| **For $E_p$ = 3.5 MeV** | | | | | | | | | | |
|---|---|---|---|---|---|---|---|---|---|---|
| **$^{71}Zn^m$** | | | | | | | | | | |
| **$t_1$ (sec)** | **$t_{2i}$ (sec)** | **$t_{3i}$ (sec)** | **$f_i$ (sec)** | **Eq.(i) (sec$^2$)** | **Eq.(ii) (sec$^2$)** | **Eq.(iii) (sec$^2$)** | **Eq.(iv) (sec$^2$)** | **$\partial f_i/\partial\lambda$ (sec$^2$)** | **$\Delta f$ (sec)** | **$\Delta f/f$ (%)** |
| 30300 | 1534 | 3591.2 | 2357.4 | 21237845.0 | -3616256.74 | 44375026.8 | -48484857.3 | 13511757.7 | 34.7933 | 0.273 |
| 30300 | 5180 | 3634.3 | 1996.09 | 17982772.8 | -10340145.1 | 37533276.1 | -41053702.7 | 4122201.1 | | |
| 30300 | 8852 | 3616.9 | 1662.46 | 14977090.4 | -14715254.4 | 31273491.6 | -34191891.5 | -2656563.9 | | |
| 30300 | 12541 | 7253.3 | 2560.53 | 23067802.7 | -32112616.9 | 43921099.7 | -52662552.3 | -17786266.7 | | |
| 30300 | 20114 | 10368.6 | 2360.84 | 21268828.5 | -47485278.2 | 37340325.5 | -48555590.9 | -37431715.1 | | |
| 30300 | 30573 | 7950.3 | 1149.5 | 10355843.6 | -35144005 | 19366058.4 | -23641833.8 | -29063936.8 | | |
| 30300 | 38532 | 6353.3 | 647.088 | 5829611.9 | -24933321.3 | 11358781.3 | -13308690.2 | -21053618.4 | | |

**Table 13(b):** Calculation of timing factor for $^{178}$Au at $E_p$ = 3.5 MeV.

| **For $E_p$ = 3.5 MeV** | | | | | | | | | | |
|---|---|---|---|---|---|---|---|---|---|---|
| **$^{198}$Au** | | | | | | | | | | |
| **$t_1$ (sec)** | **$t_{2i}$ (sec)** | **$t_{3i}$ (sec)** | **$f_i$ (sec)** | **Eq.(i) (sec$^2$)** | **Eq.(ii) (sec$^2$)** | **Eq.(iii) (sec$^2$)** | **Eq.(iv) (sec$^2$)** | **$\partial f_i/\partial\lambda$ (sec$^2$)** | **$\Delta f$ (sec)** | **$\Delta f/f$ (%)** |
| 30300 | 1534 | 3591.2 | 306.718 | 756653404.4 | -3616256.7 | 787605770.7 | -791831181 | 748811737.0 | | |
| 30300 | 5180 | 3634.3 | 307.028 | 640683001.2 | -10340145.1 | 666848513.0 | -670469167 | 626722202.2 | | |
| 30300 | 8852 | 3616.9 | 302.245 | 533597757.3 | -14715254.4 | 555404316.1 | -558405394 | 515881424.8 | | |
| 30300 | 12541 | 7253.3 | 596.269 | 821850403.3 | -32112616.9 | 850806550.2 | -860059271 | 780485065.2 | 0.5196 | 0.0151 |
| 30300 | 20114 | 10368.6 | 829.528 | 757757271.7 | -47485278.2 | 780810021.0 | -792986369 | 698095645.8 | | |
| 30300 | 30573 | 7950.3 | 618.766 | 368953834.5 | -35144005.0 | 381555557.7 | -386106966 | 329258420.8 | | |
| 30300 | 38532 | 6353.3 | 484.04 | 207695068.8 | -24933321.3 | 215301985.3 | -217351076 | 180712656.7 | | |

### 3.4.2. Uncertainty in Detector Efficiency

In this experiment, a hyperpure HPGe detector separated by 1 cm from the irradiated foil stack was used to determine $C_{Zn}$ and $C_{Au}$ in **Eq. (31)**. The detection efficiencies of the detector were measured by using eight γ-lines of a $^{152}$Eu calibration source. The detection efficiency for the i-th γ-line (emission probability $I_i$, Martin, 2013) was determined by:

$$\varepsilon_{p,i} = \frac{C\boldsymbol{\varepsilon_{G,i}}K_{c,i}}{A_0 e^{-\lambda t}\Delta t_{c,i} I_{\gamma,i}} - - - (44).$$

We express the energy dependence of the detection efficiency by **Eq. (30)** in which the three parameters ($\varepsilon_0$, $E_0$ and $\varepsilon_c$) are determined by fitting this function to the measured detection efficiencies { $\varepsilon_i$ } with their uncertainties propagated from $\Delta C_i = \sqrt{C_i}$ and $\Delta I_i$ determined by the ENSDF evaluator (Martin, 2013). Note that, we do not have to propagate the uncertainties in the parameters commonly applied to all γ-lines (e.g., $\Delta A_0$, $\Delta\lambda$) because only the ratio of the detection efficiency ($\eta_{r,x} = \varepsilon_r / \varepsilon_x$) is required in our cross section measurement. The parameters reproducing the efficiency { $\varepsilon_i$ } in **Table 7** gives the detection efficiency curve $\varepsilon(E_\gamma)$ in **Figure 21**.

The counts C, gamma intensities $I_\gamma$, coincidence summing effect correction factors $K_c$, the detection efficiencies for the point source geometry $\varepsilon_p$ and for the foil stack geometry E at the characteristic γ energies of $^{152}$Eu and the uncertainties Δε propagated from the C, ΔC, $I_\gamma$, $\Delta I_\gamma$, $\varepsilon_p$, and ε are given in **Table 14**.

**Table 14:** The uncertainties Δε propagated from the C, ΔC, $I_\gamma$, $\Delta I_\gamma$, $\varepsilon_p$, and ε.

| $E_\gamma$ (keV) | C | ΔC | $I_\gamma$ | $\Delta I_\gamma$ | $\varepsilon_{p(uncor)}$ (%) | $K_c$ | $\varepsilon_{p(cor)}$ (%) | ε (%) | Δε (%) |
|---|---|---|---|---|---|---|---|---|---|
| 121.8 | 328049.3 | 572.7559 | 0.2853 | 0.0016 | 2.7416 | 1.113 | 3.0514 | 3.0270 | 0.0178 |
| 244.7 | 53997.8 | 232.3743 | 0.0755 | 0.0004 | 1.7343 | 1.158 | 2.0083 | 1.9940 | 0.0136 |
| 344.3 | 157183.5 | 396.4637 | 0.2659 | 0.002 | 1.4425 | 1.078 | 1.5550 | 1.5450 | 0.0123 |
| 411.1 | 9647.2 | 98.22016 | 0.02237 | 0.00013 | 1.0731 | 1.193 | 1.2803 | 1.2720 | 0.0149 |
| 444.0 | 13292.1 | 115.2914 | 0.03125 | 0.00018 | 1.0584 | 1.142 | 1.2087 | 1.2013 | 0.0125 |
| 778.9 | 32542.8 | 180.3962 | 0.1293 | 0.0008 | 0.6263 | 1.112 | 0.6964 | 0.6922 | 0.0058 |
| 1112.1 | 28712.2 | 169.4467 | 0.1367 | 0.0008 | 0.5227 | 1.033 | 0.5399 | 0.5368 | 0.0045 |
| 1408.0 | 34940.8 | 186.9246 | 0.2087 | 0.0009 | 0.4166 | 1.050 | 0.4374 | 0.4349 | 0.0030 |

The correlation coefficient of efficiency curve fitting parameters obtained from **Eq. (30)** is given in **Table 7**. On following the prescription by Mannhart (2013), we can propagate the covariances of the three fitting parameters of **Eq. (30)** to the two detection efficiencies at $E_{Zn}$ and $E_{Au}$ on the curve by:

$$cov(\varepsilon_{Zn}, \varepsilon_{Au}) = \exp[-(E_{Zn} + E_{Au})/E_0](\Delta\varepsilon_0)^2$$
$$+(\varepsilon_0^2 E_{Zn} E_{Au}/\mathrm{E}_0^4)\exp[-(E_{Zn} + E_{Au})/E_0](\Delta E_0)^2$$
$$+(\Delta\varepsilon_0)^2$$
$$+\varepsilon_0[(E_{Zn} + E_{Au})/\mathrm{E}_0^2]\exp[-(E_{Zn} + E_{Au})/E_0]cov(E_0, \varepsilon_c)$$
$$+[exp(-E_{Zn}/E_0) + \exp(-E_{Au}/E_0)]cov(\varepsilon_0, \varepsilon_c)$$
$$+[(\varepsilon_0 E_{Zn}/\mathrm{E}_0^2)\exp(-E_{Zn}/E_0) + (\varepsilon_0 E_{Au}/\mathrm{E}_0^2)\exp(-E_{Au}/E_0)]cov(\varepsilon_0, E_0)$$
$$---(45)$$

with $(\Delta\varepsilon_{Zn})^2$ = var $(\varepsilon_{Zn})$ and $(\Delta\varepsilon_{Au})^2$ = var $(\varepsilon_{Au})$. From the **Eq. (31),** we need only the detector efficiency ratio $\eta = \varepsilon_{Zn}/\varepsilon_{Au}$ , which fractional uncertainty $(\Delta\eta_{Zn,Au}/\ \eta_{Zn,Au})$ is further propagated following to **Eq. (46)** from var $(\varepsilon_{Zn})$, var $(\varepsilon_{Au})$ and cov$(\varepsilon_{Zn},\varepsilon_{Au})$ by

$$(\Delta\,\eta/\eta)^2 = (\Delta\varepsilon_{Zn}/\varepsilon_{Zn})^2 + (\Delta\varepsilon_{\mathrm{Au}}/\varepsilon_{Au})^2 - 2cov(\varepsilon_{Zn}, \varepsilon_{Au})/(\varepsilon_{Zn}, \varepsilon_{Au}) --- (46),$$

and we finally obtain $\eta = 1.06459 \pm 0.00274$.

Note that we do not have to propagate the uncertainties in the parameters commonly applied to all γ-lines (*e.g.*, $\Delta A_0$, $\Delta\lambda$) because only the ratio of the detection efficiency ($\eta_{m;x} = \varepsilon_m = \varepsilon_x$) is required in our cross section determination.

### 3.4.3. Uncertainty in the Standard Gold Cross section (Monitor)

The $^{197}$Au($n$, $\gamma$)$^{198}$Au cross section taken from the IAEA Neutron Cross Section Standards (A.D. Carlson, 2009) was adopted as the monitor cross section in this experiment. The **Figure 23(a)** shows the point-wise $^{197}$Au($n$, $\gamma$)$^{198}$Au monitor cross section $\sigma_r(E)$ and its group-wise cross section $\langle\sigma_r\rangle_k$ compiled in the IAEA Neutron

Cross Section Standards. Since the $^{7}$Li($p$, $n_0$)$^{7}$Be incident neutron beam is quasi-monoenergetic with having energy spread ($E_n$ = 0.96 ± 0.15 and 1.69 ± 0.15 MeV), the point wise monitor cross section in the IAEA Neutron Cross Section Standards $\sigma_r(E)$ was folded by the neutron flux energy spectrum $\Phi_i(E)$, ($\int_0^{\infty} \Phi_i(E)\mathrm{d}E = 1$, $i$ = 1, 2 are for $E_n$ = 0.96 or 1.05 MeV) calculated by a newly developed code EPEN (R. Pachuau, 2017(a) and 2017(b)):

$$\bar{\sigma}_{r,i} = \int \Phi_i(E)\sigma_r(E)\mathrm{d}E - - - (47).$$

The $^{7}$Li($p$, $n_0$)$^{7}$Be point-wise neutron flux energy spectrum $\phi_i$ (E) obtained from EPEN (Pachuau *et al*., 2017a, 2017b) and its group-wise expression $\Phi_{i,k}$ (i=1,2; k=1 to 11 and k=12 to 15 for i = 1 and 2, respectively) are shown in the **Figure 23(b)**. The covariance information of $\sigma_r(E)$ for its group-wise cross section in the IAEA Neutron Cross Section Standards can be expressed as:

$$\langle\sigma_r\rangle_k = \left(\int_{E_{k,min}}^{E_{k,max}} \sigma_r(E)\mathrm{d}E\right) / \left(E_{k,max} - E_{k,min}\right) - - - (48)$$

where, $E_{k,min}$ and $E_{k,max}$ are the lower and upper boundaries of the $k$-th energy group. Similarly, we also introduce the group-wise neutron flux energy spectrum $\Phi_{i,k}$ by:

$$\Phi_{i,k} = \int_{E_{k,min}}^{E_{k,max}} \Phi_i(E)\mathrm{d}E - - - (49)$$

which satisfies $\sum_k \Phi_{i,k} = 1$. These group-wise quantities are shown in **Figure 19** and **Table 8** & **9**, where k=1–11 and 12–15 are for the $E$ = 0.96 ± 0.15 $n$ and 1.69 ± 0.15 MeV neutrons, respectively. By using $\langle\sigma_r\rangle_k$ and $\Phi_{i,k}$, Eq. (47) is discretized to

$$\bar{\sigma}_{r,i} = \sum_k \Phi_{i,k}\,\langle\sigma_r\rangle_k - - - (50)$$

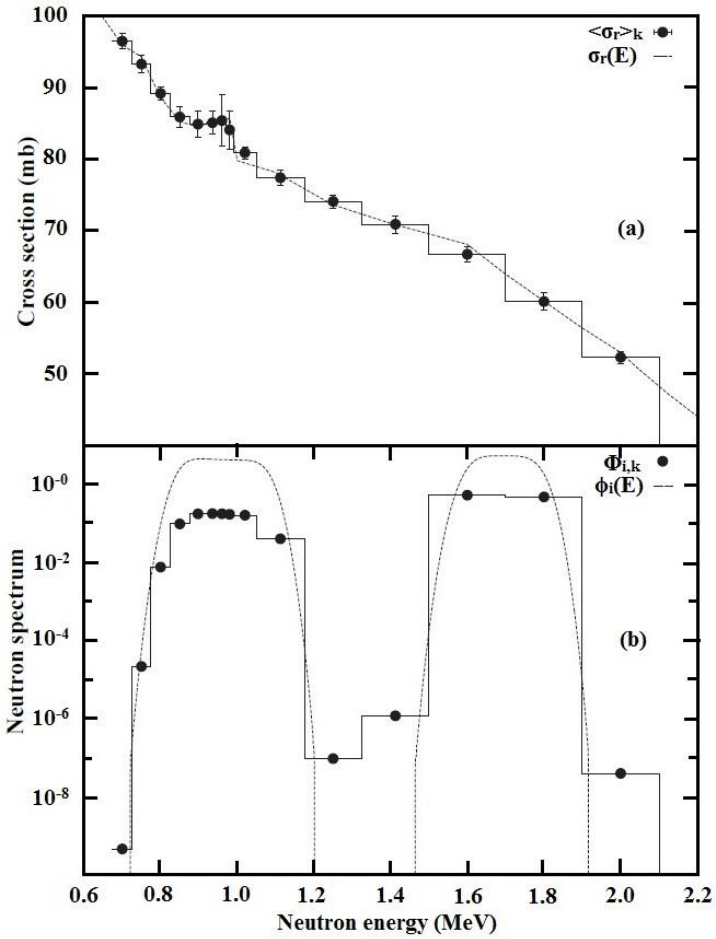


**Figure 23: (a)** The point-wise $^{197}Au(n,\gamma)^{198}Au$ monitor cross section $\sigma_r(E)$ in the IAEA Neutron Cross Section Standards (Carlson *et al.*, 2009) and its group-wise expression $<\sigma_r>_k$ . **(b)** The $^{7}Li(p, n_0)^{7}Be$ point-wise neutron flux energy spectrum $\phi_i(E)$ calculated by EPEN (Pachuau *et al.*, 2017a, 2017b) and its group-wise expression $\Phi_{i,k}$ (i=1,2; k=1 to 11 and k=12 to 15 for i = 1 and 2, respectively).

The uncertainty in $<\sigma_{Au}>$ due to the uncertainty in the IAEA Neutron Cross Section Standards was obtained by:

$$(\Delta< \sigma_{Au} >)^2 = \sum_i [\Phi_i^2 var(< \sigma_i >)] / \left(\sum_i \Phi_i\right)^2 + 2\sum_{i>j} [\Phi_i \Phi_j cov(< \sigma_i >, < \sigma_j >)] / \left(\sum_i \Phi_i\right)^2 \quad ---(51)$$

where *cov* (< $\sigma_i$ >,< $\sigma_j$ >) and *var* (< $\sigma_i$ >) are the covariances between the i-th and j-th group-wise cross section compiled in the IAEA Neutron Cross Section Standards and its diagonal component (i = j), and $\Phi_i = \int_i \varphi_0(E)\, dE$ is the neutron flux energy spectrum integrated over the i-th group of the IAEA Neutron Cross Section Standards. The summations for i and j are taken for all energy groups between 0.675 and 1.325 MeV for < $E_n$ > = 0.96 MeV neutrons (11 groups), and between 1.325 and 2.100 MeV for < $E_n$ > = 1.69 MeV neutrons (4 groups). In order to obtain the absolute covariance for the IAEA Neutron Cross Section Standards, the relative covariance ($\%^2$) compiled in the ENDF-6 format was converted to the corresponding absolute covariance ($b^2$) by multiplying the un-weighted group-wise cross section < $\sigma_i$ > constructed by ourselves. The **Figure 24** shows that the relative uncertainty plotted with uncertainty % against incident energy (MeV) taken from IAEA site (*https://www-nds.iaea.org/exfor/servlet/E4sMakeE4*). The spectrum-averaged cross sections are < $\sigma_{Au}$ > = 82.77 ± 0.86 mb at 0.96 MeV and 64.09 ± 0.92 mb at 1.69 MeV. The fractional group-wise flux $\Phi_i/\Sigma\Phi_i$ , obtained using EPEN neutron spectra, unweighted group-wise cross sections < $\sigma_i$ > of the IAEA neutron cross section standard, and their correlation coefficients

$$cor(\langle\sigma_i\rangle, \langle\sigma_j\rangle) = cov(\langle\sigma_i\rangle, \langle\sigma_j\rangle) / [var(\langle\sigma_i\rangle) var(\langle\sigma_j\rangle)]^{\frac{1}{2}} --- (52)$$

at 0.96 and 1.69 MeV are given in **Tables 15 and 16**, respectively.

Similarly, the covariance between two spectrum averaged cross sections at 0.96 and 1.69 MeV is obtained by:

$$Cov(\sigma_i, \sigma_j) = \sum_{i,j} [\Phi_i \Phi_j Cov(\langle\sigma_i\rangle, \langle\sigma_j\rangle)] / \left(\sum_i \Phi_i\right)\left(\sum_j \Phi_j\right) --- (53)$$

where, the summation for *i* is taken for all energy groups between 0.675 and 1.325 MeV for <$E_n$> = 0.96 MeV neutrons while the summation for *j* is taken for all

energy groups between 1.325 and 2.100 MeV for $< E_n > = 1.69$ MeV neutrons. By using the correlation coefficients $cor(<\sigma_i>,<\sigma_j>)$ given in Neutron Cross section Standard (Carlson, 2009), which is also given in **Table 17**, we obtain 0.059 $mb^2$ as the covariance of the spectrum averaged cross sections between two energies. These results are also summarized in **Table 18**.

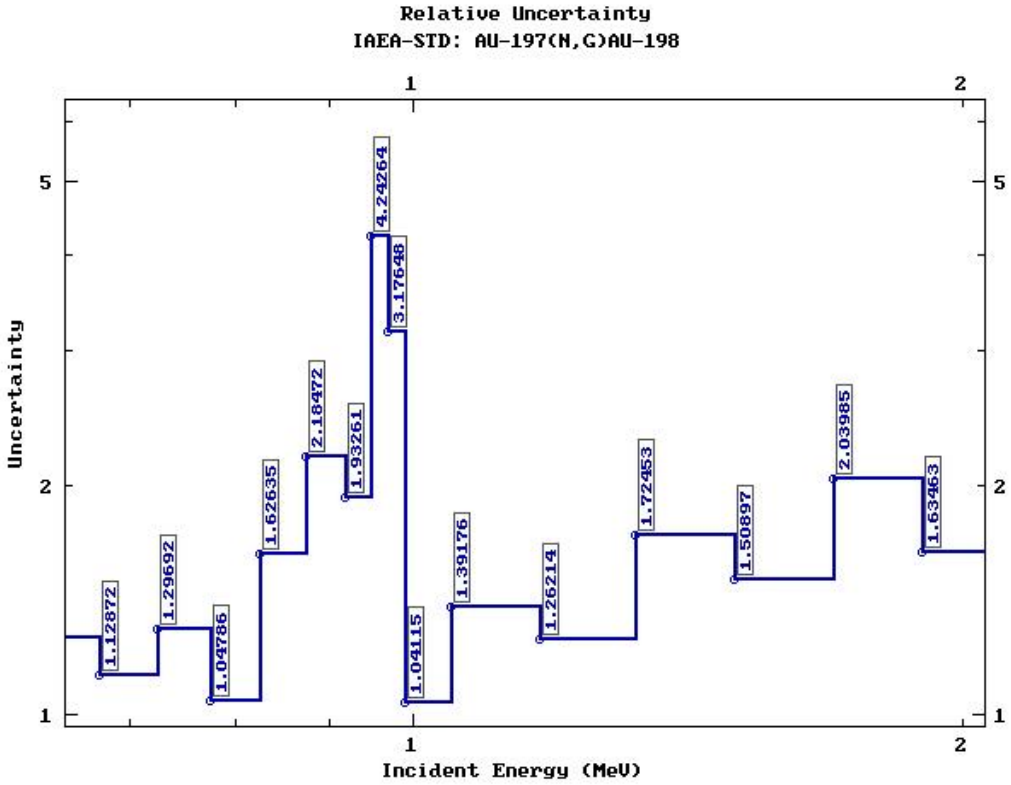


**Figure 24:** The relative uncertainty plotted with uncertainty % against incident energy (MeV) taken from IAEA site (*https://www-nds.iaea.org/exfor/servlet/ E4sMakeE4*).

**Table 15:** The fractional group-wise flux $\Phi_i/\Sigma\Phi_i$ of the $^7$Li($p$, $n_0$)$^7$Be spectrum, un-weighted group-wise cross section $<\sigma_i>$ and correlation coefficient cor($<\sigma_i>$,$<\sigma_j>$) in the IAEA Neutron Cross Section Standards for$<E_n>$ = 0.96 MeV neutrons.

| $E_{min}$ (MeV) | $E_{max}$ (MeV) | $\Phi_i/\Sigma\Phi_i$ | $<\sigma_i>$ (b) | $\Delta<\sigma_i>$ (%) | cor($<\sigma_i>$, $<\sigma_j>$) × 100 | | | | | | | | | | |
|---|---|---|---|---|---|---|---|---|---|---|---|---|---|---|---|
| 0.675 | 0.725 | 5.7302E-10 | 0.0964 | 1.1287 | 100.000 | | | | | | | | | | |
| 0.725 | 0.775 | 2.7463E-05 | 0.0932 | 1.2969 | 43.900 | 100.000 | | | | | | | | | |
| 0.775 | 0.825 | 9.6409E-03 | 0.0891 | 1.0479 | 34.120 | 51.770 | 100.000 | | | | | | | | |
| 0.825 | 0.875 | 1.2307E-01 | 0.0859 | 1.6264 | 20.010 | 28.920 | 33.310 | 100.000 | | | | | | | |
| 0.875 | 0.920 | 1.9745E-01 | 0.0849 | 2.1847 | 13.070 | 11.730 | 12.760 | 10.720 | 100.000 | | | | | | |
| 0.920 | 0.950 | 1.3143E-01 | 0.0851 | 1.9326 | 6.647 | 12.920 | 24.510 | 15.210 | 8.827 | 100.000 | | | | | |
| 0.950 | 0.970 | 8.5593E-02 | 0.0854 | 4.2426 | 2.581 | 4.046 | 5.590 | 9.520 | 3.219 | 6.007 | 100.000 | | | | |
| 0.970 | 0.990 | 8.4304E-02 | 0.0841 | 3.1765 | 7.715 | 6.316 | 7.412 | 6.074 | 43.520 | 4.910 | 1.937 | 100.000 | | | |
| 0.990 | 1.050 | 2.4379E-01 | 0.0808 | 1.0412 | 18.680 | 15.450 | 24.820 | 25.120 | 20.390 | 38.090 | 11.400 | 11.690 | 100.000 | | |
| 1.050 | 1.175 | 1.2469E-01 | 0.0773 | 1.3918 | 16.260 | 14.120 | 13.780 | 12.560 | 13.200 | 21.030 | 7.447 | 9.168 | 44.870 | 100.000 | |
| 1.175 | 1.325 | 2.8842E-07 | 0.0740 | 1.2621 | 17.280 | 16.130 | 18.170 | 12.910 | 11.790 | 6.297 | 3.395 | 12.260 | 27.560 | 40.740 | 100.000 |

**Table 16:** The fractional group-wise flux $\Phi_i/\Sigma\Phi_i$ of the $^7$Li($p$, $n_0$)$^7$Be spectrum, un-weighted group-wise cross section $<\sigma_i>$ and correlation coefficient cor($<\sigma_i>$,$<\sigma_j>$) in the IAEA Neutron Cross Section Standards for $<E_n>$ = 1.69 MeV neutrons.

| $E_{min}$ (MeV) | $E_{max}$ (MeV) | $\Phi_i/\Sigma\Phi_i$ | $<\sigma_i>$ (b) | $\Delta<\sigma_i>$ (%) | cor($<\sigma_i>$, $<\sigma_j>$) × 100 | | | |
|---|---|---|---|---|---|---|---|---|
| 1.325 | 1.500 | 1.0181E-06 | 0.0708 | 1.7245 | 100.000 | | | |
| 1.500 | 1.700 | 5.2954E-01 | 0.0666 | 1.5090 | 34.570 | 100.000 | | |
| 1.700 | 1.900 | 4.7046E-01 | 0.0600 | 2.0399 | 15.280 | 37.460 | 100.000 | |
| 1.900 | 2.100 | 3.0301E-08 | 0.0521 | 1.6346 | 12.010 | 25.040 | 38.210 | 100.000 |

**Table 17:** The correlation coefficient cor($<\sigma_i>$,$<\sigma_j>$) in the IAEA Neutron Cross Section Standards between $<E_n>$ = 0.96 and 1.69 MeV neutrons.

| | **$E_{min}$ (MeV)** | **$E_{max}$ (MeV)** | **cor($<\sigma_i>$, $<\sigma_j>$) × 100** | | | | | | | | | | |
|---|---|---|---|---|---|---|---|---|---|---|---|---|---|
| **$E_{min}$ (MeV)** | | | 0.675 | 0.725 | 0.775 | 0.825 | 0.875 | 0.920 | 0.950 | 0.970 | 0.990 | 1.050 | 1.175 |
| **$E_{max}$ (MeV)** | | | 0.725 | 0.775 | 0.825 | 0.875 | 0.920 | 0.950 | 0.970 | 0.990 | 1.050 | 1.175 | 1.325 |
| | 1.325 | 1.500 | 11.87 | 10.39 | 12.03 | 9.145 | 8.119 | 10.56 | 6.673 | 6.962 | 15.54 | 17.22 | 39.12 |
| | 1.500 | 1.700 | 14.01 | 12.28 | 14.40 | 11.14 | 10.95 | 10.76 | 4.417 | 8.172 | 18.60 | 14.93 | 22.76 |
| | 1.700 | 1.900 | 10.34 | 9.03 | 10.71 | 8.154 | 9.124 | 7.886 | 6.538 | 7.369 | 13.89 | 10.68 | 12.57 |
| | 1.900 | 2.100 | 12.09 | 10.5 | 12.47 | 9.483 | 10.09 | 9.439 | 4.228 | 7.915 | 16.07 | 12.78 | 14.88 |

**Table 18:** Reference cross section $<\sigma_{Au}>$ with their uncertainty and correlation coefficient.

| **$E_n$ (MeV)** | **Value (mb)** | **Uncertainty (mb)** | **Correlation coefficient** | |
|---|---|---|---|---|
| 0.96 | 82.77 | 0.86 | 1.00 | |
| 1.69 | 64.09 | 0.92 | 0.22 | 1.00 |

### 3.4.4. Total Uncertainty in the $^{70}Zn(n, \gamma)^{71}Zn^{m}$ Cross section

**Table 19** summarizes the uncertainties in various parameters to obtain the $^{70}Zn(n, \gamma)^{71m}Zn$ cross section. We use **Eq. (31)** for these parameters except for the replacement of $\varepsilon_x$ and $\varepsilon_m$ with $\eta$, and therefore, the total uncertainty is obtained by the quadratic sum rule.

**Table 19:** The fractional (%) partial uncertainty in the measured cross sections propagated from various sources of uncertainties. The last column gives the property of the correlation between two data points for each source of the uncertainty. See **Section 3.4.1** for the propagation of the uncertainties in the half-lives.

| | Source | $E_n$=0.96 MeV | $E_n$=1.69 MeV | Correlation property [a] |
|---|---|---|---|---|
| **Count** | Zn | 7.809 | 5.988 | Uncorrelated |
| | Au | 3.247 | 2.471 | |
| **Sample** | Zn enrichment | 1.381 | | Fully correlated |
| | Zn thickness | 0.115 | 0.088 | Uncorrelated |
| | Au thickness | 0.099 | 0.097 | |
| **Decay data** | Zn intensity | 2.298 | | Fully correlated |
| | Au intensity | 0.063 | | |
| | Zn half-life | 0.177 | 0.273 | |
| | Au half-life | 0.027 | 0.015 | |
| **Other** | Efficiency ratio | 0.257 | | Fully correlated |
| | Au standard | 1.043 | 1.433 | Partially correlated [b] |
| **Total** | | 8.94 | 7.17 | Partially correlated [c] |

[a] Uncorrelated, fully correlated and partially correlated mean the correlation coefficient is 0, 1 or between them, respectively. See Ref. (Smith *et al*., 2012; Otuka *et al*., 2017) for more details.

[b] Correlation coefficient is 0.22 (See Table 18).

[c] Correlation coefficient is 0.12, which is obtained by $(1.381^2 + 2.298^2 + 0.063^2 + 0.177 \cdot 0.273 + 0.027 \cdot 0.015 + 0.257^2 + 1.043 \cdot 1.433 \cdot 0.22) / (8.94 \cdot 7.17)$.

The 22 parameters in **Table 19** form the 13 subsets $C_{Zn,1}$, $C_{Zn,2}$, $C_{Au,1}$, $C_{Au;2}$, ($a_{Zn,1}$, $a_{Zn,2}$), ($n_{Zn;1}$, $n_{Zn;2}$), ($n_{Au,1}$, $n_{Au,2}$), ($I_{Zn,1}$, $I_{Zn,2}$), ($I_{Au,1}$, $I_{Au,2}$), ( $f_{Zn,1}$, $f_{Zn,2}$), ( $f_{Au,1}$, $f_{Au,2}$), ($\eta_1$, $\eta_2$), ($\sigma_{Au,1}$, $\sigma_{Au,2}$). From the uncertainties and correlation coefficients summarized in **Table 19**, we can construct the fractional variance and covariance by adding the matrices of 13 subsets:

$$\begin{pmatrix} 7.809^2 & 0 \\ 0 & 0 \end{pmatrix} + \begin{pmatrix} 0 & 0 \\ 0 & 5.988^2 \end{pmatrix} + \begin{pmatrix} 3.247^2 & 0 \\ 0 & 0 \end{pmatrix} + \begin{pmatrix} 0 & 0 \\ 0 & 2.471^2 \end{pmatrix}$$

$$+ \begin{pmatrix} 1.381^2 & 1.381^2 \\ 1.381^2 & 1.381^2 \end{pmatrix} + \begin{pmatrix} 0.115^2 & 0 \\ 0 & 0.088^2 \end{pmatrix} + \begin{pmatrix} 0.099^2 & 0 \\ 0 & 0.097^2 \end{pmatrix}$$

$$+ \begin{pmatrix} 2.298^2 & 2.298^2 \\ 2.298^2 & 2.298^2 \end{pmatrix} + \begin{pmatrix} 0.063^2 & 0.063^2 \\ 0.063^2 & 0.063^2 \end{pmatrix} + \begin{pmatrix} 0.177^2 & 0.177 \times 0.27 \\ 0.177 \times 0.27 & \text{o}.273^2 \end{pmatrix}$$

$$+ \begin{pmatrix} 0.027^2 & 0.027 \times 0.015 \\ 0.027 \times 0.015 & 0.015^2 \end{pmatrix} + \begin{pmatrix} 0.257^2 & 0.257^2 \\ 0.257^2 & 0.257^2 \end{pmatrix}$$

$$+ \begin{pmatrix} 1.043^2 & 1.043 \times 1.437 \times 0.07 \\ 1.043 \times 1.437 \times 0.07 & 1.437^2 \end{pmatrix} = \begin{pmatrix} 79.924 & 7.317 \\ 7.317 & 51.377 \end{pmatrix}$$

$$= \begin{pmatrix} 8.94^2 & 8.94 \times 7.17 \times 0.12 \\ 8.94 \times 7.17 \times 0.12 & 7.17^2 \end{pmatrix} - - - (54)$$

The last term shows that the total uncertainties in the cross sections are 8.94 and 7.17% at 0.96 and 1.69 MeV, respectively, and also the correlation coefficient between the two cross sections is 0.12.

# CHAPTER 4

# NUCLEAR MODELS

# 4. NUCLEAR MODELS

The excitation function of the $^{70}Zn(n, \gamma)^{71}Zn^{m}$ reaction from 0.4 MeV to 4 MeV was calculated using the nuclear reaction model code TALYS-1.6 (Koning *et al*., 2008a, 2012,2013) which was then compared with the measured cross sections. The optical model parameters for neutrons were obtained by a local potential proposed by Koning and Delaroche (Koning *et al*., 2003). The compound nucleus contribution was calculated by the Hauser-Feshbach model (Hauser *et al.,* 1952). There are six level density models available in TALYS-1.6 (Koning *et al*., 2012, 2013) which are 1) **ldmodel 1**: the constant temperature and Fermi-gas model, 2) **ldmodel 2**: the back-shifted Fermi-gas model, 3) **ldmodel 3**: the generalized superfluid model, 4) **ldmodel 4**: the microscopic level densities (Skyrme force) from Goriely's table, 5) **ldmodel 5**: the microscopic level densities (Skyrme force) from Hilaire's table and 6) **ldmodel 6**: the Microscopic Level Densities (temperature-dependent HFD, Gogny force) from Hilaire's table.

The sensitivity of five different γ-ray strength functions available in TALYS-1.6 was also studied. They are 1) **strength 1**: Kopecky-Uhl generalized Lorentzian (Kopecky *et al.,* 1990), 2) **strength 2**: Brink-Axel Lorentzian (Brink, 1957; Axel, 1962), 3) **strength 3**: Hartree-Fock BCS tables (Capote *et al.,* 2009), 4) **strength 4**: Hartree-Fock-Bogolyubov tables (Capote *et al.,* 2009) and, 5) **strength 5**: Goriely's hybrid model (Goriely *et al.,* 1998).

The theoretical calculations have been done using the default parameter values except for the level density models and γ-ray strength functions.

### 4.1. Hauser-Feshbach Model

The theoretical model calculations to nuclear data evaluations have advantages

due to their ability to predict unknown nuclear reaction cross sections and some physical quantities that are very hard to measure experimentally including astrophysics and nuclear data for science and technology. The modern nuclear data libraries are calculated by using some model code like the optical model, the statistical Hauser-Feshbach (HF) model, and the pre-equilibrium model. Here, we focus only the statistical Hauser-Feshbach model. In the statistical Hauser-Feshbach model, the compound nuclear reactions on the excited state are calculated with both transmission coefficients of outgoing particles and the nuclear level density (NLD) of the residual nucleus. The nuclear reaction code TALYS (Koning *et al*., 2013) implements the HF mechanism for evaluating the nuclear reaction cross sections using different input level density models. The nuclear level density is the essential input for the calculation of compound nuclear reactions reaction cross sections in the framework of Hauser-Feshbach theory.

In the Hauser-Feshbach Model, the (*a*; *b*) reaction cross section $\sigma_{a,b}(E)$ corresponding to the decay in channel *b* (particle type, energy, outgoing angular momentum) from the compound nucleus (CN) formed in the entrance channel *a*, is given by (Herman *et al*., 2013):

$$\sigma_{a,b}(E) = \sum_{J,\pi} \sigma_a^{CN}(E,J,\pi) P_b(E,J,\pi) \quad ---(55)$$

where, $\sum_{J,\pi} \sigma_a^{CN}(E,J,\pi)$ is the compound nucleus formation cross section at a given energy, spin and parity $(E,J,\pi)$ associated to the incident channel *a* and $P_b(E,J,\pi)$ represents the decay probability of the compound nucleus with the excitation energy $E_x$ in *b* channel. The decay probability defined in terms of transmission coefficients is given by

$$P_p(E,J,\pi) = \frac{T_b(E_x,J,\pi)}{\sum_c T_c(E_x,J,\pi)} \quad ---(56)$$

which is associated to the reaction channels which might be particles emission, photon emission or fission. Here, the transmission coefficients $T_c$ correspond to the decay probability in outgoing channel *c*. The expression for the transmission coefficient for the *p* particle emission is given by:

$$T_p(E,J,\pi) = \sum_{I=|J-j|}^{I=J+j} \int_0^{E_x-B_p} \sum_{lj} T_{p,lj}\left(E_x - B_p + \varepsilon\right) \rho(\varepsilon, I, \pi_I)\delta(\pi\pi_l, (-1)^l) d\varepsilon \quad ---(57),$$

where $B_p$ is the separation energy of particle *p* in the compound nucleus, $\rho(\varepsilon, I, \pi_I)$ is residual nucleus level density with the spin and parity $(I, \pi_I)$, and the excitation energy $\varepsilon$ remaining in the residual nucleus obtained after emitting a particle in a channel *c*, and $T_{p,lj}$ is the transmission coefficient for particle *c* having channel energy $\left(E_x - B_p + \varepsilon\right)$ and orbital angular momentum *l*, which together with the particle spin *s* couples to the channel angular momentum *j* used to select in the residual nucleus spins *I* populated for a given compound nucleus spin *J*. The factor $\delta(\pi\pi_l, (-1)^l)$ corresponds to the parity conservation. For the discrete levels characterized by the energy $E_i$, spin $I_i$, and parity $\pi_{I_i}$, the level density $\rho\left(\varepsilon, I, \pi_\gamma\right)$ reduces to $\delta(\varepsilon - E_i)\delta(I, I_i)\delta(\pi_I, \pi_{I_i})$. For the gamma-decay coefficient, a similar expression is applied (Herman *et al*., 2013) as:

$$T_\gamma(E, J\pi) = \sum_{lj} T_{p,lj} \sum_{I=|J-j|}^{I=J+j} \int_0^{E_x-B_p} f_{Xl}\left(\varepsilon_\gamma\right) \rho\left(E_x - \varepsilon_\gamma, J', \pi'\right)\delta(\pi\pi', (-1)^l) d\varepsilon_\gamma \quad --(58)$$

where, *XL* represents the photon type and multipole, $f_{XL}\left(\varepsilon_\gamma\right)$ is the γ-ray strength function and $(J', \pi')$ are the spin and parity of the final states.

### 4.2. Level Density Models

In nuclear statistical models, nuclear level densities are used at excitation energies where discrete level information is not available or incomplete. Several

models are used for the level density in TALYS, which range from phenomenological analytical expressions to tabulated level densities derived from microscopic models. From Koning *et al.*, 2008b, the complete details can be found. In order to set the notation, some preferred definitions is accustomed first. The nuclear level density $\rho(E_x, J, \Pi)$ is arising from the number of discrete nuclear levels per MeV within an excitation energy $E_x$, for a certain spin $J$ and parity $\Pi$. The *total level density* $\rho^{tot}(E_x)$ arising from the total number of nuclear levels per MeV within $E_x$ is obtained by summing the level densities over all spins and parities:

$$\rho^{tot}(E_x) = \sum_{J} \sum_{\Pi} \rho(E_x, J, \Pi) - - - (59),$$

The total state density $\omega^{tot}(E_x)$ with the $2J + 1$ states for each level is obtained when the magnetic quantum number M degenerates the nuclear levels. It is given by:

$$\omega^{tot}(E_x) = \sum_{J} \sum_{\Pi} (2J + 1)\rho(E_x, J, \Pi) - - - (60),$$

When the analytical expressions provide the level densities, they are usually factorized as follows

$$\rho(E_x, J, \Pi) = P(E_x, J, \Pi)R(E_x, J)\rho^{tot}(E_x) - - - (61),$$

where, $P(E_x, J, \Pi)$ is the parity distribution and $R(E_x, J)$ the spin distribution. In all but one level density model in TALYS (**ldmodel 5**), the parity equipartition is assumed, *i.e.*,

$$P(E_x, J, \Pi) = \frac{1}{2} - - - (62).$$

However, in the programming, it has been accounted for the possibility to adopt non-equidistant parities, such as e.g. in the case of microscopic level density tables.

The following five level density models available in TALYS-1.6 (Koning *et al*., 2008a; 2013) were explained in brief as:

### 4.2.1. ldmodel 1: the Constant Temperature and Fermi-gas Model

In this model, the constant temperature model is used in the low excitation region and the Fermi-gas model is used in the high excitation energy region. The transition energy is around the neutron separation energy.

#### 4.2.1.1. The Fermi Gas Model

The Fermi Gas model (FGM) is one of the best analytical level density expression. It is based on the assumption that, at the Fermi energy, the excited levels of the nucleus constructed by the single particle states are equally spaced, but not including the collective levels. For the density states of a two-fermion system, *i.e.*, distinguishing between excited neutrons and protons, the total Fermi gas state density reads

$$\omega_F^{tot}(E_x) = \frac{\sqrt{\pi}}{12}\frac{exp\left[2\sqrt{\mathrm{a}U}\right]}{\mathrm{a}^{1/4}U^{5/4}} - - - (63),$$

here, the effective excitation energy, *U* is defined by:

$$U = E_x - \Delta - - - (64),$$

where, the energy shift Δ is an empirical parameter which is equivalent to, or for some models closely associated with, the pairing energy which is incorporated to simulate the known odd-even effects in nuclei. The underlying concept is that Δ represents the way that pairs of nucleons should be separated before every part will be excited separately. Practically, Δ plays an important function as the adjustable parameter to breed observables, and its definition can be diverse for the different models that are being mentioned here. **Eq. (63)** demonstrates that all through this manual, it will be used both the *true* excitation energy $E_x$, as fundamental running variable and for expressions associated with discrete levels, and the *effective* excitation energy *U*, mostly for expressions accompanying to the continuum.

**Eq. (63)** also contains the level density parameter *a*, given by $\alpha = \frac{\pi^2}{6}(g_\pi + g_v)$, where $g_\pi(g_v)$ denotes the spacing of the proton (neutron) single particle states near the Fermi energy. In practice, **Eq. (63)** is used to determine *a* from the experimental information of the specific nucleus under consideration or from global systematics. In contemporary analytical models, *a* is energy-dependent. This will be discussed in more detail below.

The expression of the Fermi gas level density can be derived with the total angular momentum (Ericson, 1960) as:

$$\rho_F(E_x, J, \Pi) = \frac{1}{2}\frac{2J+1}{\sqrt{2\pi}\sigma^3} exp\left[-\frac{\left(J+\frac{1}{2}\right)^2}{2\sigma^2}\right]\frac{\sqrt{\pi}}{12}\frac{\exp[2\sqrt{aU}]}{a^{1/4}U^{5/4}} - - - (65)$$

where $J$ and $\Pi$ are the nuclear spin and parity, the first factor 1/2 represents the aforementioned equiparity distribution and $\sigma^2$ is the spin cut-off parameter, which represents the Gaussian width of the angular momentum distribution $J$. It relies on excitation energy. **Eq. (65)** is a special case of the factorization of **Eq. (61)**, with the Fermi gas spin distribution given by,

$$R_F(E_x, J) = \frac{2J+1}{2\sigma^2} exp\left[-\frac{\left(J+\frac{1}{2}\right)^2}{2\sigma^2}\right] - - - (66).$$

Summing $\rho_F(E_x, J, \Pi)$ over all spins and parities provides the total Fermi gas level density:

$$\rho_F^{tot}(E_x) = \frac{1}{\sqrt{2\pi}\sigma}\frac{\sqrt{\pi}}{12}\frac{\exp\left[2\sqrt{aU}\right]}{a^{\frac{1}{4}}U^{\frac{5}{4}}} - - - (67),$$

The above **Eq. (67)** is related through **Eq. (86)**, to the total Fermi gas state density:

$$\rho_F^{tot}(E_x) = \frac{\omega_F^{tot}(E_x)}{\sqrt{2\pi}\sigma} - - - (68).$$

These equations show that the nuclear level densities $\rho_F^{tot}$ and $\rho_F$ are determined by three parameters, $a$, $\sigma$, and $\Delta$.

In the Fermi gas model, the level density parameter $a$ can be determined from $D_0$, the mean s-wave neutron level spacing at the neutron separation energy $S_n$ of the compound nucleus, which is usually obtained from the available experimental set of s-wave resonances. For any level density, the average resonance spacing parameters $D_0$ at the neutron separation energy $S_n$ can be given as:

$$\frac{1}{D_0} = \sum_{J=\left|I-\frac{1}{2}\right|}^{J=I+\frac{1}{2}} \rho_F(S_n, J, \Pi) \quad (69)$$

where, $I$ represents the spin of the target nucleus. From the above equation, it is possible to extract the level density parameter $a$ by an iterative search procedure.

The spin cut-off parameter $\sigma^2$ characterizes the Gaussian width of the angular momentum distribution of the level density. The general expression for the continuum can be formulated based on the observation that a nucleus possesses a collective rotational energy that cannot be utilized to excite the individual nucleons. Fermi gas spin cut-off parameter $\sigma_F^2$ is given by:

$$\sigma_F^2(E_x) = 0.01389 \frac{A^{5/3}}{\tilde{a}} \sqrt{aU} \quad (70)$$

where, $\tilde{a}$ is an asymptotic level density parameter obtained when all shell effects are damped and $A$ is the atomic mass number. On average, the $\sqrt{aU}/\tilde{a}$ term has the same energy- and mass-dependent behaviour as the temperature $\sqrt{U/a}$. Defining $E_d = (1/2)(E_L + E_U)$ as the energy at the mid-point of a lower discrete level $N_L$ with energy $E_L$ and an upper level $N_U$ with energy $E_U$ region, we assume discrete spin cut-off parameter $\sigma_d^2$ is constant up to this energy and can then be linearly interpolated to the

expression given by **Eq. (70)**. The matching point is chosen to be the neutron separation energy $S_n$ of the nucleus under consideration, *i.e.*,

$$\sigma^2(E_x) = \sigma_d^2 \qquad for\ 0 \le E_x \le E_d$$

$$= \sigma_d^2 + \frac{E_x - E_d}{S_n - E_d}(\sigma_F^2(E_x) - \sigma_d^2) \quad for\ \ E_d \le E_x \le S_n$$

$$= \sigma_F^2(E_x) \quad for\ \ E_x \le S_n \qquad ---(71).$$

In the TALYS-output, all quantities of interest are printed, if requested.

#### 4.2.1.2. Constant Temperature Model

Gilbert and Cameron (Gilbert *et al.*, 1965) introduced the Constant Temperature Model (CTM). According to them, in this model, the excitation energy range is separated into two energy regions, such as: (i) a low energy region starting from 0 MeV up to a matching energy $E_M$, where the so-called constant temperature law is used and (ii) a high energy region above $E_M$, where the Fermi gas model is adopted. Therefore, in the CTM for the total level density, we have

$$\rho^{tot}(E_x) = \rho_T^{tot}(E_x),\ \ if\ E_x \le E_M \quad ---(72),$$

$$= \rho_F^{tot}(E_x),\ \ if\ E_x \ge E_M \quad ---(73),$$

and similarly for the level density

$$\rho(E_x, J, \Pi) = \frac{1}{2} R_F(E_x, J)\rho_T^{tot}(E_x),\ \ if\ E_x \le E_M \quad ---(74),$$

$$= \rho_F(E_x, J, \Pi)\ \ if\ E_x \ge E_M \quad ---(75).$$

It is noted that, in the constant temperature region, the Fermi gas spin distribution of **Eq. (66)** and the low-energy behaviour for the Fermi gas spin cut-off parameter as expressed by **Eq. (71)** are also used.

The effective excitation energy, $U = E_x - \Delta^{CTM}$ is used for the Fermi gas expression, where the energy shift is given by

$$\Delta^{CTM} = \chi \frac{12}{\sqrt{A}} - - - (76),$$

with

$$\chi = 0, \ \ for\ odd - odd,$$

$$= 1, \ \ for\ odd - even,$$

$$= 2, \ for\ even - even - - - (77).$$

Note that, in TALYS, by using a default, no adjustable pairing shift parameter is used in the CTM. In **Eq. (76),** a number 12 in the numerator can be changed using the **pairconstant** keyword. This can also be applied to the other level density models.

In the case of low excitation energy, the CTM relied on the experimental evidence that the cumulative number of levels $N(E_{\mathrm{x}})$ of the first discrete levels can be well reproduced by an exponential law of the form

$$N(E_{\mathrm{x}}) = \exp\left(\frac{E_{\mathrm{x}} - E_0}{T}\right) - - - (78).$$

The above expression is called the constant temperature law. The adjustable parameters, the nuclear temperature $T$, and the normalization factor $E_0$ adjust the formula to the experimental discrete levels. Accordingly, the constant temperature part $N(E_{\mathrm{x}})$ is related to the total level density by the equation:

$$\rho_F^{tot}(E_x) = \frac{dN(E_{\mathrm{x}})}{dE_{\mathrm{x}}} = \frac{1}{T}\exp\left(\frac{E_x - E_0}{T}\right) - - - (79).$$

In the case of higher energies, the Fermi gas model is more suitable and the total level density is given by **Eq. (67)**. The expressions for $\rho_{\mathrm{T}}^{\mathrm{tot}}$ and $\rho_{\mathrm{F}}^{\mathrm{tot}}$ are adjusted to match each other at a matching energy $E_{\mathrm{M}}$ in order to become they, and their derivatives, identical. According to continuity equation, we have,

$$\rho_{\mathrm{T}}^{\mathrm{tot}}(E_{\mathrm{M}}) = \rho_F^{tot}(E_{\mathrm{M}}) - - - (80).$$

Putting **Eq. (79)** in the above equation, we have the condition,

$$E_0 = E_{\mathrm{M}} - T\ln[T\rho_{\mathrm{F}}^{\mathrm{tot}}(E_{\mathrm{M}})] - - - (81)\,.$$

Again, according to the condition of continuity, the derivative of **Eq. (80)** becomes

$$\frac{d\rho_{\mathrm{T}}^{\mathrm{tot}}}{dE_{\mathrm{x}}}(E_{\mathrm{M}}) = \frac{d\rho_{\mathrm{F}}^{\mathrm{tot}}}{dE_{\mathrm{x}}}(E_{\mathrm{M}}) - - - (82).$$

Thus, putting **Eq. (79)** in the above equation, we have the condition,

$$\frac{d\rho_{\mathrm{T}}^{\mathrm{tot}}}{T}(E_{\mathrm{M}}) = \frac{d\rho_{\mathrm{F}}^{\mathrm{tot}}}{dE_{\mathrm{x}}}(E_{\mathrm{M}}) - - - (83),$$

or

$$\frac{1}{T} = \frac{d\ln\rho_{\mathrm{F}}^{\mathrm{tot}}}{dE_{\mathrm{x}}}(E_{\mathrm{M}}) - - - (84)\,.$$

In principle, **Eq. (84)** could be elaborated analytically for all Fermi gas type expressions including the energy dependent expressions for $a$, $\sigma^2$, and $K_{\mathrm{rot}}$ etc., but in practice, we use a numerical method of solution to allow any level density model to be used in the matching problem. For this, the inverse temperature of **Eq. (84)** is determined numerically by calculating $\rho_{\mathrm{F}}^{\mathrm{tot}}$ on a sufficiently dense energy grid.

The matching problem given by **Eqs. (81)** and **(84)** provides two conditions with three unknowns: $T$, $E_0$ and $E_{\mathrm{M}}$. Hence, another constraint is needed. This is obtained by demanding that in the discrete level region, the constant temperature law reproduces the experimental discrete levels from a lower level $N_{\mathrm{L}}$ with energy $E_{\mathrm{L}}$ to an upper level $N_{\mathrm{U}}$ with energy $E_{\mathrm{U}}$, *i.e.*, $\rho_{\mathrm{T}}^{\mathrm{tot}}$ needs to obey

$$N_{\mathrm{U}} = N_{\mathrm{L}} + \int_{E_{\mathrm{L}}}^{E_{\mathrm{U}}} dE_{\mathrm{x}}\rho^{\mathrm{tot}}(E_{\mathrm{x}}) - - - (85),$$

or, after inserting **Eq. (79)**,

$$N_{\mathrm{U}} = N_{\mathrm{L}} + \left(\exp\left[\frac{E_{\mathrm{U}}}{T}\right] - \exp\left[\frac{E_{\mathrm{L}}}{T}\right]\right)\exp\left[\frac{-E_0}{T}\right] - - - (86).$$

The combination of **Eqs. (81)**, **(84)** and **(86)** determines $T$, $E_0$ and $E_{\mathrm{M}}$. Putting **Eq. (81)** in **Eq. (86)**, we have,

$$T\rho_{\mathrm{T}}^{\mathrm{tot}}(E_{\mathrm{M}})\exp\left[\frac{-E_{\mathrm{M}}}{T}\right]\left(\exp\left[\frac{E_{\mathrm{U}}}{T}\right]-\exp\left[\frac{E_{\mathrm{L}}}{T}\right]\right)+N_{\mathrm{L}}-N_{\mathrm{U}}=0---(87).$$

From the above **Eq. (87)**, $E_{\mathrm{M}}$ can be elaborated by an iterative procedure with the simultaneous adoption of the tabulated values given by **Eq. (84).** When the discrete levels $N_{\mathrm{L}}$ and $N_{\mathrm{U}}$ are selected, $\rho_{\mathrm{T}}(E_{\mathrm{x}})$ provides the best explanation of the observed discrete states and are stored in the nuclear structure database. For nuclides for which no, or not sufficient, discrete levels are given, we depend on empirical formula for the temperature. For the effective model (Koning *et al*., 2013), we have,

$$T=-0.22+\frac{9.4}{\sqrt{A(1+\gamma\delta W)}}---(88)$$

and for the collective model

$$T=-0.25+\frac{10.2}{\sqrt{A(1+\gamma\delta W)}}---(89)$$

where $\gamma$ is the global parameter and its values are given in Talys manual. $E_{\mathrm{M}}$ can be obtained directly from **Eq. (84)** and $E_0$ from **Eq. (88)**. Again, by fitting all individual values of the nuclides, **Eqs. (84)** and **(89)** were obtained, for which sufficient discrete level information exists. In a few cases, the global expression for *T* may lead to a value for $E_{\mathrm{M}}$ that is too high. In such cases, we rely for the matching energy on the empirical expressions. For the effective model, we have,

$$E_{\mathrm{M}}=2.33+\frac{253}{A}+\Delta^{CTM}---(90),$$

and for the collective model, we have,

$$E_{\mathrm{M}}=2.67+\frac{253}{A}+\Delta^{CTM}---(91),$$

after which *T* is obtained from **Eq. (84).**

### 4.2.2. ldmodel 2: The Back-shifted Fermi gas Model

The Back-shifted Fermi gas Model (BFM) (Goriely *et al.*, 2011) is a modified

model of Fermi Gas Model (FGM). In this model, the pairing energy is treated as an adjustable parameter and the Fermi gas expression is used to describe the level density all the way down to 0 MeV. Hence, the total level density is given as,

$$\rho_F^{tot}(E_x) = \frac{1}{\sqrt{2\pi}\sigma}\frac{\sqrt{\pi}}{12}\frac{\exp\left[2\sqrt{\alpha U}\right]}{\alpha^{1/4}U^{5/4}} - - - (92),$$

and the level density is,

$$\rho_F(E_x, J, \Pi) = \frac{1}{2}\frac{2J+1}{2\sqrt{2\pi}\sigma^3}\exp\left[-\frac{(J+\frac{1}{2})^2}{2\sigma^2}\right]\frac{\sqrt{\pi}}{12}\frac{\exp\left[2\sqrt{\alpha U}\right]}{\alpha^{1/4}U^{5/4}} - - - (93),$$

respectively. These expressions, as well as the energy-dependent expressions for *a* and $\sigma^2$, contain the effective excitation energy $U = E_x - \Delta^{BFM}$, where the energy shift is given by

$$\Delta^{BFM} = \chi\frac{12}{\sqrt{A}} + \delta - - - (94),$$

with

$$\chi = -1, \ for\ odd - odd,$$
$$= 0, \ for\ odd - even,$$
$$= 1, \ for\ even - even - - - (95).$$

and $\delta$ an adjustable parameter to fit experimental data per nucleus.

When *U* goes to zero, a problem occurs in the original BFM, which may have hampered its use as the default level density option in nuclear model analyses, is the divergence of **Eqs. (92)** and **(93)**. Grossjean and Feldmeier (1985) have been provided a solution for this problem and it has been put into a practical form by Demetriou and Goriely (2001), which is adopted in TALYS (Koning *et al*., 2008b). Thus, the total BFM level density is given by,

$$\rho_{BFM}^{tot}(E_x) = \left[\frac{1}{\rho_F^{tot}(E_x)} + \frac{1}{\rho_0(t)}\right]^{-1} - - - (96),$$

here, $\rho_0$ is given by

$$\rho_0(t) = \frac{\exp(1)}{24\sigma}\frac{(\mathrm{a_n} + \mathrm{a_p})^2}{\sqrt{\mathrm{a_n}\mathrm{a_p}}}\exp\left(4\mathrm{a_n}\mathrm{a_p}t^2\right) - - - (97),$$

where, $a_n = a_p = a/2$ and $t$ is thermodynamical temperature given by $\sqrt{U/\mathrm{a}}$. With the usual spin distribution, the level density can be given as,

$$\rho_{BFM}(E_x, J, \Pi) = \frac{1}{2}\frac{2J+1}{2\sigma^2}\exp\left[-\frac{\left(\mathrm{J}+\frac{1}{2}\right)^2}{2\sigma^2}\right]\rho_{\mathrm{BFM}}^{\mathrm{tot}}(E_{\mathrm{x}}) - - - (98).$$

In sum, there are two adjustable parameters for the BFM, $a$ and δ.

### 4.2.3. ldmodel 3: the Generalized Superfluid Model

The Generalized Superfluid Model (GSM) is based on the Bardeen-Cooper-Schrieffer theory, which includes pairing correlations that produce the superfluid characteristics of this model (Ignatyuk *et al*., 1993). The phenomenological model (Larsen *et al*., 2010a; Larsen *et al*., 2010b) is characterized by a phase transition from a super fluid behaviour at low energy, where the level density is strongly influenced by pairing correlations, to a high energy region which is described by the Fermi Gas Model (FGM). Therefore, the GSM is similar to the Constant Temperature Model to the extent that it distinguishes between a low energy and a high energy region, although for the GSM, this distinction follows naturally from the theory and does not rely upon specific discrete levels that determine a matching energy. Instead, at low energies, the model automatically provides a constant temperature-like behaviour. For the level density expressions, it is helpful to remember the general formula for the total level density,

$$\rho^{tot}(E_x) = \frac{1}{\sqrt{2\pi}\sigma}\frac{e^S}{\sqrt{D}} - - - (99),$$

where, $S$ is the entropy and $D$ is the determinant related to the saddle-point

approximation. In the GSM, the level density has to be treated separately in two energy regions which are separated by the temperature called the critical temperature $T_c$ and the excitation energy corresponding to the critical temperature called the critical energy $U_c$, can be expressed as

$$U_c = a_c T_c^2 + E_{cond} - - - (100) .$$

Here, the critical temperature $T_c$ is

$$T_c = 0.567\Delta_0 - - - (101),$$

where, the pairing correlation function is given by

$$\Delta_0 = \frac{12}{\sqrt{A}} - - - (102).$$

Also, $E_{cond}$ is the condensation energy, which describes the decreasing of the superfluid phase in respect to the Fermi gas phase. It is given by:

$$E_{cond} = \frac{3}{2\pi^2} a_c \Delta_0^2 - - - (103),$$

where, $a_c$ is the critical level density parameter, which can be determined by the iterative equation

$$a_c = \tilde{a}\left[1 + \delta W \frac{1 - \exp(-\gamma a_c T_c^2)}{a_c T_c^2}\right] - - - (104) ,$$

where, $\tilde{a}$ is the asymptotic value of the level density parameter, $\delta W$ is the shell correction and $\gamma$ is the shell effects damping parameter. **Eq. (104)** indicates that shell effects are again appropriately taken into account. For the determination of the level density, the critical entropy $S_c$, and the critical determinant $D_c$ are defined by the following expressions:

$$S_c = 2a_c T_c - - - (105) ,$$

and,

$$D_c = \frac{144}{\pi} a_c^3 T_c^5 - - - (106),$$

Also, the critical spin cut-off parameter $\sigma_c^2$ can be given by

$$\sigma_c^2 = 0.01389A^{5/3}\frac{a_c}{\tilde{a}}T_c - - - (107)$$

Since everything is specified at $U_c$, we can utilize the superfluid Equation Of State (EOS) to characterize the level density below $U_c$. For this, we define the effective excitation energy

$$U' = E_x + \chi\Delta_0 + \delta - - - (108),$$

where,

$$\chi = 1,\ for\ odd - even,$$
$$= 0,\ for\ even - even$$
$$= 2,\ for\ odd - odd, - - -(109).$$

and $\delta$ is an adjustable shift parameter to obtain the best description of experimental data per nucleus (Koning *et al*., 2008b). The function $\varphi$ introduced at effective excitation energies below $U_c$, in the energy range where the superconductivity model BCS (Ignatyuk *et al*., 1979) applies is given as

$$\varphi^2 = 1 - \frac{U'}{U_c} - - - (110).$$

Then, the relation between the function $\varphi$ and temperature $T$ obeying the superfluid EOS for the excitation energy $U' \leq U_c$ (Ignatyuk *et al*., 1979), can be given by the equation,

$$\varphi = \tanh\left(\frac{T_c}{T}\varphi\right) - - - (111),$$

which is equivalent to

$$T = 2T_c\varphi\left[ln\frac{1+\varphi}{1-\varphi}\right]^{-1} - - - (112)$$

The other required functions for $U' \leq U_c$ are the entropy S, given by:

$$S = S_{\mathrm{c}}\frac{T_c}{T}(1-\varphi^2) = S_{\mathrm{c}}\frac{T_{\mathrm{c}}}{T}\frac{U'}{U_{\mathrm{c}}} - - - (113),$$

the determinant *D*, given by the expression:

$$D = D_{\mathrm{c}}(1-\varphi^2)(1+\varphi^2)^2 = D_{\mathrm{c}}\frac{U'}{U_{\mathrm{c}}}(2-\frac{U'}{U_{\mathrm{c}}})^2 - - - (114)$$

and the spin cut-off parameter

$$\sigma^2 = \sigma_{\mathrm{c}}^2(1-\varphi^2) = \sigma_{\mathrm{c}}^2\frac{U'}{U_{\mathrm{c}}} - - - (115)$$

In sum, the level density can now be specified for the entire energy range. For $U' \leq U_c$ , the total level density is given by

$$\rho_{GSM}^{tot}(E_{\mathrm{x}}) = \frac{1}{\sqrt{2\pi}\sigma}\frac{e^S}{\sqrt{D}} - - - (116),$$

using **Eqs. (113)** and **(114)**. Similarly, the level density is

$$\rho_{\mathrm{GSM}}(E_x, J, \Pi) = \frac{1}{2}R_{\mathrm{F}}(E_x, J)\rho_{\mathrm{GSM}}^{\mathrm{tot}}(E_{\mathrm{x}}) - - - (117)$$

For $U' \leq U_c$, the FGM applies though with an energy shift, that is, different from the pairing correction of the CTM and BFM. The total level density is

$$\rho_{GSM}^{tot}(E_{\mathrm{x}}) = \frac{1}{\sqrt{2\pi}\sigma}\frac{\sqrt{\pi}}{12}\frac{\left[2\sqrt{aU}\right]}{\mathrm{a}^{1/4}U^{5/4}} - - - (118),$$

where the effective excitation energy is defined by $U = E_{\mathrm{x}} - \Delta^{\mathrm{GSM}}$, with

$$\Delta^{\mathrm{GSM}} = E_{\mathrm{cond}} - \chi\Delta_0 - \delta - - - (119),$$

The spin cut-off parameter in the high-energy region reads

$$\sigma^2 = I_0\frac{\mathrm{a}}{\tilde{\mathrm{a}}}\sqrt{\frac{U}{\mathrm{a}}} - - - (120),$$

and $I_0$ is the moment of inertia of the nucleus given by $[(2/5)m_0R^2A]/(\hbar c)^2$ where, $R=1.2A^{1/3}$ is the radius and $m_0$ is the neutron mass in amu. The level density is given by

$$\rho_{\mathrm{GSM}}(E_{\mathrm{x}},J,\Pi)=\frac{1}{2}R_{\mathrm{F}}(E_{\mathrm{x}},J)\rho_{\mathrm{GSM}}^{\mathrm{tot}}(E_{\mathrm{x}})---(121).$$

At the matching energy, *i.e.*, for $E_{\mathrm{x}}'=U_{\mathrm{c}}-\chi\Delta_0-\delta$, it is easy to verify that **Eqs. (116)** and **(118)** match so that the total level density is perfectly continuous. In sum, there are two adjustable parameters for the GSM, $a$ and $\delta$.

### 4.2.4. ldmodel 4: the Microscopic Level Densities (Skyrme force) from Goriely's table.

Not only in TALYS, there are different options to employ more microscopic approaches to calculate the nuclear level densities. For the RIPL database, S. Goriely has calculated level densities using the Hartree-Fock calculations (Goriely *et al.*, 2001) for excitation energies up to 150 MeV and for spin values up to I = 30. If **ldmodel 4**, these tables with microscopic level densities can be read. Moreover, Hilaire and Goriely (Goriely *et al*., 2008) have been proposed the new energy-, spin- and parity-dependent nuclear level densities based on the microscopic combinatorial model. This combinatorial model consists of using single-particle level schemes obtained from the constrained axially symmetric Hartree-Fock-Bogoliubov (HFB) method and it describes an elaborated microscopic calculation of the intrinsic state density and collective enhancement. The phenomenological prospect of the model is only a simple damping function for the rotational effects. Within the deformed Skyrme-Hartree-Fock-Bogolyubov framework, these calculations make coherent use of nuclear structure properties (Koning *et al*., 2008b; 2013).

### 4.2.5. ldmodel 5: the Microscopic Level Densities (Skyrme force) from Hilaire's table.

In **ldmodel 5**, the nuclear level densities for more than 8500 nuclei are made available in the tabular format, for excitation energies up to 200 MeV and for spin

values up to J = 49 (Koning *et al*., 2008b; 2013).

### 4.2.6. ldmodel 6: the Microscopic Level Densities (temperature-dependent HFD, Gogny force) from Hilaire's table.

In **ldmodel 6**, the most recent option to employ the microscopic approaches to calculate the nuclear level densities is based on temperature-dependent Hartree-Fock-Bogolyubov calculations using the Gogny force (Koning et al., 2008b; Hilaire *et al*., 2012).

For both microscopic level density models, tables for level densities on top of the fission barriers are automatically invoked for **ldmodel 4, 5** or **6**, when available in the structure database. The default Fermi gas model is used for nuclides outside the tabulated microscopic database (Koning *et al*., 2013).

## 4.3. Gamma-ray Transmission Coefficients

In order to describe the gamma emission channel in nuclear reactions, the gamma-ray transmission coefficients are very important. Generally, since the gamma rays may accompany emission of any other emitted particle, the gamma emission channel is an almost universal channel. For the calculation of the competition of photons with other particles, the gamma-ray transmission coefficients enter the Hauser-Feshbach model, like the particle transmission coefficients that emerge from the optical model, (Koning *et al*., 2012).

For the multipolarity $\ell$ of type X (where X = M or E), the gamma-ray transmission coefficient $T_{X\ell}(E_\gamma)$ related to the corresponding strength function is given by

$$T_{X\ell}(E_\gamma) = 2\pi f_{X\ell}(E_\gamma) E_\gamma^{2\ell+1} \quad ---(122),$$

where, *E* denotes the gamma energy. Gamma-ray strength functions are important

constituents of the compound nucleus model calculations of capture cross sections, γ-ray production spectra, isomeric state populations, and competition between γ-ray and particle emission. The γ-ray strength functions include information on the nuclear structure, and are widely used to study the mechanisms of nuclear reactions as well as nuclear structure (Capote *et al*., 2009). The different γ-ray strength functions available in TALYS-1.6 were explained in brief in Sec-4.2.1. as (Koning *et al*., 2008a, 2013).

### 4.3.1. Gamma-ray Strength Functions

In Talys, there are four models for the gamma-ray strength function. The Brink-Axel Lorentzian Model is called the **strength 2** (Brink, 1957; Axel, 1962), in which a standard Lorentzian form describes the Giant Dipole Resonance (GDR) shape, *i.e.*,

$$f_{X\ell}(E_\gamma) = K_{X\ell}\frac{\sigma_{X\ell}E_\gamma\Gamma_{X\ell}^2}{(E_\gamma^2 - E_{X\ell}^2)^2 + E_\gamma^2\Gamma_{X\ell}^2} - - - (123),$$

where `$\sigma_{X\ell}$, $E_{X\ell}$ and $\Gamma_{X\ell}$ are the strength, energy and width of the giant resonance, respectively, and

$$K_{X\ell} = \frac{1}{(2\ell+1)\pi^2h^2c^2} - - - (124)$$

For all transition types other than E1, at present, the Brink-Axel option is applied. For E1 radiation in TALYS, the Kopecky-Uhl Generalized Lorentzian Model called **strength 1** is the default option (Kopecky, 1990), and is given as

$$f_{E1}(E_\gamma, T) = K_{E1}\left[\frac{E_\gamma\tilde{\Gamma}_{E1}(E_\gamma)}{(E_\gamma^2 - E_{E1}^2)^2 + E_\gamma^2\tilde{\Gamma}_{E1}(E_\gamma)^2} + \frac{0.7\Gamma_{E1}4\pi^2T^2}{E_{E1}^3}\right]\sigma_{E1}\Gamma_{E1} - -(125),$$

where, the energy-dependent damping width $\tilde{\Gamma}(E_\gamma)$ is given by

$$\tilde{\Gamma}_{E1}(E_\gamma) = \Gamma_{E1}\frac{E_\gamma^2 + 4\pi^2T^2}{E_{E1}^2} - - - (126),$$

and *T* is the nuclear temperature given by (Kopecky *et al.*, 1993)

$$T = \sqrt{\frac{E_n + S_n - \Delta - E_\gamma}{a(S_n)}} - - - (127)$$

where, $E_n$ is the incident neutron energy, $S_n$ the neutron separation energy, $\Delta$ the pairing correction and $a$ the level density parameter at $S_n$.

The parameters of GDR for various individual nuclides exist for *E*1-transitions, and in the nuclear structure database of TALYS, these parameters are stored. In the case of deformed nuclides, GDR strength function splits into two components, *i.e*. a second set of Lorentzian parameters. The incoherent sum of two strength functions is taken in these cases. For all transitions other than *E*1, Kopecky (Capote *et al*., 2009), compiled the systematic formulae for the resonance parameters. For *E*1 transitions, the following default parameters have been adopted for which no tabulated data exist (Koning *et al*., 2013):

$$- - -(128)$$

$$\sigma_{E1} = 1.2 \times \frac{120NZ}{(A\pi\Gamma_{E1})} mb\ ,$$

$$E_{E1} = 31.2A^{-1/3} + 20.66A^{-1/6}\ \text{MeV},$$

$$\Gamma_{E1} = 0.026E_{E1}^{1.91}\ \text{MeV}.$$

For *E*2 transitions, the following adopted default parameters of GQR are:

$$- - -(129)$$

$$\sigma_{E2} = \frac{0.00014Z^2E_{E2}}{A^{1/3}\Gamma_{E2}}\ mb\ ,$$

$$E_{E2} = 63.A^{-1/3}\ MeV\ \text{MeV}\ ,$$

$$\Gamma_{E2} = 6.11 - 0.012A\ MeV\ .$$

For multipole radiation higher than *E*2, the default parameters are:

$$- - -(130)$$

$$\sigma_{E\ell} = 8.10^{-4}\sigma_{E(\ell-1)}\,,$$

$$E_{E\ell} = E_{E(\ell-1)}\,,$$

$$\Gamma_{E\ell} = \Gamma_{E(\ell-1)}$$

For *M*1 transitions, the default parameterizations of the GMR are as follows:

$$---(131)$$

$$f_{M1} = 1.58A^{0.47} \text{ at 7 MeV},$$

$$E_{M1} = 41.A^{-1/3}\ MeV\,,$$

$$\Gamma_{M1} = 4\ MeV\,,$$

here, in order to obtain the $\Gamma_{M1}$ value, **Eq. (123)** needs to be applied at 7 MeV. For multipole radiation higher than *M*1, the following default parameters are used:

$$---(132)$$

$$\sigma_{M\ell} = 8.10^{-4}\sigma_{M(\ell-1)}\,,$$

$$E_{M\ell} = E_{M(\ell-1)}\,,$$

$$\Gamma_{M\ell} = \Gamma_{M(\ell-1)}$$

The systematics can be overruled with user-defined input parameters for all the cases.

Talys also provides two microscopic options for *E*1 radiation. According to the Hartree-Fock BCS Model, Stephane Goriely calculated gamma-ray strength function called **strength 3**, and he also calculated that function according to Hartree-Fock-Bogolyubov model, it is known as **strength 4**, see also Ref. (Capote *et al*., 2009). In the microscopical strength functions, two adjustment parameters $f^{nor}$ and $E_{shift}$ are introduced which is given in **Eq. (133)** as:

$$f_{\mathrm{E1}}(E_\gamma) = f^{nor} f_{\mathrm{HFM}}(E_\gamma + E_{shift}) --- (133)$$

here, $f^{nor} = 1$ and $E_{shift} = 0$ are the default parameters (*i.e*. unaltered values from the tables). The energy shift $E_{shift}$ simply suggests acquiring the level density from

the table at a different energy. By adjusting $f^{nor}$ and $E_{shift}$ together, it gives enough adjustment flexibility. A further detailed description of the model is given in TALYS user manual (Koning *et al*., 2013).

.

# CHAPTER 5

# RESULTS AND DISCUSSIONS

# 5. RESULTS AND DISCUSSIONS

The measured $^{70}Zn(n, \gamma)^{71}Zn^{m}$ cross sections are given in **Table 20** with their overall and partial uncertainties in **Table 19**. In **Table 20**, the ratio of the evaluated $^{70}Zn(n, \gamma)^{71}Zn^{m}$ cross sections in the TENDL-2015 library folded by the ($p$, $n_0$) neutron flux energy spectra $<\sigma_{Zn}{}^{m}>_{TENDL}$ to the measured cross sections are also given. Among the latest major libraries, JENDL-4.0 also provides an original evaluated data set for the $^{70}Zn(n, \gamma)^{71}Zn^{g+m}$ cross section (Kopecky, 1990; Brink, 1957) but not for the $^{70}Zn(n, \gamma)^{71}Zn^{m}$ cross section.

**Figures 25(a-e)** show the comparison of the present measured spectrum averaged $^{70}Zn(n, \gamma)^{71}Zn^{m}$ reaction cross sections and the cross sections for mono energetic neutrons predicted by TALYS-1.6 with various level density models and γ-ray strength functions. A sudden decrease in the $^{70}Zn(n, n_1)^{70}Zn^{m}$ cross section around 0.9 MeV was predicted by both TALYS-1.6 and TENDL-2015. This was due to the $^{70}Zn(n, n_1)^{70}Zn$ in elastic scattering channel. **Figure 25(a-e)** shows that the prediction by TALYS-1.6 was very sensitive to the choice of the level density models and the γ-ray strength functions. It could also be clearly seen that TALYS-1.6 with the generalized superfluid level model (**ldmodel 3**) along with the Kopecky-Uhl generalized Lorentzian gamma ray strength function (**strength 1**) in **Figure 25(c)** best matched the present measured cross sections.

In order to estimate the $^{70}Zn(n, \gamma)^{71}Zn^{g+m}$ cross sections from the measured $^{70}Zn(n, \gamma)^{71}Zn^{m}$ cross sections, the measured cross sections $<\sigma_{Zn}{}^{m}>_{exp}$ were multiplied by the isomeric ratios $<\sigma_{Zn}{}^{g+m}>_{TENDL}/<\sigma_{Zn}{}^{m}>_{TENDL}$ evaluated in TENDL-2015 folded by the $^{7}Li(p, n_0)$ neutron spectra. The ratios obtained were 1.6698 and 1.6823 at 0.96 and 1.69 MeV respectively as given in the **Table 21**. **Table 22** compares the derived

total neutron capture cross sections $<\sigma_{Zn}^{g+m}>_{present}$ with the ($p$, $n_0$) neutron flux energy spectrum averaged $^{70}Zn(n, \gamma)^{71}Zn^{g+m}$ cross sections evaluated in TENDL-2015 $<\sigma_{Zn}^{g+m}>_{TENDL}$, JENDL-4.0 $<\sigma_{Zn}^{g+m}>_{JENDL}$ as well as calculated by TALYS-1.6 with the generalized superfluid level density model (**ldmodel 3**) and Kopecky-Uhl generalized Lorentzian γ-ray strength function (**strength 1**), $<\sigma_{Zn}^{g+m}>_{TALYS}$.

**Table 20:** The $^{70}Zn(n, \gamma)^{71}Zn^{m}$ cross sections measured in the present experiment $<\sigma_{Zn}^{m}>_{exp}$ with their total uncertainties. The ratio of the evaluated cross sections in TENDL-2015 averaged by the ($p$, $n_0$) neutron flux energy spectra $<\sigma_{Zn}^{m}>_{TENDL}$ to the measured cross sections are also given.

| **$E_n$ (MeV)** | **$<\sigma_{Zn}^{m}>_{exp}$ (mb)** | **Correlation coefficients** | | **$<\sigma_{Zn}^{m}>_{TENDL}$/ $<\sigma_{Zn}^{m}>_{exp}$** |
|---|---|---|---|---|
| 0.96 ± 0.15 | 1.83 ± 0.16 | 1.00 | | 1.89 |
| 1.69 ± 0.15 | 1.33 ± 0.09 | 0.12 | 1.00 | 1.48 |

**(a)**

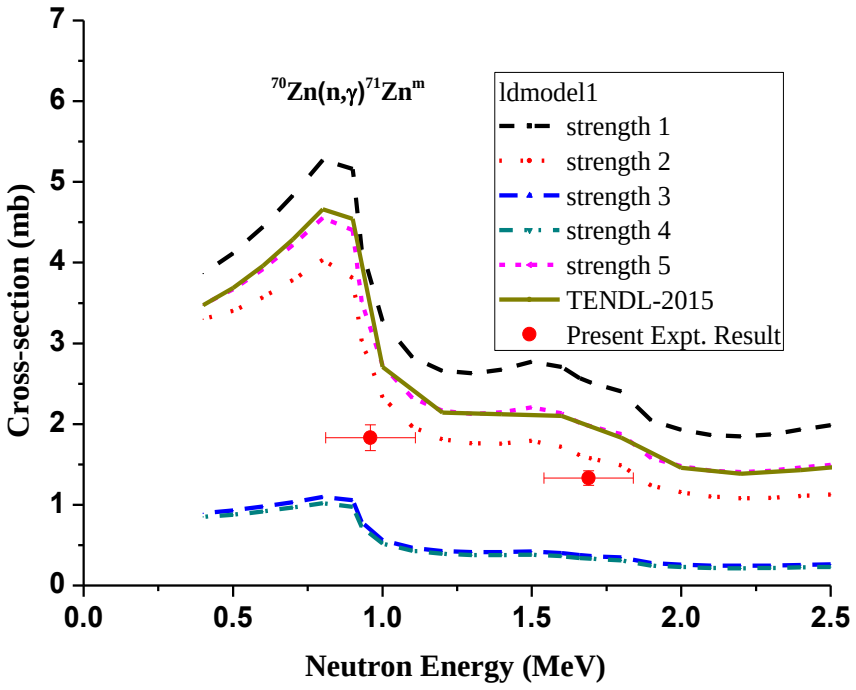

**(b)**

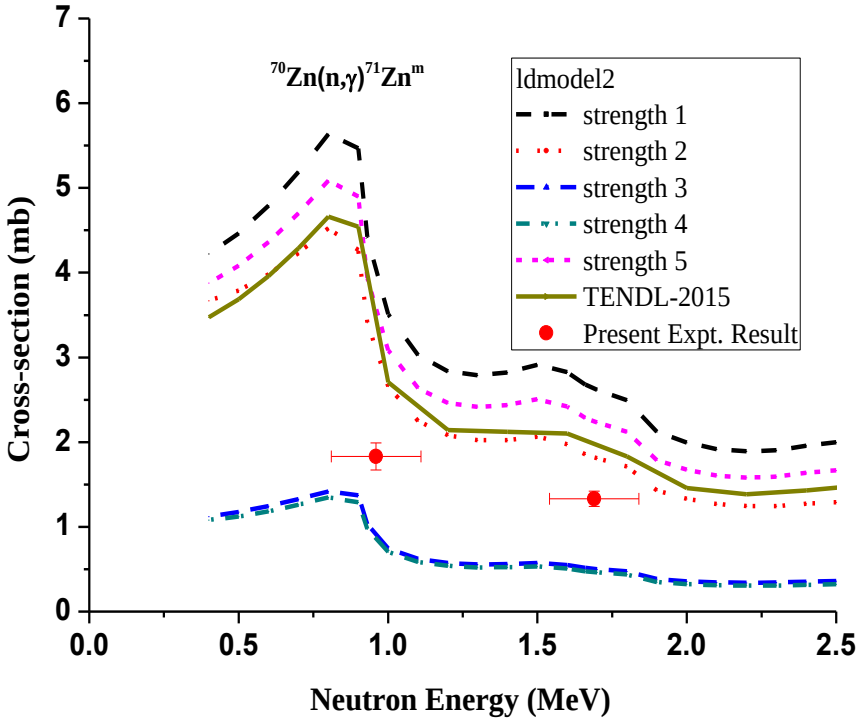
$^{70}Zn(n,\gamma)^{71}Zn^{m}$
ldmodel2
strength 1
strength 2
strength 3
strength 4
strength 5
TENDL-2015
Present Expt. Result
Cross-section (mb)
Neutron Energy (MeV)
0
1
2
3
4
5
6
7
0.0
0.5
1.0
1.5
2.0
2.5

**(c)**

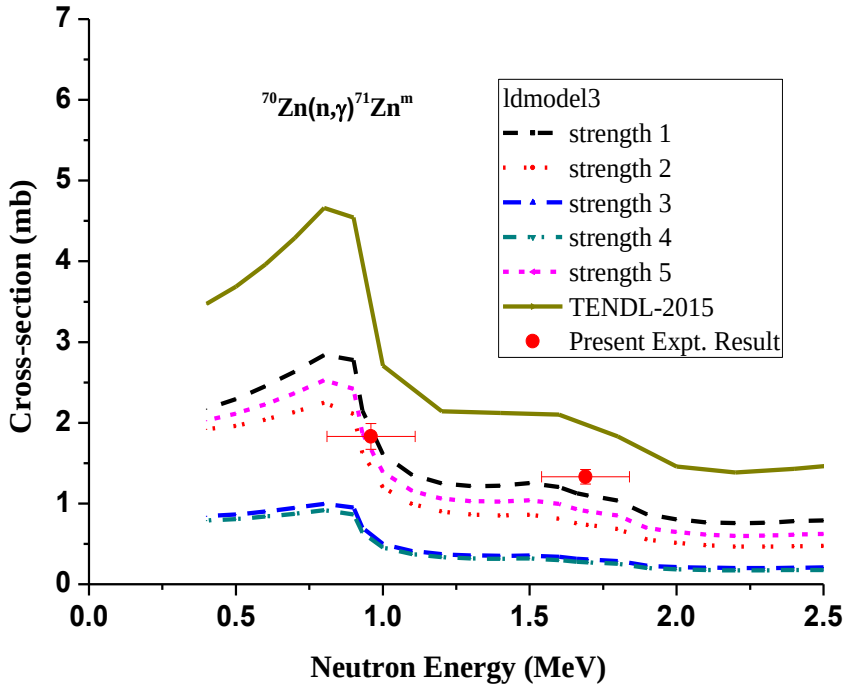
$^{70}Zn(n,\gamma)^{71}Zn^{m}$
ldmodel3
strength 1
strength 2
strength 3
strength 4
strength 5
TENDL-2015
Present Expt. Result
Cross-section (mb)
Neutron Energy (MeV)
0
1
2
3
4
5
6
7
0.0
0.5
1.0
1.5
2.0
2.5

**(d)**

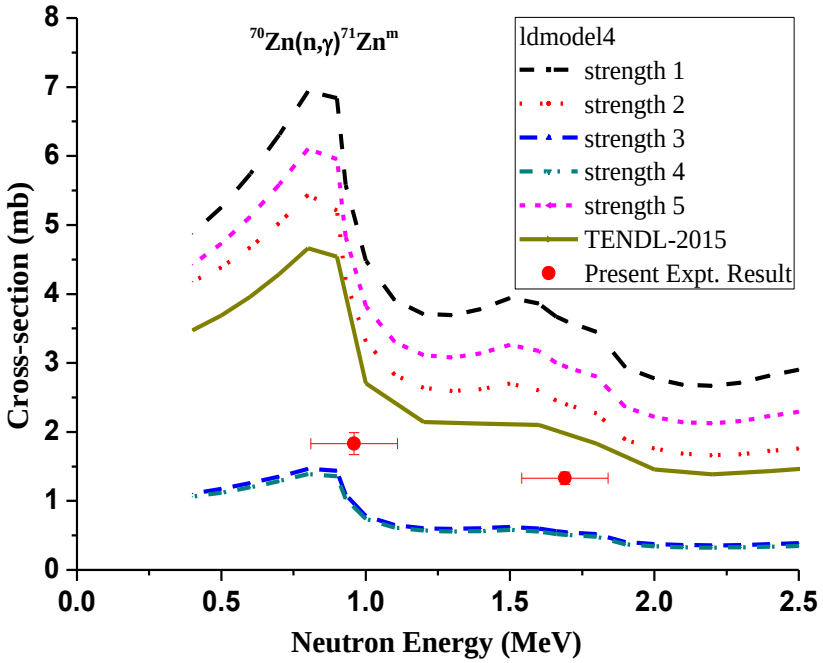


**(e)**

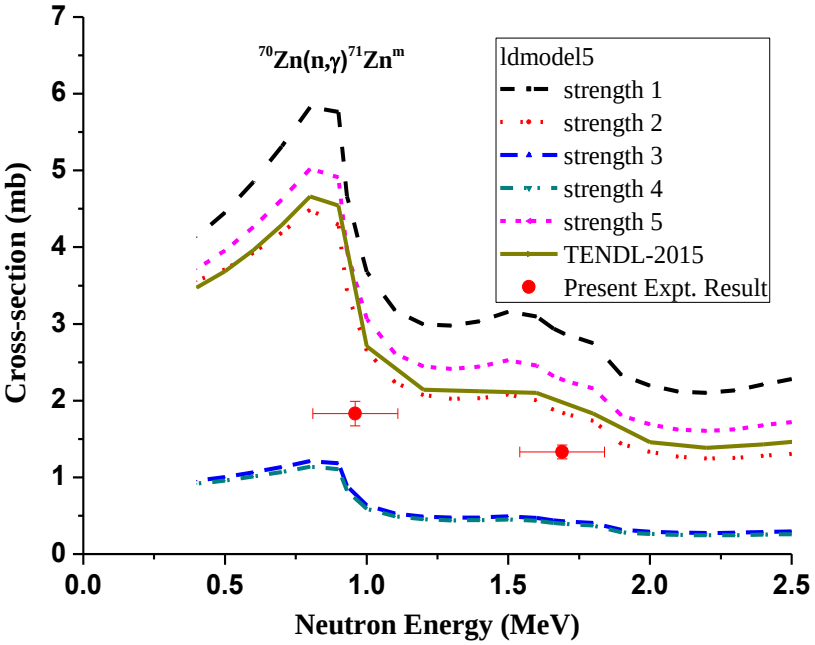


**Figure 25:** Excitation functions of the $^{70}$Zn(*n, γ*)$^{71}$Zn$^{m}$ cross sections measured in this work, evaluated in TENDL-2015 (solid line) as well as calculated by TALYS-1.6 with five different γ-ray strength functions (**strength 1 to 5**) with the level density models: (a) **ldmodel 1** (b) **ldmodel 2** (c) **ldmodel 3** (d) **ldmodel 4** and (e) **ldmodel 5** .

See text for the details of the γ-ray strength functions and level density models. The experimental cross sections were ($p$, $n_0$) neutron flux energy spectrum averaged while the evaluated and calculated cross sections were for mono energetic neutrons.

**Table 21:** The $^{70}Zn(n, \gamma)^{71}Zn^{m}$ and $^{70}Zn(n, \gamma)^{71}Zn^{g+m}$ cross sections folded by the ($p$, $n_0$) neutron flux energy spectra as well as their ratios in TENDL-2015.

| $E_n$ (MeV) | $\langle\sigma_{Zn}^{m}\rangle_{TENDL}$ | $\langle\sigma_{Zn}^{g+m}\rangle_{TENDL}$ | $\langle\sigma_{Zn}^{g+m}\rangle_{TENDL}$ / $\langle\sigma_{Zn}^{m}\rangle_{TENDL}$ |
|---|---|---|---|
| 0.96 ± 0.15 | 3.4567 | 5.7720 | 1.6698 |
| 1.69 ± 0.15 | 1.9689 | 3.3122 | 1.6823 |

**Table 22:** The $^{70}Zn(n, \gamma)^{71}Zn^{g+m}$ captured cross sections derived from the experimental $^{70}Zn(n, \gamma)^{71}Zn^{m}$ cross sections $\langle\sigma_{Zn}^{g+m}\rangle_{present}$. The ratio of the evaluated cross sections folded by the ($p$ ,$n_0$) neutron flux energy spectra for TENDL-2015 $\langle\sigma_{Zn}^{g+m}\rangle_{TENDL}$, JENDL-4.0 $\langle\sigma_{Zn}^{g+m}\rangle_{JENDL}$, TALYS-1.6 with generalized superfluid level density model $\langle\sigma_{Zn}^{g+m}\rangle_{TALYS}$ to the present cross sections are also given.

| $E_n$ (MeV) | $\langle\sigma_{Zn}^{g+m}\rangle_{present}$ (mb) | $\langle\sigma_{Zn}^{g+m}\rangle_{TENDL}$/ $\langle\sigma_{Zn}^{g+m}\rangle_{present}$ | $\langle\sigma_{Zn}^{g+m}\rangle_{JENDL}$/ $\langle\sigma_{Zn}^{g+m}\rangle_{present}$ | $\langle\sigma_{Zn}^{g+m}\rangle_{TALYS}$/ $\langle\sigma_{Zn}^{g+m}\rangle_{present}$ |
|---|---|---|---|---|
| 0.96 ± 0.15 | 3.05 ± 0.27 | 1.90 | 1.15 | 1.33 |
| 1.69 ± 0.15 | 2.24 ± 0.16 | 1.48 | 0.66 | 1.46 |

**Figure 26** shows the excitation function for the $^{70}Zn(n, \gamma)^{71}Zn^{g+m}$ cross sections. It can be seen in this figure that the measured cross section was close to the JENDL-4.0 library at 0.96 MeV whereas between TENDL-2015 and JENDL-4.0 libraries at 1.69 MeV.

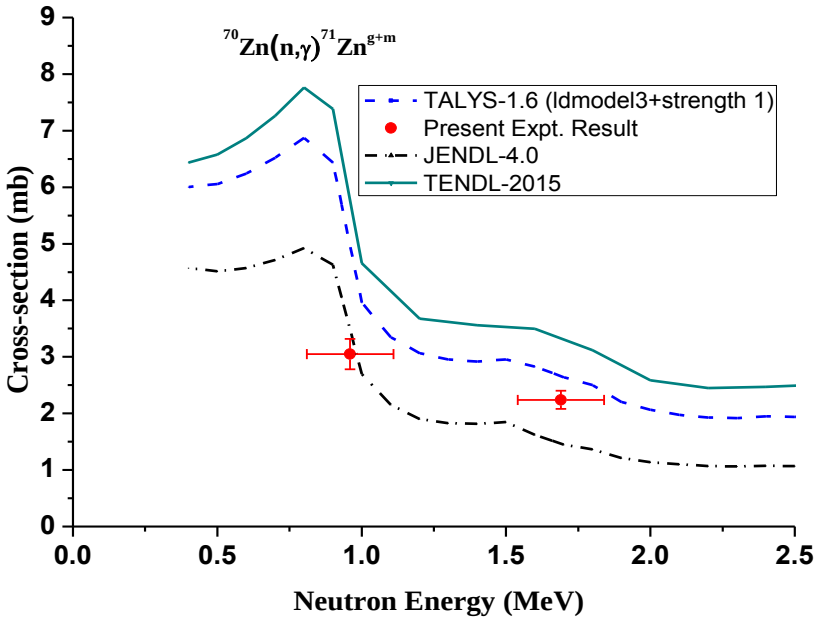


**Figure 26:** Excitation functions of the $^{70}$Zn($n$, $\gamma$)$^{71}$Zn$^{g+m}$ cross sections derived in the present work, evaluated in TENDL-2015 and JENDL-4.0 as well as calculated by TALYS-1.6 with the generalized superfluid level density model (**ldmodel 3**) and the Kopecky-Uhl generalized Lorentzian γ-ray strength function (**strength 1**). The derived present cross sections are ($p$, $n_0$) neutron flux energy spectrum averaged while the evaluated and calculated cross sections were for mono energetic neutrons.

# CHAPTER 6

# SUMMARY AND CONCLUSIONS

# 6. SUMMARY AND CONCLUSIONS

Measurement of neutron radiative capture cross sections for $^{70}Zn(n, \gamma)^{71}Zn^{m}$ reaction was carried out above the upper boundary of the resolved resonance region because there has been no experimental results so far from this region, and while comparing the evaluated total capture cross sections in the basic evaluated nuclear data libraries TENDL-2015, (Koning *et al.,* 2015), JENDL-4.0 (Shibata *et al.*, 2011 ; Iwamoto *et al.*, 2007) and EAF-2010 (Sublet *et al.*, 2010), there are large discrepancies between them. So, it is not possible to know which evaluation is correct in absence of the experimental data. Therefore, the present results in this energy region have been resolved this issue. The neutron capture cross sections of zinc isotopes are important for reactor applications. The radiative capture cross section of $^{70}Zn$ is a candidate of Reactor Dosimetry (Trkov *et al*., 2013). It is also a candidate of dosimetry reactions to study deviation of the epithermal reactor neutron spectrum from 1/E distribution because there is no $^{70}Zn$+n resolved resonance below 10 keV (Trkov, 2015). The deviation from the 1/E distribution is of particular importance in determining the neutron leakage and absorption in the slowing down energy region. It is also important for nuclear astrophysics. In the solar system, about half of the nuclei beyond iron are produced by the slow neutron capture process (*s*-process), the other half by the rapid neutron capture process (*r*-process), and a marginal contribution is provided by the so-called *p*-process (Burbidge *et al*., 1957). This work described how the $^{70}Zn$ is bypassed through $^{69}Zn$ in the s-process path between iron and arsenic (Reifarth, 2012) and how it has linked that path.

The cross sections of the $^{70}Zn(n, \gamma)^{71}Zn^{m}$ ($T_{1/2}$ = 3.96±0.05 hrs) reaction were measured relative to the $^{197}Au(n, \gamma)^{198}Au$ cross sections using activation technique.

The neutrons were obtained by the $^{7}$Li(*p, n*)$^{7}$Be reaction at incident proton energies 2.8 MeV and 3.5 MeV. The experiment was carried out at the Folded Tandem Ion Accelerator (FOTIA) Facility, Nuclear Physics Division, Bhabha Atomic Research Centre (BARC), Mumbai. The neutron spectra at those incident proton energies were obtained by $^{7}$Li(*p, n*)$^{7}$Be neutron spectrum code EPEN (R. Pachuau *et al*., 2017a, 2017b) developed and being tested by our group (NHERG). The EPEN (Energy of Proton-Energy of Neutron) is a tool for simulating neutron spectra resulting from the $^{7}$Li(*p, n*)$^{7}$Be reaction. This code is designed by using evaluated data from $E_p$ = 1.95 - 4 MeV taken from Horst Liskien and Arno Paulsen (Liskien *et al*., 1975) and below 1.95 MeV up to threshold (1880.429 keV) is taken from Macklin and Gibbons (Macklin *et al*., 1958). The average energy of the ground state neutron group calculated with the EPEN (*p, n$_0$*) neutron flux energy spectrum $\varphi_0$(E) were 0.96 and 1.69 MeV for $E_p$ = 2.80 and 3.50 MeV respectively. The width of the (*p, n$_0$*) spectrum is ± 0.15 MeV at both proton energies. The neutron flux was monitored online by a NE213 (shown in the **Figure 10**) neutron detector at zero degree and at 1 m distance from the lithium target. The neutron flux was recorded and saved every 30 minutes to get the neutron flux fluctuation during the whole irradiation period. The γ-ray activity was measured using a pre-calibrated lead-shielded 185 cc high purity germanium (HPGe) detector having 30% relative efficiency, and 1.8 keV energy resolution at 1.33 MeV γ-energy. The data acquisition was carried out using CAMAC based LAMPS (Linux Advanced Multi Parameter System) software (TCAMCON-95/CC 2000 crates controller and CM-48 ADCs). Due to low count rate of $^{71}$Zn$^{m}$, the foil stack was place very close to the detector to obtain high count rate. However, it introduces the coincidence-summing effect. In order to correct the measured efficiency for the

coincidence summing effect, the correction factor $K_c$ was calculated using the Monte Carlo simulation code EFFTRAN (Vidmar, 2005).

Therefore, the $^{70}Zn(n, \gamma)^{71}Zn^{m}$ cross sections have been newly measured by a $^{7}Li(p, n)^{7}Be$ neutron source at 0.96 and 1.69 MeV, and their corresponding $^{70}Zn(n, \gamma)^{71}Zn^{m+g}$ cross sections have been derived. The data analysis was carried out using the latest decay data, and by taking into account the neutron flux fluctuation due to proton current fluctuation during irradiation, low energy ($p, n_1$) neutron backgrounds coming from the neutron population of the first excites state of $^{7}Be$, scattered neutron background originating from elastic, inelastic and multiple scattering in the foil stack and surrounding materials, and γ self-attenuation due to a gamma photon during its passes through any material, including the sample in which it was generated, underwent specific interactions which attenuated the photon either by absorption or scattering with losing energy partially or totally. The measured $^{70}Zn(n, \gamma)^{71}Zn^{m}$ cross sections were compared with theoretical calculations using nuclear reaction model code TALYS-1.6 (Koning *et al*., 2008) with various level density models and γ-ray strength functions available in TALYS-1.6. It has been observed that the theoretical calculation with default parameter settings along with the generalized superfluid model (**ldmodel 3**) and Kopecky-Uhl generalized Lorentzian γ-ray strength function (**strength 1**) predicted well the measured $^{70}Zn(n, \gamma)^{71}Zn^{m}$ cross sections. The derived $^{70}Zn(n, \gamma)^{71}Zn^{g+m}$ cross sections were compared with the latest evaluated cross sections in the TENDL-2015 and JENDL-4.0 libraries. It has been observed that the present derived total cross section agrees well with the JENDL-4.0 library at 0.96 MeV whereas at 1.69 MeV it best matches TALYS-1.6 with combination of ldmodel3 with strength 1 which was in between TENDL-2015 and JENDL-4.0 libraries. This work described how the covariances of neutron captured cross section in reference standard

cross section and efficiency of the HPGe detector were estimated. The uncertainties in the timing factor and HPGe detector were also estimated. The uncertainties in various parameters were summarized in **Table 19** to obtain the $^{70}Zn(n, \gamma)^{71m}Zn$ cross section uncertainties. Then, the total uncertainties in the cross sections were 8.94 and 7.17% at 0.96 and 1.69 MeV, respectively, and also the correlation coefficient between the two cross sections was 0.12.

It can be seen from the **Figure 26** that more experimental data was required in the energy region below 1 MeV, where the discrepancy between evaluated files were maximum to clearly establish which evaluation was correct in predicting the excitation function of $^{70}Zn(n, \gamma)^{71}Zn^{g+m}$ . In this regards, our group carried out experiment at FOTIA, BARC at incident proton energies of 2.25 MeV and 2.6 MeV. The data reduction is being carried out and is being studied as a separate Ph.D. research work by another Research Scholar. These experimental values are expected to resolve a large difference predicted by different evaluators.

## References


Abbas M.I., (2007), "Direct mathematical method for calculating full-energy peak efficiency and coincidence corrections of HPGe detectors for extended sources", *Nucl. Instr. Meth. Phys. Research* B, **256**, 554-557.

Abusaleem K. and Singh B., (2011), "Nuclear Data Sheets for A= 71", *Nucl. Data Sheets* **112**, 133-273.

Arlandini C., Käppeler F., Wisshak K., Gallino R., Lugaro M., Busso M. and Straniero O., (1999), "Neutron capture in low-mass asymptotic giant branch stars: cross sections and abundance signatures", *APJ*, **525**, 886-900.

Axel P., (1962), "Electric dipole ground-state transition width strength function and 7-MeV photon interactions", *Phys. Rev.* **126**, 671-683.

Bao Z., Beer H., Käppeler F., Voss F., Wisshak K., and Rauscher T., (2000), "Neutron cross sections for nucleosynthesis studies", *At. Data Nucl. Data Tables*,**76**,70-154.

Beer H., Voss F. and Winters R.R., (1992), " On the calculation of Maxwellian-averaged capture cross sections", *Astrophys. J., Suppl. Ser*.**, 80** : 403-424.

Bersillon O., Greenwood L.R., Griffin P.J., Mannhart W., Nolthenius H.J., Paviotti-Corcuera R., Zolotarev K.I., and Zsolnay E.M., (2006), "International Reactor Dosimetry File 2002 (IRDF-2002)", Report STI/DOC/010/452, International Atomic Energy Agency.

Blachot J., (2012), "Nuclear Data Sheets for A = 115", *Nucl. Data Sheets* **113**,10, 2391-2535.

Bode P., De Coeij, J.J.M., (1998), "Activation analysis", Encyclopaedia of Environmental Analysis and Remediation, *J. Wiley & Sons, New York*, ISBN 0-471-11708-0, 68–84.

Brink D.M., (1957), "Individual particle and collective aspects of the nuclear photoeffect*", Nucl. Phys*. **4**, 215-220.

Burbidge, E. M., Burbidge, G. R., Fowler, W. A., & Hoyle, F., Rev., (1957), "Synthesis of the elements in stars", *Mod. Phys*., **29**, 547-650.

Capote R., Herman M., Oblozinsky P., Young P.G., Goriely S., Belgya T., Ignatyuk A.V., Koning A.J., Hilaire S., Plujko V., Avrigeanu M., Bersillon O., Chadwick M.B., Fukahori T., Kailas S., Kopecky J., Maslov V.M., Reffo G., Sin M., Soukhovitskii E., Talou P., Han Yinlu, and Ge Zhigang, (2009), "Reference Input Parameter Library (RIPL-3)", *Nucl. Data Sheets* **110**, 3107-3214.

Carlson A.D., Pronyaev V.G., Smith D.L., Larson, Zhenpeng Chen N.M., Hale G.M., Hambsch F.-J., Gai E.V., Soo-Youl Oh, Badikov S.A., Kawano T., Hofmann H.M., Vonach H., and Tagesen S., (2009), "International evaluation of neutron cross section standards", Nucl. Data Sheets **110**, 3215-3324.

Chandani Z., (2014), "Development of Low Level $^{226}$Ra Activity Analysis for Live Fish Using Gamma-Ray Spectrometry", A dissertation submitted to Mc Master University for the Degree of Master of Sciences, *http://hdl.handle.net/ 11375/15978.*

Cohen I.M., Guevara S.R., Arribére M.A., Fornaciari Iljadica M.C., Kestelman A.J., Ohaco R.A., Segovia M.S. and Yunes A.N., "Determination of nuclear constants of reactions induced on zinc by short irradiations with the epithermal and fast components of a reactor neutron spectrum", (2005), *Radiochim. Acta* **93**, 543–546.

Damon R.W., (2005), "Determination of the photo-peak detection efficiency of a HpGe detector, for volume sources, via Monte Carlo simulations",

Dissertation submitted to the University of the Western Cape for the Degree of Master of Sciences in Physics, *http://hdl.handle.net/11394/256.*

De Felice P., Angelini P., Fazio A., Biagini R., (2000). "Fast procedures for coincidence-summing correction in gamma-ray spectrometry", *Appl. Radiat. Isot.* **52**, 745–752.

Demetriou P. and Goriely S., (2001), "Microscopic nuclear level densities for practical applications", *Nucl. Phys*. **A695**, 95-108.

Domingo-Pardo C., (2004), "New radiative neutron capture measurement of $^{207}$Pb and $^{209}$Bi", A doctoral thesis submitted to Universidad de Valencia – CSIC (University of Valencia), *https://ific.uv.es/gamma/tesis_doctorales/Thesis Domingo.pdf.*

Ericson T., (1960), "The statistical model and nuclear level densities", *Adv. Phys*. **9**, 425-511.

Fessler A., Plompen A.J.M., Smith D.L., Meadows J.W., and Ikeda Y., (2000), "Neutron activation cross section measurements from 16 to 20 MeV for Isotopes of F, Na, Mg, Al, Si, P, Cl, Ti, V, Mn, Fe, Nb, Sn, and Ba", *Nucl. Sci. Eng.* **134**, 171-200.

Gicking A., (2012), "Neutron capture cross sections of cadmium isotopes", A thesis submitted to Oregon State University for the degree of Bachelor of Science, *http://ir.library.oregonstate.edu/concern/undergraduate_thesis_or_projects/kh04dr15d.*

Gallino R., Arlandini C., Busso M, Lugaro M, Travaglio C., Straniero O., Chieffi A., and Limongi M., (1998), "Evolution and Nucleosynthesis in low-Mass Asymptotic Giant Branch Stars. II. Neutron Capture and the s-Process", *APJ* **497**, 388-403.

Gilmore G., (2008), "Practical gamma-ray spectroscopy", England: John Wiley &

Sons Ltd.

Gilbert A. and Cameron A.G.W., (1965), "A composite nuclear-level density formula with shell corrections", *Can. J. Phys*. **43**, 1446-1496.

Goriely S., (1998), "Improved microscopic nuclear level densities within the Hartree-Fock-Bogoliubov plus combinatorial method", *Phys. Lett*. B **436**, 10-18.

Goriely S., Tondeur F., Pearson J.M., (2001), "A Hartree–Fock nuclear mass table", *Atom. Data Nucl. Data Tables* 77, 311-381.

Goriely S., Hilaire S. and Koning A.J., (2008), "Improved microscopic nuclear level densities within the Hartree-Fock-Bogoliubov plus combinatorial method", *Phys. Rev*. C **78**, 064307.

Goriely S., Hilaire S., Koning A.J., and Capote R., (2011), "Towards improved evaluation of neutron induced fission cross section", Proceedings of the International Conference on Nuclear Data for Science and Technology, *Journ. Kor. Phys. Soc*. **59**, 23, 979-982.

Grossjean M.K. and Feldmeier H., (1985), ""Level density of a Fermi gas with pairing interactions", *Nucl. Phys*. **A444**, 113-132.

Hamidatou L., Slamene H., Akhal T. and Zouranen B., (2013), "Concepts, Instrumentation and Techniques of Neutron Activation Analysis," In: F. Kharfi, Ed., Imaging and Radioanalytical Techniques in Interdisciplinary Research — Fundamentals and Cutting Edge Applications, *InTech, Rijeka*, 141-178, *http://www.intechopen.com/books/imaging-and-radioanalyal-techniques-in-interdisciplinnary-research-fundamentals-and-cutting-edge-applications/concepts-instrumentationand-techniques-of-neutron-activation-analysis; http://dx.doi.org/10.5772/53686.*

Haquin G., (2017), "Coincidence summing corrections in gamma ray spectrometry:

overview and experimental data", *http://www.iaea.org/inis/collection/ NCLCollectionStore/_Public/35/066/35066096.pdf.*

Herman M., Capote R., Sin M., Trkov A., Carlson B.V., Oblo_zinsk_y P., Mattoon C.M., Wienke H., Hoblit S., Young-Sik Cho, Nobre G.P.A., Plujko V.A., Zerkin V., (2013), EMPIRE-3.2 Malta, User's Manual, *http://www-nds. iaea.org/ publications.*

Hilaire S., Girod M., Goriely S. and Koning A.J., (2012), "Temperature dependent combinatorial level densities with the D1M Gogny force", *Phys. Rev*. **C 86**, 064317.

Hauser W. and Feshbach H., (1952), "The Inelastic Scattering of Neutrons", *Phys. Rev*. **87**, 366-373.

Huang Xiaolong, (2009), "Nuclear Data Sheets for A = 198", *Nucl. Data Sheets* **110**, 2533-2688.

IAEA-TECDOC-1215, (2001), "Use of research reactors for neutron activation analysis", Report of an Advisory Group meeting held in Vienna, 22–26 June 1998. IAEA-TECDOC-1215, ISSN 1011–4289.

Ignatyuk A.V., Istekov K.K., and Smirenkin G.N., (1979), "The role of collective effects in the systematics of nuclear level densities", *Sov. J. Nucl. Phys*. **29**, 4, 450-454.

Ignatyuk, A.V., Weil, J.L., Raman, S., Kahane, S., (1993). Density of discrete levels in $^{116}$Sn, *Phys. Rev*. **C**. **47**, 1504–1513.

Ilieva K. (2011), "Need of Reactor Dosimetry Preservation", Proceedings of an International Conference on Opportunities and Challenges for Water Cooled Reactors in the 21st Century, *IAEA-CN--164-4P04.*

Iwamoto N., (2007), "New Evaluation of Neutron Nuclear Data for Zinc Isotopes", *J. Nucl. Sci. Technol.* **44**, 1131-1141.

Jackman K.R., (2007), "KMESS: An Open Source Software Package Using a Semi-empirical Mesh-Grid Method for the Modelling of Germanium Detector Efficiencies", Dissertation submitted to the University of Texas at Austin for the Degree of Doctor of Philosophy, *https://search.proquest.com/openview/7836a219a36c8a995173c218c651819d.*

Käppeler, F., Beer, H., & Wisshak, K., (1989), " s-Process nucleosynthesis-nuclear physics and the classical model", *Rep. Prog. Phys*., **52**, 945-1013.

Knoll G. F., (2000), "Radiation Drtection and Measurement", *Wiley India Pvt. Ltd*., ISBN : 978-81-265-2260-6.

Koloczek A., Thomas B., Glorius J., Plag R., Pignatari M., Reifarth R., Ritter C., Schmidt S., Sonnabend K., (2016), "Sensitivity study for s process nucleosynthesis in AGB stars", *At. Data Nucl. Data Tables* **108**, 1-14.

Koning A.J. and Delaroche J.P., (2003), "Local and global nucleon optical models from 1 keV to 200 MeV", *Nucl. Phys*. A **713**, 231-310.

Koning A.J., Hilaire S. and Duijvestijn M.C., (2008a) "TALYS-1.0", Proceedings of the International Conference on Nuclear Data for Science and Technology, April 22-27, 2007, *EDP Sciences*, 211-214.

Koning A.J., Hilaire S. and Goriely S., (2008b), "Global and local level density models", *Nucl. Phys.* A **810**, 13-76.

Koning A.J. and Rochman D., (2012), "Modern Nuclear Data Evaluation with the TALYS Code System", *Nucl. Data Sheets* **113**, 2841-2934.

Koning A.J., Hilaire S. and Goriely S., (2013), Talys 1.6 - A Nuclear Reaction Program, User Manual, First Edition, www.talys.eu.

Koning A.J., Rochman D., Kopecky J., Sublet J.Ch., Fleming M., Bauge, E., Hilaire S., Romain P., Morillon B., Duarte H., van der Marck S.C., Pomp S.,

Sjostrand H., Forresr R., Henriksson H., Cabellos O., Goriely S., Leppanen J., Leeb H., Plompen A., and Mills R., (2015), "TENDL-2015 : TALYS-based evaluated nuclear data library", *https://tendl.web.psi.ch/tendl_2015/tendl 2015.html.*

Kopecky J. and Uhl M., "Test of gamma-ray strength functions in nuclear reaction model calculations", (1990), *Phys. Rev*. C **41**, 1941-1955.

Kopecky J., Uhl M. and Chrien R. E., (1993), "Radiative strength in the compound nucleus $^{157}$Gd", *Phys. Rev*. C **47**, 312.

Krane K.S., (2017), "Neutron capture cross sections of $^{70}$Zn and the decay of $^{71m}$Zn", *Appl. Radiat. and Isot*. **121**, 28-37.

Larsen A.C. and Goriely S., (2010a), "Impact of a low-energy enhancement in the γ-ray strength function on the neutron-capture cross section", *Phys. Rev*. C **82,** 014318.

Larsen A.C., Agvaanluvsan U., Bernstein L.A., Brger A., Chankova R., Goriely S., Guttormsen M. , Lonnroth T., Mitchell G.E., Nyhus H.T., Siem S., Syed N.U.H., Toft H.K. and Voinov A., (2010b), "Soft structure of gamma-ray strength functions studied with the Oslo method", CNR*09 – Second International Workshop on Compound Nuclear Reactions and Related Topics, eds. Bonneau L., Dubray N., Gunsing F., Jurado B., *Eur. Phys. J.*, **2**, 03001.

Lederer C., Andrzejewski J., Barbagallo M., Chiaveri E., Domingo-Pardo C., Dressler R., Ferreira P., Gon_calves I.F., Guerrero C., Gunsing F., Kappeler F., Neuhausen J., Massimi C., Perkowski J., Reifarth R., Schumann D., Tagliente G., Tain J.L., Vaz P., Wallner A., WeiB C., (2013), "Neutron capture cross sections of $^{70,72,73,74,76}$Ge at n-TOF EAR-1", CERN-INTC-

2013-021 / INTC-P-381.

Liskien H. and Paulsen A., (1975), "Neutron production cross sections and energies for the reactions $^{7}$Li(*p, n*)$^{7}$Be and $^{7}$Li(*p, n*)$^{7}$Be* *At. Data Nucl. Data Tables* **15**, 57-84.

Macklin R.L. and Gibbons J.H., (1958), "Study of the T(*p, n*)$^{3}$He and $^{7}$Li(*p, n*)$^{7}$Be Reactions", *Phys. Rev.*, **109**, 105.

Mangal S.K. and Gill P.S., (1962), "Thermal neutron activation cross sections for isomer production", *Nuclear Physics* **36,** 542-548.

Mannhart W. and Vonach H.K., (1968), "Isomere wirkungsquerschnittsverhäiltnisse Beim thermischen neutroneneinfang im bereic der $2p_{1/2}$ and 1 $g_{9/2}$ schalenmodellzustäinde (Isomeric cross section ratios for $2p_{1/2}$ and $1g_{9/2}$ Shell Model States formed by thermal neutron capture)", *Zeitschrift für Physik* **210**, 13-31.

Mannhart W., (2013), "A small guide to generating covariances of experimental data", Report of the International Nuclear Data Committee, *INDC(NDS)*-**0588** (Rev.), International Atomic Energy Agency.

Martin M., (2013), "Nuclear Data Sheets for A = 152*", *J., Nucl. Data Sheets* **114**, 1497-1847.

Millsap D.W. and Landsberger S., (2015), "Self-attenuation as a function of gamma ray energy in naturally occurring radioactive material in the oil and gas industry", *Appl. Radiat. Isot*. **97**, 21-23.

Nowotny R., (1998), "XMuDat: Photon attenuation data on PC Version 1.0.1 of August 1998", Report IAEA-NDS-195, International Atomic Energy Agency.

Otuka N., Dupont E., Semkova V., Pritychenko B., Blokhin A.I., Aikawa M., Babykina S., Bossant M., Chen G., Dunaeva S., Forrest R.A., Fukahori T., Furutachi N., Ganesan S., Ge Z., Gritzay O.O., Herman M., Hlavač S., Katō

K., Lalremruata B., Lee Y.O., Makinaga A., Matsumoto K., Mikhaylyukova M., Pikulina G., Pronyaev V.G., Saxena A., Schwerer O., Simakov S.P., Soppera N., Suzuki R., Takács S., Tao X., Taova S., Tárkányi F., Varlamov V.V., Wang J., Yang S.C., Zerkin V., and Zhuang Y., (2014), *Nucl. Data Sheets* **120**, 272-276.

Otuka N., Lalremruata B., Khandaker M.U., Usman A.R., and Punte L.R.M., (2017), "Uncertainty propagation in activation cross section measurements", *Radiation Phys. Chem*. **140**, 502-510, *https://doi.org/10.1016/j.radphychem. 2017.01.013.*

Pachuau, R., Lalremruata, B., Otuka, N., Hlondo, L.R., Punte, L.R.M., Thanga, H.H., (2017a), "Thick and thin target $^{7}$Li(*p, n*)$^{7}$Be neutron spectra below the three-body break up reaction threshold", *Nucl. Sci. Eng*. 187. 70-80, *http://dx.doi. org/10.1080/00295639.2017.1291053.*

Pachuau, R., Lalremruata, B., Otuka, N., Hlondo, L.R., Punte, L.R.M., Thanga, H.H., (2017b), "A tool for calculation of $^{7}$Li(*p, n*)$^{7}$Be neutron source spectra below the three body break-up reaction threshold", Proceedings of the ND2016, *EPJ* **146**, 12016, *https://doi.org/10.1051/epjconf/201714612016.*

Peralta, L., (2004), "Measuring the activity of a radioactive source in the classroom", *Eur. J. Phys*, **25**, 211-219.

Pignatari M., Gallino R., Heil M., Wiescher M., Käppeler F., Herwig F., and Bisterzo S., (2010), "The weak *s*-process in massive stars and its dependence on the neutron capture cross sections", *APJ,* **710**:1557-1577.

Reifarth R., Dababneh S., Heil M., Käppeler F., Plag R., Sonnabend K., and Uberseder E., (2012), "Neutron activation of natural zinc samples at kT = 25 keV", *Phys. Rev*. C **85**, 035802.

Robu E. and Giovani C., (2009), "Gamma-ray self-attenuation corrections in environmental samples", *Rom. Rep. Phys*. **61**, 295-300.

Sage C., Semkova V., Bouland O., Dessagne P., Fernandez A., Gunsing F., Nastren C., Noguere G., Ottmar H., Plompen A.J.M., Romain P., Rudolf G., Somers J., and Wastin F., (2010), "High resolution measurements of the $^{241}$Am(*n*, 2*n*) reaction cross section", *Phys.Rev*. C **81**, 064604.

Sato T., Niita K., Matsuda N., Hashimoto S., Iwamoto Y., Noda S., Ogawa T., Iwase H., Nakashima H., Fukahori T., Okumura K., Kai T., Chiba S., Furuta, and L. Sihver T., (2013), "Particle and Heavy Ion Transport code System, PHITS, version 2.52", *J. Nucl. Sci. Technol*. **50**, 913-923.

Semkow T.M., Mehmood G., Parekh P.P., Virgil M., (1990). "Coincidence Summing In Gamma-Ray Spectroscopy". Nucl. Instr. Meth. Phys. Res. **A290,** 437-444.

Shibata K., Iwamoto O., Nakagawa T., Iwamoto N., Ichihara A., Kunieda S., Chiba S., Furutaka K., Otuka N., Ohsawa T., Murata T., Matsunobu H., Zukeran A., Kamada S., and Katakura J., (2011), "JENDL-4.0: A New Library for Nuclear Science and Engineering", *J. Nucl. Sci. Technol*. **48**, 1, 1-30.

Smith D.L. and Otuka N., (2012), "Experimental nuclear reaction data uncertainties: basic concepts and documentation", *Nucl. Data Sheets* **113**, 3006-3053.

Sublet J.C., Packer L.W., Kopecky J., Forrest R.A., Koning A.J., and Rochman D.A., (2010), "The European Activation File: EAF-2010 neutron-induced cross section library", Report CCFE-R(1) 05, Culham Centre for Fusion Energy.

The L. –S., Mounib F. El Eid, and Bradley S. Meyer, (2007), "s-Process Nucleosynthesis in Advanced Burning Phases of Massive Stars", *ApJ*, **655**, 1058-1078.

Travaglio C., Gallino R., Arnone E., Cowan J., Jordan F., and Sneden C., (2004), "Galactic evolution of Sr, Y, and Zr : A multiplicity of nucleosynthetic processes", *APJ* **601**, 864-884,

Trkov A., Greenwood L. R., and Simakov S. P., (2013), "Testing and improving the International Reactor Dosimetry and Fusion File (IRDFF)", Summary Report of the First Research Coordination Meeting, 1-5 July 2013, *INDC (NDS)-***0639**, *International Atomic Energy Agenc, http://www-nds.iaea.org/ public cations.*

Trkov A., Private communication (2015).

Verma H. R., (2007), "Atomic and Nuclear Analytic Methods", Springer, ISBN 10: 3540302778 / ISBN 13: 9783540302773.

Vidmar T., (2005), "EFFTRAN—A Monte Carlo efficiency transfer code for gamma-ray Spectrometry", *Nucl. Instrum. Meth.* A **550**, 603-608.

Yit-Fong Chan, "Neutron activation measurements for materials used in fusion reactors", (2012), Dissertation submitted to the Department of Physics at the University of York for the Degree of Master of Science in Physics, *http://etheses. whiterose.ac.uk/4023/1/YFCHAN_n-activation.pdf.*

Xhixha G.,(2012), "Advanced gamma-ray spectrometry for environmental radioactivity monitoring", A Ph.D thesis submitted to The University of Ferrara, Ferrara, Italy: 29, March 2012, *https://core.ac.uk/download/pdf/ 11822939.pdf.*

## List of Research Publications

### International Publications

1. Punte L.R.M., Lalremruata B., Otuka N., Suryanarayana S.V., Iwamoto Y., Pachuau R., Satheesh B., Thanga H.H., Danu L.S., Desai V.V., Hlondo L.R., Kailas S., Ganesan S., Nayak B.K., Saxena A., (2017), 'Measurements of neutron capture cross sections on $^{70}$Zn at 0.96 and 1.69 MeV', *Phys. Rev.* **C 95**, 024619.

2. Lalremruata B., Punte L.R.M., Otuka N., Pachuau R., Iwamoto Y., Suryanarayana S.V., Nayak B.K., Satheesh B., Thanga H.H., Danu L.S., Desai V.V., Hlondo L.R., Ganesan S., Saxena A., (March, 2017), 'Measurements of neutron capture cross sections on $^{70}$Zn at 0.96 and 1.69 MeV', *INDC(IND)-**0049**, International Atomic Energy Agency.*

3. Otuka N., Lalremruata B., Khandakerd M.U., Usmand A.R., Punte L.R.M., (2017), "Uncertainty propagation in activation cross section measurements", *Radiat. Phys. Chem.* **140**, 502-510.

4. Hlondo L.R., Lalremruata B., Punte L. R. M., Rebecca L., Lalnunthari J., and Thanga H.H., (2016) 'A revisit to self-excited push pull vacuum tube radio frequency oscillator for ion sources and power measurements', *Rev. Sci. Intrum.* **87**, 045101.

5. Pachuau R., Lalremruata B., Otuka N., Hlondo L.R., Punte L.R.M., Thanga H.H., (2017), 'Thick and thin target $^{7}$Li(*p, n*)$^{7}$Be neutron spectra below the three-body break up reaction threshold', *Nucl. Sci. Eng.*. **187**, 70-81.

6. Pachuau Rebecca, Lalremruata B., Otuka N., Suryanarayana S. V., Punte L.R.M., Hlondo L.R., Desai V. V., Satheesh B., Kailas S., Ganesan S., Nayak B. K., and Saxena A., (2018), "Energy dependence of zinc-70 neutron capture cross section near the inelastic scattering threshold", *Phys. Rev.* **C**., **97**, 064617.

**Conference/Symposium Publications**

1. Punte L.R.M., Lalremruata B., Satheesh B., Thanga H.H., Otuka N., Saxena A., Suryanarayana S. V., Nayak B. K., Ganesan S., Danu L. S., and Desai V., (2013), 'Measurement of fast neutron radiative capture cross sections for $^{70}Zn(n, \gamma)^{71}Zn^{m}$ reaction using isotopically enriched $^{70}Zn$ isotope in the incident neutron energy range 0.3 - 1.5 MeV', *Proceedings of the DAE Symp. on Nucl. Phys.* **58**, 384-385.

2. Satheesh B., Musthafa M.M., Singh B.P., Prasad R., Lalremruata B., Thanga H.H., and Punte L. R., 'Production of the isomeric pairs $^{119g,m}Te$ and $^{121g,m}Te$ in proton induced nuclear reactions', (2013), *Proceedings of the DAE Symp. on Nucl. Phys.* **58,** 350-351.

3. Pachuau R., Lalremruata B., Otuka N., Hlondo L.R., Punte L.R.M., and Thanga H.H., (2016), "A tool for calculation of $^{7}Li(p, n)^{7}Be$ neutron source spectra below the three body break-up reaction threshold", Proceedings of the ND2016, *EPJ.* **146**, 12016.

4. Pachuau R., Lalremruata B., Otuka N., Hlondo L.R., Punte L.R.M., Thanga H.H., (2017), 'A tool for calculation of $^{7}Li(p, n)^{7}Be$ neutron source spectra below the three body break-up reaction threshold', *Proceedings of the DAE-BRNS Symp. on Nucl. Phys.* **61**, 430-431.

**Papers/Poster Presentations**

1. Poster presentation at DAE-BRNS, International Symposium on Nuclear Physics, BARC, Mumbai, *$2^{nd}$ – $6^{th}$ December, 2013*.

2. Oral presentation at National Workshop on Error Propagation in Nuclear Reaction Data Measurement-2017 (EPNRDM-2017), MZU, Aizawl, *$13^{th}$ - $14^{th}$ March, 2017*.

## Conferences/Symposiums/Workshops/Seminars Attended

1. 5th DAE-BRNS Theme Meeting on EXFOR Compilation of Nuclear Data (EXFOR 2013), *18th -22nd February, 2013*.

2. International Symposium on Nuclear Physics, BARC, Mumbai, *2nd - 6th December, 2013*.

3. One Day State Level Acquaintance Programme, MZU, Aizawl, *28th March, 2014*.

4. Two Days Workshop on Physics Teaching in Higher Secondary School of Mizoram, MZU, Aizawl, *4th - 9th March, 2014*.

5. Condensed Matter Days-2016 (CMDAYS-2016), MZU, Aizawl, *29th - 31st March, 2014.*

6. Mizoram Science Congress, MZU, Aizawl, *13th - 14th October, 2016.*

7. Error Propagation in Nuclear Reaction Data Measurement-2017 (EPNRDM-2017), MZU, Aizawl, *13th - 14th March, 2017*.

## Brief Bio-data of the Author

The author is currently a research scholar in the Department of Physics, Mizoram University. He received his Master degree in Physics at Mizoram University with first class in 2012 and he was awarded a Gold Medal for securing first position. The author was employed as a Guest Lecturer in the Department of Physics, Mizoram University for the period August – October, 2012. He was also employed as a Junior Research Fellow (JRF) from 1st November, 2012 to 31st October, 2014, and a Senior Research Fellow (SRF) from 1st November, 2014 to 31st October, 2015 under the DAE-BRNS project entitled "Measurements EXFOR Compilation and Theoretical Study of Nuclear Data" (Sanction No.: 2012/36/17-BRNS Dated 14.8.2012). He has completed his project research work with satisfaction. The author got admitted in the Department of Physics, Mizoram University as a Ph.D. Scholar in August 2013 and successfully completed the Pre Ph.D. Course work in August 2014 with grade 'O'. He has been registered for Ph.D. with Reg. No.: MZU/Ph.D./692 of 20.10.2014. His main research interests are in the areas of Nuclear Physics and his topic is "Measurement of neutron radiative capture cross sections for $^{70}$Zn($n$, $\gamma$)$^{71}$Zn$^{m}$ reaction using isotopically enriched $^{70}$Zn isotope in the few MeV incident neutron energy region". He has published several papers in both the international and national journals and has also attended various state and national level conferences, symposium and workshops.

## Address:

Lalrinmawia Punte
H.No.: F-12/3,
Biak In Mual, Republic Veng-796005
Aizawl, Mizoram.
E-mail: lrpunte7@gmail.com

# Reprints of Research Papers